České vysoké učení technické v Praze
Fakulta jaderná a fyzikálně inženýrská
Katedra fyziky

Particle confinement of pellet fuelled plasmas in tokamaks

Diploma thesis

Autor práce: **Bc. Pavel Háček**
Vedoucí úkolu: **Ing. Martin Valovič, PhD.**
Akademický rok: **2008/2009**

Název práce:
Udržení částic v tokamakovém plazmatu při vstřelování pelet

Autor: Bc. PavelHáček

Obor: Fyzikální inženýrství

Druh práce: Diplomová práce

Vedoucí práce: Ing. Martin Valovič, Ph.D., EURATOM/ UKAEA Fusion, Abingdon U.K.

Konzultant: Ing. Ivan Ďuran, Ph.D.

Abstrakt: Tokamaky jsou nejpokročilejším zařízením ve výzkumu řízené jaderné fúze. V roce 2007 začala výstavba obřího tokamaku ITER, který má za úkol prokázat technologickou proveditelnost fúze s magnetickým udržením. Jedním z klíčových témat výzkumu je doplňování paliva do tokamaků. Pro velká zařízení jako ITER je nezbytná technologie vstřelování pelet. Pelety ovšem velmi narušují prostředí okraje plazmatu a jsou zdrojem zvýšené aktivity tzv. ELMů a zvýšeného transportu částic a energie. Tento transport se nazývá anomální, neboť neodpovídá teoretickým předpovědím pro difúzi a nabývá mnohem větších hodnot. Část této práce se zabývá teoretickým základem anomální difúze. V experimentální části je z dat z tokamaku JET kvantifikován transport částic po vstřelení pelet výpočtem difuzního koeficientu a doby udržení peletu.

Klíčová slova: Tokamak, vstřelování pelet, anomální difúze, difuzní koeficient, doba udržení peletu

Title:
Particle confinement of pellet fuelled plasmas in tokamaks

Author: Bc. Pavel Háček

Abstract: Tokamaks are the most advanced devices in the research of controlled nuclear fusion. In the year 2007 construction of giant tokamak ITER has begun. ITER's goal is to demonstrate the technological feasibility of magnetic confinement fusion. One of the crucial parts of the research is the tokamak plasma refuelling. For big devices like ITER, technology of pellet injection is necessary. Pellets, however, disturb the edge plasma and cause enhanced ELM activity along with increased particle and energy transport. This transport is called anomalous, as it does not correspond to theoretical predictions of diffusion and it reaches far higher values. Part of this work is aimed at explaining the theoretical basis of the anomalous diffusion. The experimental part with use of data the JET tokamak data quantifies the post pellet particle transport by calculation of diffusion coefficient and pellet retention time.

Key words: Tokamak, pellet injection, anomalous diffusion, diffusion coefficient, pellet retention time

Contents

1 Introduction

This thesis is based upon previous bachelor thesis [1] and research project [2], from which parts of the text were retaken.

There are several types of experimental devices for confining hot plasma necessary for the fusion reaction to occur at a sufficient rate. The most advanced one is the tokamak concept and in present time a large tokamak ITER is being built, which is estimated to produce *500MW* of fusion power. Tokamak plasma refuelling is one of the most important and fundamental parts of the tokamak research. With the necessity of increasing the tokamak dimensions it is more difficult to deliver the fuel particles deep into the plasma column. Simple gas puff used for the smaller tokamaks becomes incapable of that task and the most important technology of tokamak plasma fuelling for future devices like ITER would be *pellet injection*. Small solid fuel pellets are injected at high speeds into the plasma. The question of refuelling is closely connected with the energy and particle confinement and transport in plasma. The confinement properties of the toroidally symmetric tokamak plasma have been calculated for particle Coulomb collisions. This so called *neoclassical transport* does not, however, agree with the experiments. The observed transport is called *anomalous* and occurs because of plasma instabilities. To explain and understand the theory of anomalous transport is one of the major challenges for present tokamak physics. This work's goal was to attempt to quantify the edge plasma diffusion during the pellet fuelling to be able to estimate the requirements for the ITER pellet injection system.

The theoretical part of this work consists of four chapters. In the chapter 2, the idea of nuclear fusion and magnetic confinement of hot plasma is outlined. In chapter 3, the tokamak plasma equilibrium and the concept of magnetic surfaces is presented, as it is important for the choice of coordinates in the experimental part of the thesis. In the chapter 4, the basics of transport in tokamaks, mainly the anomalous one are given. The fifth chapter is about principles of pellet fuelling, the physics of pellet ablation and shielding, pellet injection technological issues and design of JET and proposed design of ITER pellet injection system.

The original part of this work is contained in chapters 6 - 8. There the data were downloaded from the JET tokamak database for shot *#53212*, which was a part of experiments undertaken at JET aimed to develop optimized pellet refuelling scenarios. The basic parameters of the shot *#53212* and parameters of the injected pellets, along with description of the downloaded data and the observed plasma response to the pellet operation are outlined in chapter 6. The most important data for the analysis in this work was the LIDAR measured electron density profile. Due to insufficient temporal resolution of these profiles compared to fast post-pellet particle losses, the data were pre-processed by a boxcar analysis, which is described in chapter 7. An average post-pellet density profile evolution was thus gained. Chapter 8 is the main chapter of this thesis and it contains all the calculations made.

2 Controlled thermonuclear fusion on Earth

2.1 Nuclear fusion

The development of human society has always been closely connected to searching new energy sources. In present time, the main ways of gaining energy are burning the fossil fuels like coal and oil, nuclear fission of heavy atoms like uranium-235 and also the exploitation of renewable sources like wind, water or sun. However, none of these energy sources is perfect. The fossil fuels cause massive pollution of Earth's atmosphere by CO_2 and therefore contribute to the greenhouse effect and also their reserves are limited. The exploitation of the renewable sources is limited by local geographic and weather conditions. Presently the most promising nuclear fission faces problems with storing of the radioactive waste. These disadvantages along with quick population growth (world population is expected to reach almost 8.1 billion in 2030) and also growth of the global primary energy demand (projected to increase by 52% from 2003 to 2030) are the main arguments pointing at the necessity of finding a new, efficient energy source available for all nations and harmless to the environment. Apart from the fourth generation nuclear fission reactors, this role could be played by nuclear fusion (either in fusion-fission hybrid reactors or in purely fusion devices).

The fusion reaction is a nuclear reaction between two light atomic nuclei (with atomic mass number $A<56$), which releases energy. The new nuclear arrangement is more stable, its total mass is reduced, and therefore corresponding amount of energy is released. This energy is in form of kinetic energy of the products. The amount of released energy is far greater than by nuclear fission of heavy atoms as you can see on Fig 2.1. [3][4][5]

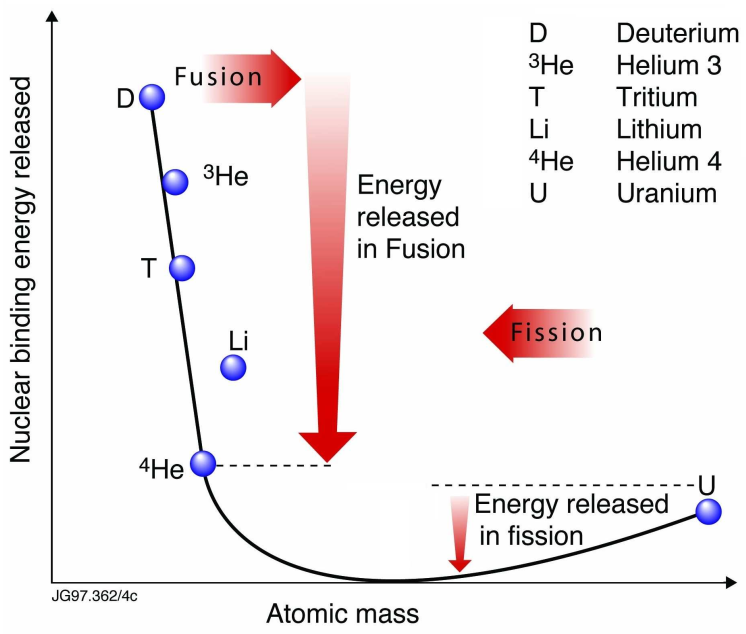

Figure 2.1: *Energy released by nuclear reactions [5]*

There are several reactions, which are considered to be used for controlled nuclear fusion on Earth [6]:

$$D + T \rightarrow {}^{4}He\ (3.52\ MeV) + n\ (14.06\ MeV) \tag{2.1}$$

$$D + D \rightarrow T\ (1.01\ MeV) + p\ (3.03\ MeV) \tag{2.2}$$

$$D + D \rightarrow {}^{3}He\ (0.82\ MeV) + n\ (2.45\ MeV) \tag{2.3}$$

$$D + {}^{3}He \rightarrow {}^{4}He\ (3.67\ MeV) + p\ (14.67\ MeV) \tag{2.4}$$

The first of these reactions (2.1) is supposed to be used in the first generation thermonuclear reactors, as it is the easiest to achieve. It is a reaction between two isotopes of hydrogen, deuterium and tritium (so called DT reaction). For lower energies, the cross section of DT fusion reaction is much higher than the cross sections of other mentioned reactions. [3]

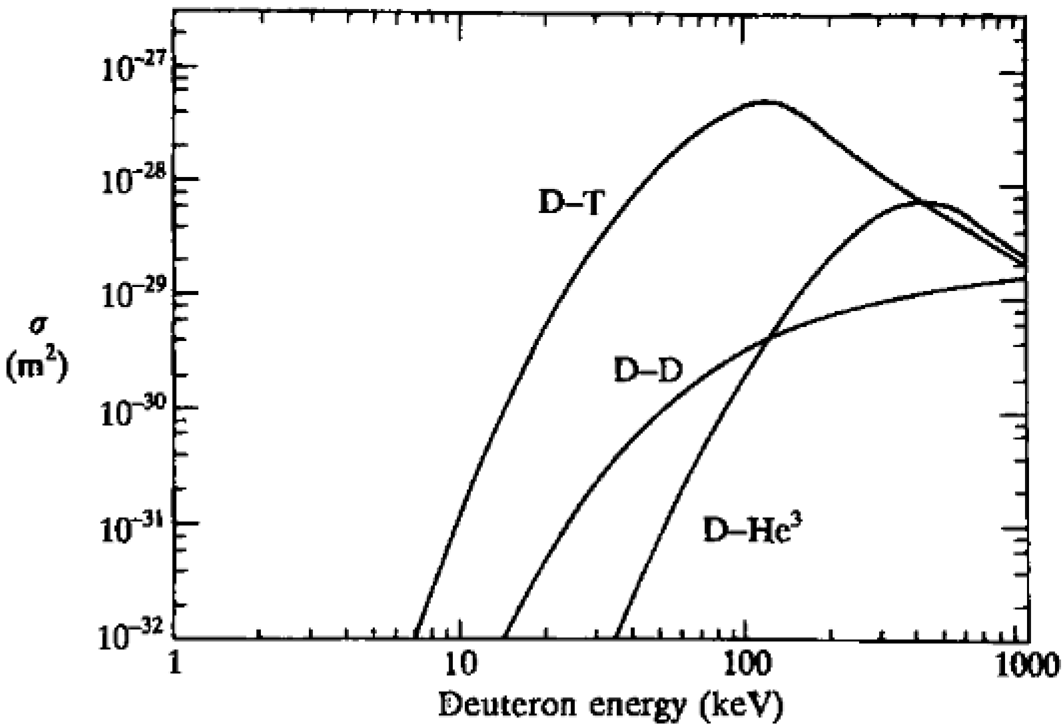

Figure 2.2: *Nuclear fusion reactions' cross sections, the two D-D reactions have similar cross sections, the graph shows their sum [4]*

Tritium is radioactive with a half-life of *12.3* years and so its natural reserves are negligible. Therefore it has to be manufactured. It is projected that tritium will be produced in the future fusion power plants by reaction of lithium with neutrons released by the fusion reaction:

$${}^{6}Li + n \rightarrow {}^{4}He + T + 4.8\ MeV \tag{2.5}$$

$${}^{7}Li + n \rightarrow {}^{4}He + T + n - 2.5\ MeV \tag{2.6}$$

Deuterium can be gained easily from the sea water. In average, there is one deuterium atom per *7000* normal hydrogen atoms. The Earth's reserves of lithium are estimated in millions of tons and will last for at least thousand years. The reserves of deuterium are practically inexhaustible.

As we can see, the nuclear fusion could be an ideal future energy source. The fuel is abundant and its reserves are widely distributed on Earth. The reaction by-product, helium, is a harmless inert gas, therefore there will be no radioactive waste and no pollution of the atmosphere.

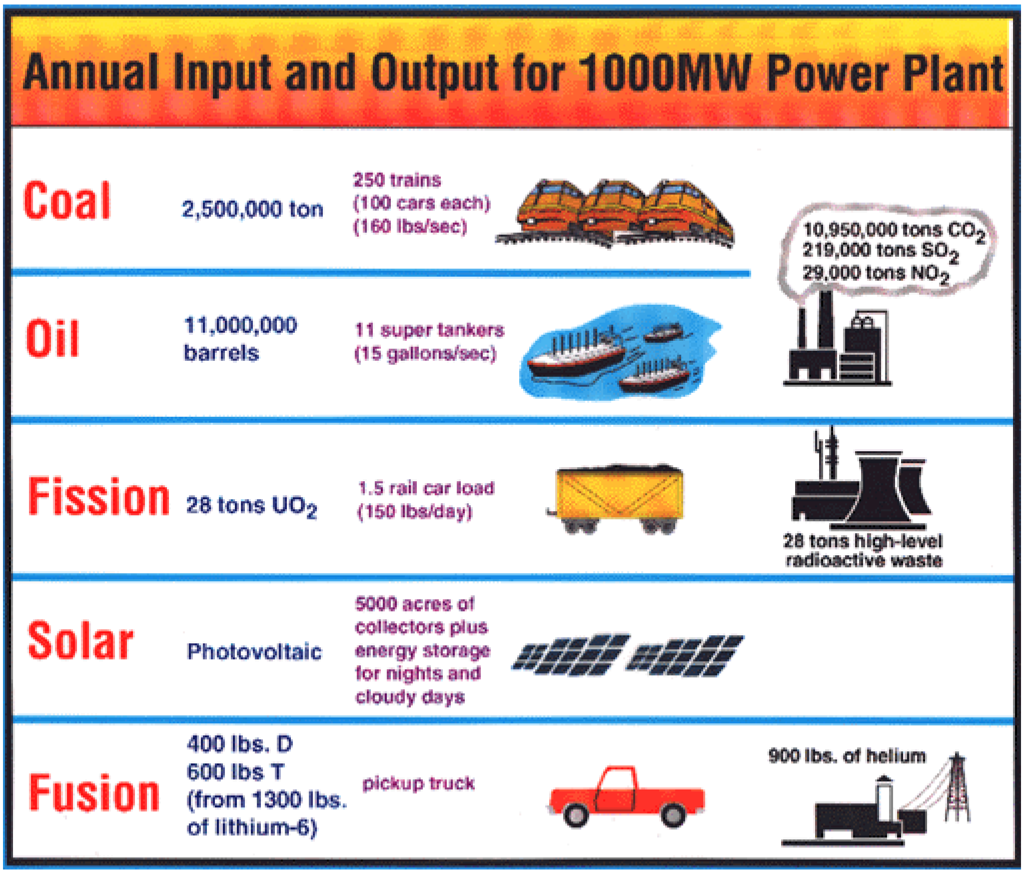

Figure 2.3: *Annual inputs and outputs of a 1000MW power plant depending on a type of fuel (taken from [7])*

2.2 Plasma

For fusion reaction to occur, it is necessary to bring the two nuclei very close together. It is therefore necessary to overcome their strong electrostatic repulsive force. The method which seems to be the most effective to increase the probability for the two nuclei of getting close enough to react is to warm their gas mixture. To ensure fusion in sufficient rate, temperatures of hundreds of millions Kelvins are needed. In these extreme temperatures, the gas is fully ionized and we refer to it as plasma or “the fourth state of matter“.

“Plasma is a quasi-neutral gas of charged and neutral particles, which shows a collective behaviour“[6].

Plasmas are quasi-neutral, which means that local charge concentrations or external potentials are shielded out on distances short enough in comparison with the plasma dimensions. Parameter which describes the rate of shielding in plasma is called the Debye length λ_D:

$$\lambda_D = \sqrt{\frac{1}{\sum_\alpha \frac{Q_\alpha^2 \cdot n_\alpha}{\varepsilon_0 \cdot k_B \cdot T_\alpha}}}\,, \tag{2.7}$$

where α denotes the type of particles (electrons, ions etc.), $\varepsilon_0 = 8.85 \cdot 10^{-12} kg^{-1} m^{-3} s^4 A^2$ is the permittivity of vacuum, $k_B = 1.38 \cdot 10^{-23} m^2 kg \cdot s^{-2} K^{-1}$ is the Boltzmann constant, T_α is the particles‘ temperature and n_α is the particles‘ density. Therefore the total positive charge contained in plasma is approximately equal to the absolute value of the total negative charge.

Collective behaviour of the plasma particles means that the particles movement and trajectories are influenced not only by local conditions, but also by conditions in other places of the plasma. Plasma is a gas ionized in such extent, that its properties and particle movement are determined mainly by the electromagnetic forces and only marginally by collisions with neutral atoms. More information about plasma and its properties can be found in [4],[6] and especially in [8].

2.3 Ignition

One of the most important questions is what conditions need to be ensured to gain positive power balance from the thermonuclear fusion. The released fusion power must be greater than power needed to heat and confine the plasma. The first man to formulate these conditions mathematically was British physicist John Lawson. His famous Lawson criterion pointed out that product of plasma density and energy confinement time must exceed certain value. Plasma density n is a number of ions per cubic metre and the energy confinement time τ_E describes the rate of plasma energy losses and is defined as a ratio of total energy W contained in plasma and total power of losses P_{loss} :

$$\tau_E = \frac{W}{P_{loss}} \tag{2.8}$$

For a DT fusion, the reaction products are helium nuclei (called alpha particles) and neutrons. In case of magnetic confinement of the plasma, the alpha particles, being charged, are trapped within the magnetic field. They pass their energy in collisions to the plasma particles thus heating the plasma. With the rise of temperature the rate of fusion reactions increases and therefore also alpha particles heating is greater. Ignition is a desired state, when the alpha particles deliver all the heating power needed and the reaction is self-sustaining. The criterion for ignition in magnetically confined plasmas is similar to the Lawson criterion:

$$n \cdot \tau_E > \frac{12}{\langle \sigma v \rangle} \cdot \frac{T}{E_\alpha} \quad [m^{-3}.s], \tag{2.9}$$

where n is the plasma ion density, τ_E the energy confinement time, $<\sigma v>$ describes the averaged reactivity (the probability of reaction per unit time per unit density, computed as a velocity averaged product of reaction cross section and relative velocity of ions [19]). T is the plasma temperature and E_α energy of one alpha particle (3.5MeV). The right side of the equation (2.9) is function of temperature only and this dependence has its minimum near 30*keV*.

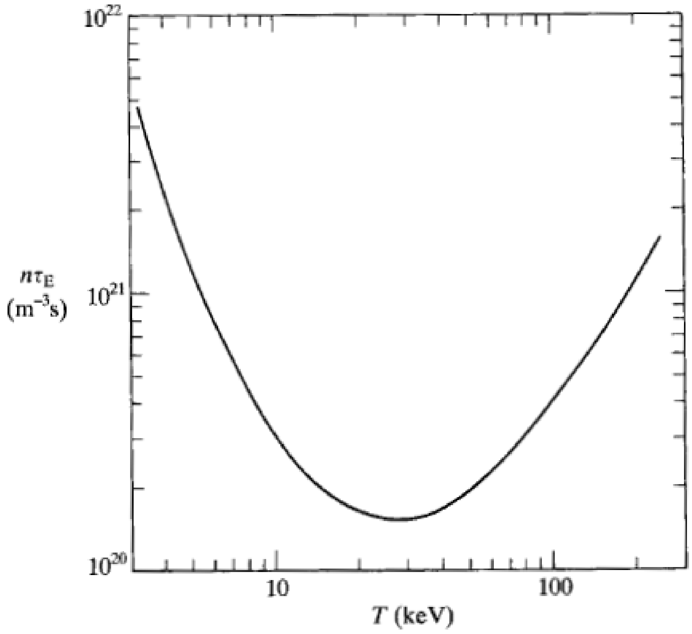

Figure 2.4: *The condition for ignition - dependence of the needed product of density and energy confinement time on temperature (for DT fusion) [39]*

However, because plasma averaged cross section $<\sigma v>$ and also the energy confinement time τ_E are functions of temperature, the ideal temperature to achieve ignition is lower. In the temperature range of 10-20*keV*, the ignition criterion for DT fusion can be written as:

$$n \cdot T \cdot \tau \ > 3 \cdot 10^{21} m^{-3} \cdot keV \cdot s \qquad (2.10)$$

The left side of equation (2.10) is sometimes referred as *fusion triple product*. [3][4][9]

2.4 Plasma confinement

There are generally two principles of confining hot plasmas with ambition of achieving the required conditions mentioned above. These are magnetic and inertial confinement.

Magnetic confinement:
Hot plasma contains charged particles, therefore can be confined by a strong magnetic field. Charged particles circle around the magnetic field lines with a specific radius called Larmor radius:

$$r_L = \frac{m \cdot v_\perp}{|q| \cdot B}, \qquad (2.11)$$

where m is the particle mass, $v_\perp$ is the particle velocity perpendicular to the magnetic field, q is the charge of the particle and B is the magnetic field.

Plasma is kept in a closed volume and its typical parameters are $\tau_E \sim 10^{-3} - 10^{0} s$ and $n \sim 10^{19} - 10^{21} m^{-3}$ (lower densities and very high energy confinement times).

Inertial confinement:
Very energetic laser pulses or particle beams symmetrically heat a target sphere of DT. The target implodes and in its centre the conditions for a fusion reaction are obtained. This approach features high densities of $n \sim 10^{31} m^{-3}$ and very short energy confinement of typically $\tau_E \sim 10^{-11} s$.

In linear magnetic field devices the end losses of particles and energy are too high, so it is necessary to enclose the magnetic field lines. Toroidally shaped devices satisfy this condition. However, in a system with toroidal magnetic field only, the magnetic field curvature and gradient result in an opposite vertical drift movement of ions and electrons and occurrence of electric current. Resulting electric field causes $\vec{E} \times \vec{B}$ drift in outward direction:

$$\vec{v}_E = \frac{\vec{E} \times \vec{B}}{B^2} \tag{2.12}$$

To avoid the particles quickly drift away, it is necessary to twist the magnetic field lines, so that the resulting magnetic field is helical. There are two main types of magnetic devices solving this problem: stellarators and tokamaks.
Stellarator uses external coils wound around the plasma torus to twist the magnetic field. Tokamak uses induced plasma current in toroidal direction to create poloidal magnetic field and therefore to twist the magnetic field.

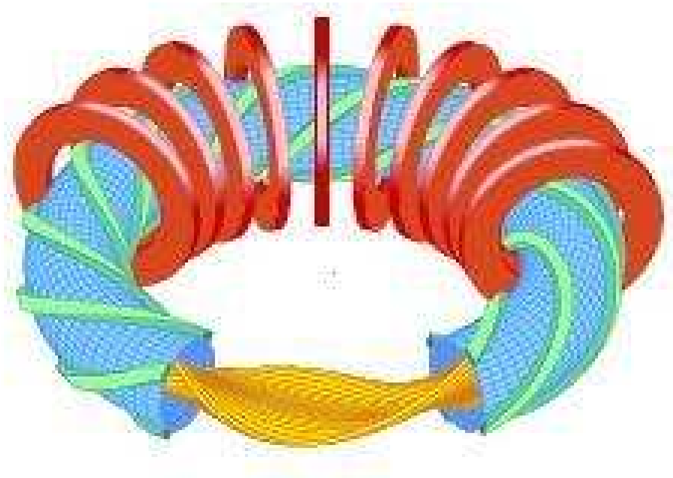

Figure 2.5: *Scheme of a classical stellarator. It consists of the toroidal field coils (red), independent helical coils (green) and the vacuum vessel (blue). [9]*

2.5 Tokamak

Tokamak (toroidalnaja kamera s magnitnymi katuškami) is the most advanced device confining hot plasma in the present fusion research. It was projected in the fifth decade of 20th century in Moscow, USSR. It is generally a toroidal shaped vacuum vessel with strong toroidal field and weaker poloidal field. Toroidal field is produced by coils surrounding the vacuum vessel. Plasma in tokamak acts as secondary single-turn winding of a transformer. Strong induced current heats the plasma and creates the poloidal magnetic field, thus twisting the toroidal field lines. Resultant helically shaped magnetic field lines cause that each particle spends similar time both in the high and low toroidal field regions. Therefore the drifts responsible for charge separation last only for a short time before being reversed and in time average their effect is cancelled. Additional outer poloidal field coils help to shape and position plasma.

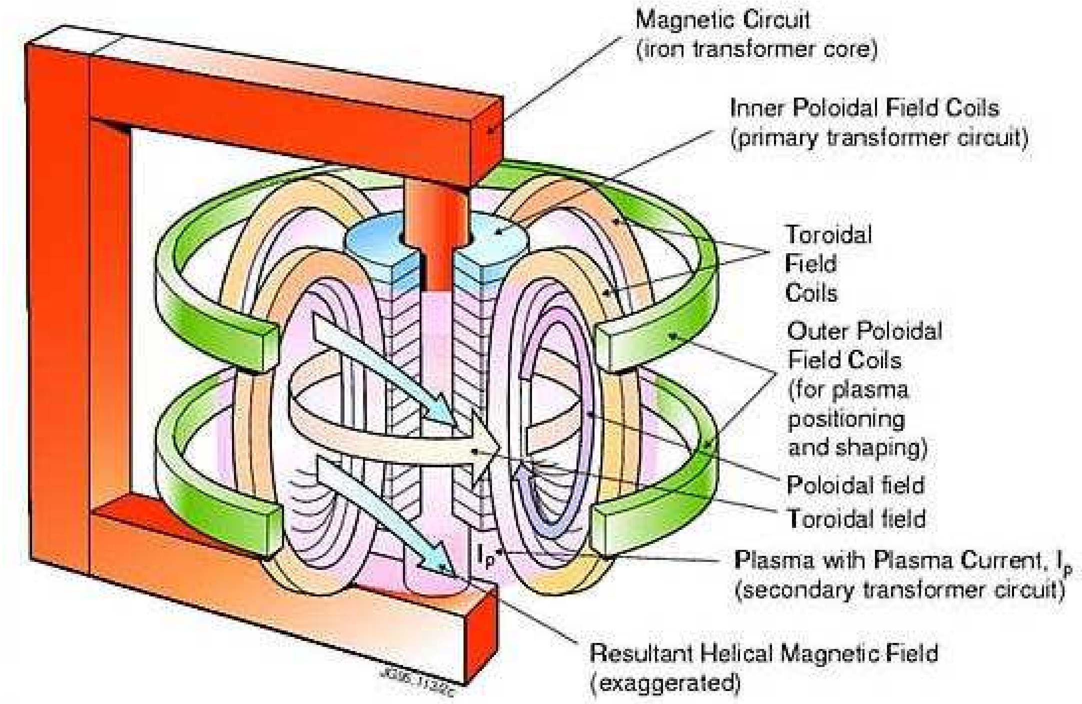

Figure 2.6: *Scheme of a tokamak [10]*

The vacuum vessel has two symmetry axes, major and minor. These axes characterize two basic directions: toroidal and poloidal. Basic tokamak geometrical parameters are major radius *R* and minor radius *a*. Major radius is a distance between major and minor axis and minor radius is a shortest distance between minor axis and edge of the vessel (see Fig 2.7). The helicity of magnetic field in a tokamak is described by a parameter called *safety factor q*. It is a number of toroidal turns of the magnetic field line needed to encircle one poloidal turn.

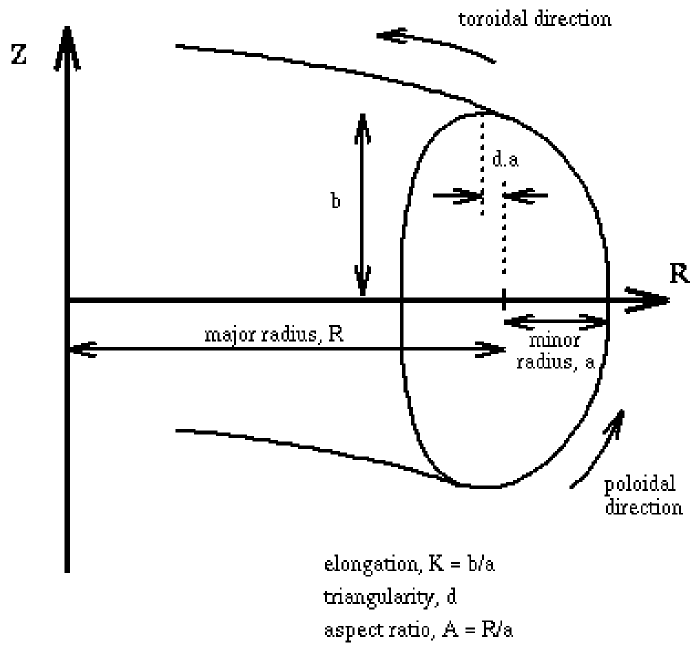

Figure 2.7: *Tokamak geometry [11]*

In a tokamak, continuous heat source must exist to initially heat the plasma to the needed temperatures and then to maintain these temperatures and balance the energy losses of plasma. There are several ways of heating the plasma in tokamak. Initial ohmic heating is caused by induced toroidal current I_p. However, as the plasma temperature rises, efficiency of this method of heating quickly decreases. This is caused by increasing plasma conductivity. Therefore additional heating methods must be used.

Neutral beam injection (NBI): Tangential injection of energetic neutral particles into the plasma column. Ions are accelerated and then neutralized, so they are not affected by the tokamak magnetic field and are able to access deeper parts of the plasma. There the neutral atoms are ionized, caught by the magnetic field and they pass their energy to the plasma particles via collisions.

Ion cyclotron resonance heating (ICRH): Emitted electromagnetic waves of certain frequency (tens of MHz) resonate with the cyclotron motion of the plasma ions. This method of heating has the advantage of being localised at a particular location.

Self-heating of plasma: As was already mentioned, alpha particles produced by the fusion reaction help to heat the plasma by collisions with plasma particles. The moment when all heating needed is delivered only by the alpha particles is called *ignition*.

Current research of the tokamak plasmas faces many problems. Plasmas are the source of numerous instabilities which lead to a deterioration of the energy and particle confinement. Also suitable materials of the components of a tokamak must be developed, to withstand extreme neutron and particle fluxes and magnetic fields and not to be source of impurities released into the plasma.

2.6 JET, ITER and future

JET (Joint European Torus) is the largest operating nuclear fusion facility in the world. It is located in Culham, United Kingdom. JET tokamak started to operate in 1983 and was the first fusion device to achieve a significant production of a fusion power. It holds several experimental records in fusion research, including *16MW* of peak fusion power.
The typical parameters of the JET tokamak are shown in the Tab. 2.1 below:

Plasma major radius	*2.96m*
Plasma minor radius	*2.10m* (vertical) *1.00m* (horizontal)
Toroidal magnetic field (on plasma axis)	$\leq 3.45T$
Plasma current	$\leq 4.8MA$
Additional heating power	$\leq 25MW$

Table 2.1: *Main JET tokamak parameters*

Experimental results on tokamaks showed, that conditions needed for ignition could be achieved by increasing the plasma dimensions (which especially leads to greater energy confinement time). After successful demonstration of physical feasibility of fusion by large tokamaks like JET, the need of a larger device capable of demonstrating the technological feasibility of fusion and provide the necessary data to design and operate the first electricity-producing fusion power plant has arisen. The international fusion community has designed a *next step* device, called ITER, to fulfil this task. In June 2005, it was decided to construct ITER in Cadarache, France and on 21st November 2006 a Joint Implementation agreement was signed, thus establishing the ITER organization. In the year 2007, the construction of ITER (international thermonuclear experimental reactor) tokamak has begun. ITER is an international project of seven participants: The European Union (represented by EURATOM), Japan, The People's Republic of China, India, the Republic of Korea, the Russian Federation and the USA. The construction costs of ITER are estimated as five billion Euro and another five billion Euros are estimated for its 20-year long operation, thus making it one of the most expensive research projects of our time. Its objectives are to achieve a steady-state burn of deuterium-tritium plasma producing 500MW of fusion power, achieve the power amplification factor Q = 10 (ratio of fusion power to the heating power) and to test the inner components facing high-heat and neutron fluxes. It should start its operation by the end of the year 2016. The possible success of ITER would lead to construction of DEMO, a fully functional prototype of a fusion power plant producing electricity and then to first commercial devices. [3]

3 Plasma equilibrium

3.1 From statistics to continuum

Plasma is a system consisting of several types of particles (electrons, ions, neutral atoms). Let us denote them by a subscript α. The probability density of occurrence of particle α is:

$$f_\alpha = f_\alpha(t, \vec{x}, \vec{v}_\alpha), \tag{3.1}$$

where $\vec{x}$ and $\vec{v}$ are phase space coordinates (vectors of position and velocity). The density probability function f_α is normalized to the number of particles α in the system:

$$\begin{aligned} &\int f_\alpha(t, \vec{x}, \vec{v}_\alpha) d^3\vec{v}_\alpha = n_\alpha(t, \vec{x}) \\ &\int f_\alpha(t, \vec{x}, \vec{v}_\alpha) d^3\vec{x} \cdot d^3\vec{v}_\alpha = N_\alpha(t) \end{aligned}, \tag{3.2}$$

where n_α is the particle density and N_α the number of particles α in the system. The density probability function f_α changes in time due to collisions of like and unlike particles:

$$\frac{d}{dt} f_\alpha(t, \vec{x}, \vec{v}_\alpha) = \sum_\beta S_{\alpha\beta}\ , \tag{3.3}$$

where the right side terms are called the Boltzmann collision integrals describing the particle collisions, α and β subscripts denoting the particle types. The total time derivation in (3.3) can be transcribed and the resulting equation in operator form written as:

$$\frac{\partial f_\alpha}{\partial t} + \left(\vec{v}_\alpha \cdot \vec{\nabla}_x\right) f_\alpha + \frac{1}{m_\alpha}\left(\vec{F}_\alpha \cdot \vec{\nabla}_v\right) f_\alpha = \sum_\beta S_{\alpha\beta}\ , \tag{3.4}$$

where $\vec{\nabla}_x = \left(\frac{\partial}{\partial x_1}, \frac{\partial}{\partial x_2}, \frac{\partial}{\partial x_3}\right)$ and $\vec{\nabla}_v = \left(\frac{\partial}{\partial v_1}, \frac{\partial}{\partial v_2}, \frac{\partial}{\partial v_3}\right)$ are gradients in positions and velocities, $\vec{F}_\alpha$ are the forces affecting the particles and m_α are the particle masses. The equation (3.4) is called the Boltzmann equation and it is the basic equation in statistics of disequilibrium processes. According to possible ways of expressing the collision integral, the altered Boltzmann equation can be called the Fokker-Planck equation (only binary Coulomb collisions), Vlasov equation (collisions neglected) etc.

Usually, the probability function information about the whole phase space is not needed and it is sufficient to know the development of dynamical variables in position and time only. Therefore it is possible to average the Boltzmann equation over velocities. The loss of information about the variable $\vec{v}_\alpha$ then leads from statistics to the equations of continuum. Let us multiply the Boltzmann equation (3.4) by a function of velocity $\phi_\alpha(\vec{v}_\alpha)$ and integrate over velocities. For electromagnetic interaction the force $\vec{F}_\alpha$ is the Lorentz force:

$$F_\alpha = Q_\alpha \cdot \left(\vec{E} + \vec{v}_\alpha \times \vec{B}\right), \tag{3.5}$$

where Q_α is the particle charge, $\vec{E}$ the electric field and $\vec{B}$ the magnetic field. The result of integration is then:

$$\frac{\partial}{\partial t}\left\langle n_\alpha \phi_\alpha \right\rangle_v + \vec{\nabla}_x \cdot \left\langle n_\alpha \phi_\alpha \vec{v}_\alpha \right\rangle - \frac{Q_\alpha}{m_\alpha}\left\langle n_\alpha \left(\vec{E} + \vec{v}_\alpha \times \vec{B}\right) \cdot \frac{\partial \phi_\alpha}{\partial \vec{v}_\alpha} \right\rangle_v = \int \phi_\alpha \sum_\beta S_{\alpha\beta} d^3 \vec{v}_\alpha \,, \tag{3.6}$$

where $\langle \ \rangle_v = \int f_\alpha d^3 \vec{v}_\alpha$. The equation (3.6) is called the Moment equation and it has a form of a continuity equation. The first term is a time derivative of density of an additive variable, the second term is a divergence of the flow of the variable, the third term describes the source terms from force fields and the right side of the equation describes the source terms due to collisions. Substituting $\phi_\alpha(\vec{v}_\alpha)$ in (3.6) by powers of velocity results in gaining the so called *moments of the Boltzmann equation*. The zero moment ($\phi_\alpha(\vec{v}_\alpha) = m_\alpha; Q_\alpha; 1$) is the conservation of mass, charge and number of particles. The first moment ($\phi_\alpha(\vec{v}_\alpha) = m_\alpha \vec{v}_\alpha$) is the momentum conservation law. The second moment ($\phi_\alpha(\vec{v}_\alpha) = \frac{1}{2} m_\alpha v_\alpha^2$) is the energy conservation law. Higher moments are not usually considered. [8]

3.2 Magnetohydrodynamics

Magnetohydrodynamics (MHD) is an approach to plasma within the frame of the continuum mechanics. The basic MHD equations are the moments of the Boltzmann equation mentioned above along with Maxwell equations for electromagnetic field. In MHD, the plasma is considered a conducting fluid (one or more), whose behaviour is affected dominantly by the magnetic field. There are more possible options of defining the initial presumptions of the MHD theory; in this text the following are given:

- *Plasma can be regarded as a continuum*: The collisions in plasma are dominant, the mean free paths of particles are much shorter than the dimensions of plasma and the mean collision time of particles is much shorter than the period in which the plasma is observed.
- *Plasma is quasi-neutral:* In every macroscopic plasma volume, there is the same number of positive and negative charge.
- *One fluid model:* Plasma can be regarded as a one fluid. If the lighter electrons escape from the system, they drag along the heavier ions by an electric field (ambipolar diffusion). The average velocities of the electron and ion parts of the plasma are almost equalized ($\vec{u}_e \approx \vec{u}_i$) and they are both approximately equal to the centre-of-mass velocity:

$$\vec{u} = \frac{\sum m_\alpha \vec{u}_\alpha}{\sum m_\alpha} \,. \tag{3.7}$$

The small difference in $\vec{u}_e$ and $\vec{u}_i$ leads to a current density flowing in the plasma:

$$\vec{j} = \sum Q_\alpha n_\alpha \vec{u}_\alpha \tag{3.8}$$

- *Non-relativistic plasma:* All kinds of particles have non-relativistic velocities
- *Low-frequency plasma:* The plasma phenomena are low-frequency and the displacement current in the Maxwell equations can be neglected.

The complete set of MHD equations then can be written:

$$\frac{\partial \vec{B}}{\partial t} = \frac{1}{\sigma \mu_0} \Delta \vec{B} + rot\left(\vec{u} \times \vec{B}\right), \tag{3.9}$$

$$\frac{\partial \rho}{\partial t} + div \rho \vec{u} = 0, \tag{3.10}$$

$$\rho \frac{\partial \vec{u}}{\partial t} + \rho\left(\vec{u} \cdot \vec{\nabla}_x\right)\vec{u} = -\vec{\nabla} p + \eta \Delta \vec{u} + (\varsigma + \eta / 3)\vec{\nabla}(div \vec{u}) + \vec{j} \times \vec{B}, \tag{3.11}$$

$$p = p(\rho). \tag{3.12}$$

The equation (3.9) is an equation for the magnetic field, (3.10) the equation of continuity, (3.11) the equation of motion for a viscous magnetized fluid (the famous Navier-Stokes equation) and (3.12) is some algebraic relation for pressure, which completes the set of equations. In these equations, σ is the plasma conductivity, $\mu_0 = 4\pi \cdot 10^{-7}\, kg \cdot m \cdot s^{-2} A^{-2}$ is the permeability of vacuum, ρ is the plasma mass density, *p* is the plasma pressure, η is the first viscosity and ζ is the second viscosity. [8]

3.3 The Grad-Shafranov equation

On short timescales the tokamak plasma shows a variety of oscillations and turbulent phenomena. On sufficiently long timescales the plasma behaviour is governed by gradual changes in the magnetic configuration, changes of the plasma heating, the diffusive losses etc. Let us consider situations, where there exists an intermediate timescale on which the tokamak plasma is in equilibrium. In equilibrium, the plasma pressure and the forces due to magnetic field must be equalized. When we start from the MHD equation of motion (3.11) and consider the equilibrium situation, in which the temporal derivatives are equal to zero, and if we additionally consider zero plasma flow ($\vec{u} = 0$), then the equation (3.11) can be rewritten as:

$$\vec{\nabla} p = \vec{j} \times \vec{B}, \tag{3.13}$$

which exactly expresses the equalization of the plasma tendency to extend due to its kinetic pressure and the Lorentz force binding the particles to the magnetic field lines. The ratio of the kinetic plasma pressure, averaged over the plasma volume, to magnetic pressure:

$$\beta = \langle p \rangle / \left(B^2 / 2\mu_0\right), \tag{3.14}$$

called the *beta parameter*, is an important characteristics of the plasma confinement.

For an axisymmetric system like tokamak (independence in the toroidal direction) it is convenient to rewrite the equilibrium equation (3.13). Before it is done, there are several ideas which should be noted:

- A scalar product of equation (3.13) with current density $\vec{j}$ or magnetic field $\vec{B}$ yields:

$$\begin{aligned} \vec{j}\cdot\vec{\nabla}p &= 0 \\ \vec{B}\cdot\vec{\nabla}p &= 0 \end{aligned}, \tag{3.15}$$

  which tells us, that both the current density and magnetic field are perpendicular to the plasma pressure gradient. This implies that electric currents in equilibrium flow on surfaces of constant pressure and the magnetic field lines also lie on that surface. It can be shown that in axisymmetric case these surfaces are tori.
- The flux integrals $\int\vec{B}\cdot d\vec{S},\int\vec{j}\cdot d\vec{S}$ ($d\vec{S}$ is a vector element of the surface, with a direction normal to the surface) have a constant value on these *p=const.* surfaces, as they lie on them and thus any part of the integral on the surface vanishes. These surfaces are therefore called *flux surfaces* or *magnetic surfaces* and can be labelled by the scalar fluxes. Moreover, p is also a function of fluxes only.
- The constraint $div\vec{B}=0$ (the Gauss's law for magnetism) implies that the magnetic field lines cannot cross each other. Therefore if one follows a magnetic field line around the torus, the ratio between the numbers of toroidal and poloidal revolutions of the field line converges to a constant q. The constant q is called the safety factor because of its importance in stability of a wide range of MHD modes. It is related to the average twist of the helical field on a magnetic surface.

On a magnetic surface, there are two topologically different types of curves: winding around the torus-shaped surface in poloidal or toroidal direction. If we chose a curve winding around the magnetic surface in the toroidal direction and integrate the poloidal component of the magnetic field B_p over the surface S enclosed by the curve, we get the *poloidal magnetic flux* ψ:

$$\psi=\int_S\vec{B}_p\cdot d\vec{S}\,. \tag{3.16}$$

Similarly, if we integrate the poloidal current density flowing through that surface, we get the total poloidal current flowing through the surface:

$$I_p=\int_S\vec{j}_p\cdot d\vec{S}\,. \tag{3.17}$$

Both these functions are constant on the magnetic surface. In order to describe axisymmetric MHD equilibria, the cylindrical coordinates (R,ϕ,z) are used, where ϕ is the angle of symmetry (toroidal angle), R measures the distance to the axis of symmetry (the major radius) and z the height over the axis of symmetry (see Fig. 3.1). In cylindrical coordinates, the Gauss's law for magnetism $div\vec{B}=0$ has the following form:

$$\frac{1}{R}\frac{\partial}{\partial R}(RB_R)+\frac{1}{R}\frac{\partial B_\phi}{\partial \phi}+\frac{\partial B_z}{\partial z}=0\ . \tag{3.18}$$

As the poloidal magnetic flux ψ is constant on the magnetic surfaces, it must satisfy equation:

$$\vec{B}\cdot\vec{\nabla}\psi=0\ . \tag{3.19}$$

Considering the equations (3.18) and (3.19), the magnetic field can be written in cylindrical coordinates as:

$$\begin{aligned} B_\phi &= \frac{\mu_0 I_p}{2\pi R} \\ B_R &= -\frac{1}{2\pi R}\frac{\partial\psi}{\partial z}\ . \\ B_z &= \frac{1}{2\pi R}\frac{\partial\psi}{\partial R} \end{aligned} \tag{3.20}$$

The poloidal flux function ψ is arbitrary to an additive constant, which may be chosen for convenience.

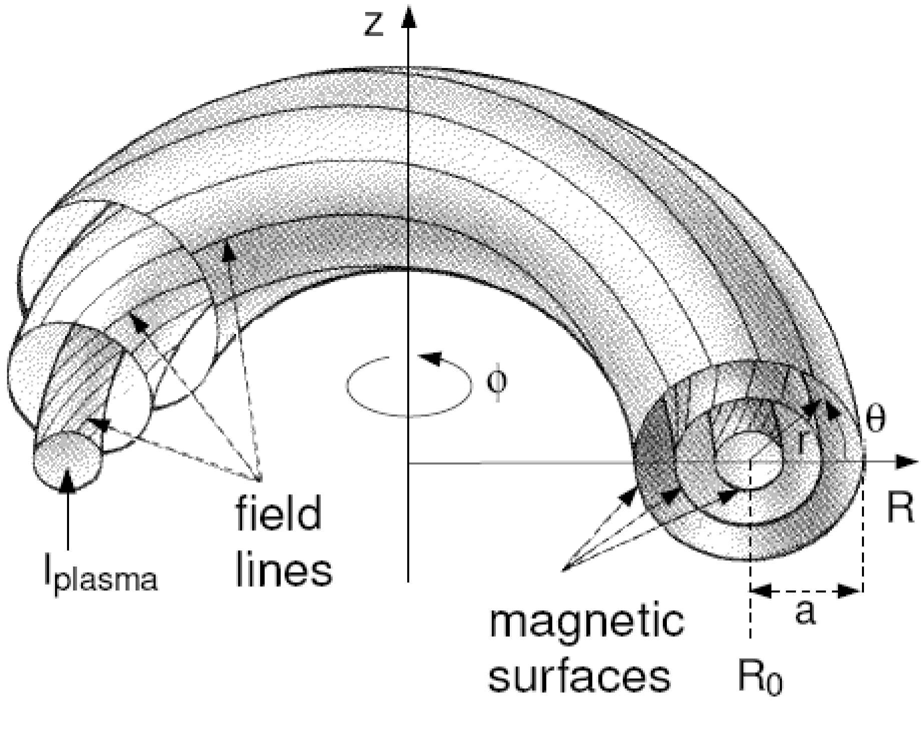

Figure 3.1: *Coordinates used for the Grad-Shafranov equation and the magnetic surfaces topology. [9]*

Using these equations (3.20), the force balance equation (3.13) may be rewritten as:

$$-\Delta^*\psi=\mu_0(2\pi R)^2\,p(\psi)'+\mu_0^2 I_p(\psi)I_p(\psi)'\ , \tag{3.21}$$

where the operator Δ^* is called the Grad-Shafranov operator and defined as:

$$\Delta^* = -\left[R\frac{\partial}{\partial R}\left(\frac{1}{R}\frac{\partial \psi}{\partial R}\right) + \frac{\partial^2 \psi}{\partial z^2} \right] \tag{3.22}$$

and the prime denotes the derivatives $\frac{\partial}{\partial \psi}$. The equation (3.21) is called the *Grad-Shafranov equation* and it is an elliptic second order nonlinear differential equation for ψ. To solve it, one has to specify $p(\psi)$, $I_p(\psi)$ and then compute the $\psi(R,z)$. Usually, one will specify boundary conditions. If the plasma is surrounded by a perfectly conducting vacuum vessel, the vessel is a flux surface $\psi = const.$. The tokamak experiments throughout the world use mainly the so called *EFIT code* to obtain a solution of the equation (3.21) in the tokamak plasma consistent with experimental measurements.

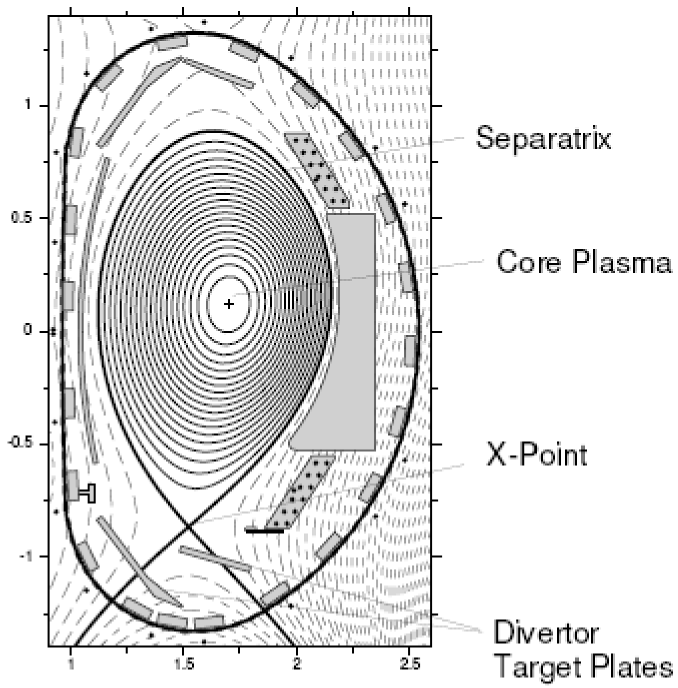

Figure 3.2: *Typical poloidal cross section of a tokamak using divertor configuration. The contours show the poloidal flux function ψ. [9]*

From the Fig 3.2, it can be observed that the flux surfaces are not centred to one axis, but they are slightly shifted in the outward direction. This shift is called the *Shafranov shift* and it is caused due to forces trying to expand the torus radially outward (the kinetic plasma pressure and the expansion force of a current loop due to the $\vec{j} \times \vec{B}$ force). The last closed flux surface is called *separatrix* Plasma particles accessing the separatrix flow along the magnetic field lines onto the material plates at the bottom of the vessel. This configuration is called a magnetic *divertor*. [4][9][21]

3.4 Flux coordinates

In equilibrium calculations, but also in the modelling of plasma transport and in stability analyses, the so called *flux coordinates (r,θ,ϕ)* are of great importance. Here ϕ is the usual toroidal angle, $r = r(\psi)$ labels the flux surfaces and θ is used for the poloidal angle. $r(\psi)$ can be the poloidal magnetic flux ψ itself or it can be chosen to closely resemble the minor radius (usually $\sqrt{\psi}$). It is usually normalized to be zero in the plasma centre and 1 on the separatrix. The differences between its definitions are not too important. The various definitions of θ, however, are each convenient in very specific applications:

- A proper geometrical angle.
- Coordinates, in which the field lines appear straight (the safety factor $q(\psi) = \dfrac{d\phi}{d\theta}$ is constant on every flux surface).
- An orthogonal coordinate system (thus $\vec{\nabla} r \cdot \vec{\nabla}\theta = 0$).

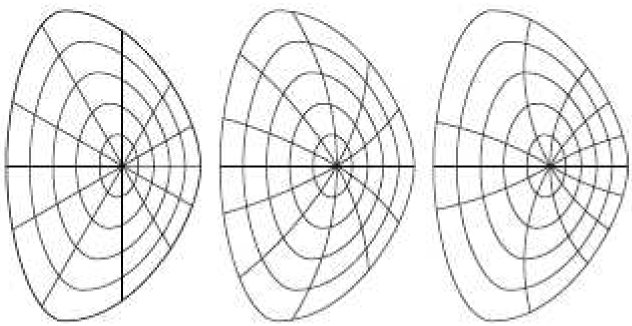

Figure 3.3: *Flux coordinate systems (left: proper poloidal angle, centre: straight field lines, right: orthogonal coordinates). [21]*

Most important application of the poloidal flux is that it can be used as a generalisation of the minor radius coordinate. Here the flux is first normalised so that on magnetic axis it is equal to *0* and on separatrix equal to *1*:

$$\psi_N = \frac{\psi - \psi(axis)}{\psi(sep) - \psi(axis)}. \tag{3.23}$$

Then the normalised minor radius is defined as $\rho = \sqrt{\psi_N}$. For plasma with circular cross section and large aspect ratio $\rho \to r/a$ (where a is the tokamak minor radius). Such definition is used in our analysis (chapter 7).

4 Transport in tokamaks

4.1 Transport equations

For a single particle in tokamak the confinement would be perfect. However, in reality collisions, drifts, MHD instabilities and turbulence lead to a radial transport of particles and energy across the magnetic field lines. This radial transport determines the particle and energy confinement times τ_p and τ_E and therefore it is one of the most important plasma parameters.

We define the particle flux $\vec{\Gamma}_\alpha$ as the number of particles α (electrons, ions or neutral atoms) passing through a magnetic surface per unit area and time. For $\vec{\Gamma}_\alpha$ the following presumption (the Fick's law) is made:

$$\vec{\Gamma}_\alpha = -D_\alpha \vec{\nabla} n_\alpha - n_\alpha \cdot \vec{v}_\alpha \, , \tag{4.1}$$

which says that it has a diffusive part driven by a gradient of particle density n_α and characterized by the diffusion coefficient D_α and a convective part due to directed motion $\vec{v}_\alpha$. If the velocity $\vec{v}_\alpha$ is positive, then this term describes an inward pinch.

The equation of continuity says that a change of density in any part of the system is due to inflow and outflow of material into and out of that part of the system, no material is created or destroyed. Mathematically expressed:

$$\frac{dN_\alpha}{dt} = -\oint_S \vec{\Gamma}_\alpha d\vec{S} \, , \tag{4.2}$$

where N_α is a number of particles α contained in the system and S is an enclosed surface encircling the system. We are able to further modify this equation by using the Gauss's law:

$$N_\alpha = \int_V n_\alpha \cdot dV \qquad\qquad \oint_S \vec{\Gamma}_\alpha d\vec{S} = \int_V \left(div \vec{\Gamma}_\alpha \right) dV \, , \qquad (4.3)\ (4.4)$$

where V is a volume enclosed by the surface S. Therefore we can write the resulting equation in a differential form:

$$\frac{\partial n_\alpha}{\partial t} = -div \vec{\Gamma}_\alpha \tag{4.5}$$

In reality, this equation contains an additional term, which describes the change of plasma density due to ionisation or recombination S_α:

$$\frac{\partial n_\alpha}{\partial t} = -div\vec{\Gamma}_\alpha + S_\alpha \tag{4.6}$$

If we put the equations (4.1) and (4.6) together, we gain the final diffusion equation:

$$\frac{\partial n_\alpha}{\partial t} = div\left(D_\alpha \vec{\nabla} n_\alpha\right) + div\left(n_\alpha \cdot \vec{v}_\alpha\right) + S_\alpha \tag{4.7}$$

Heat flux $\vec{q}_\alpha$ is defined as the flow of particle kinetic energy per unit of area per unit of time. It is driven by the temperature gradient and it can be expressed by the following form (the Fourier's law):

$$\vec{q}_\alpha = -\chi_\alpha \vec{\nabla} T_\alpha , \tag{4.8}$$

where χ_α is the thermal diffusion coefficient (thermal conductivity) and T_α temperature of the species α. Similarly to the previous considerations about the particle diffusion, a heat equation can be derived:

$$\frac{\partial T_\alpha}{\partial t} = div(\chi_\alpha \vec{\nabla} T_\alpha) , \tag{4.9}$$

for a case with no internal heat generation in the plasma.

It must, however, be mentioned that the equations derived above are but a simplification of the real phenomena. In reality, both the particle and the heat flux are driven by gradients of more than one thermodynamic quantity (for example particle flux may appear due to thermal or electric potential gradient etc.). The flux of a specific particle type α is also dependent on the gradients of thermodynamic quantities of other particles. Also note that in anisotropic magnetized tokamak plasma these diffusion coefficients are tensors themselves. [4][8][9]

4.2 Classical diffusion

In a magnetized plasma we distinguish between transport coefficients parallel and perpendicular to the magnetic field. Diffusion parallel to the magnetic field lines is unaffected by the magnetic field and is generally much bigger than the perpendicular diffusion. The magnetic confinement properties, however, are determined by the perpendicular diffusion coefficient.

The simplest way of computing the diffusion coefficient comes from the random-walk assumption. We assume that due to Coulomb collisions with other particles, the particle makes a step Δx perpendicular to the magnetic field after a time Δt. The step can be made in both directions with equal probability and the diffusion coefficient of this process is following:

$$D_\alpha \approx \frac{{\Delta x_\alpha}^2}{\Delta t_\alpha} \tag{4.10}$$

To get the diffusion coefficient, it is necessary to evaluate Δx_α and Δt_α. Δx_α, being the characteristic step size in the random walk, is the particle mean free path l_{mfp}. Δt_α is an average time which it takes for a particle to change its direction due to collisions by *90°*. It is the inverse value of the particle collision frequency ν and it differs for electron-electron (ee), ion-electron (ie), electron-ion (ei) and ion-ion collisions (ii) (there the first index denotes the incident, scattered particle and the second index the target, stationary particle). The difference between these frequencies comes from the large value of ion and electron mass ratio. Assuming approximately the same electron and ion temperatures, *90°* scattering made up by many small angle scatterings and purely hydrogen plasma, the rates of the collision frequencies can be estimated as follows:

$$\nu_{ee} : \nu_{ei} : \nu_{ii} : \nu_{ie} = 1:1:\left(m_e / m_i\right)^{1/2} : \left(m_e / m_i\right). \tag{4.11}$$

$$\nu_{ee} \approx \nu_{ei} \propto \frac{ne^4}{\sqrt{m_e} T_e^{\ 3/2}}. \tag{4.12}$$

In the so-called *classical approach*, we take Δx_α to be the Larmor radius $r_{L,\alpha}$ (2.11).

The location $\vec{R}_\alpha$ of the guiding centre of the gyro-orbit is following:

$$\vec{R}_\alpha = \frac{\vec{p}_\alpha \times \vec{B}}{q_\alpha B^2}, \tag{4.13}$$

where $\vec{p}_\alpha$ is the particle momentum, $\vec{B}$ is the magnetic field and q_α is the charge of the particle. In a collision, momentum balance requires equality of $\Delta\vec{p}_\alpha = -\Delta\vec{p}_\beta$. Therefore for collisions of like particles (ions-ions, electrons-electrons) $\Delta\vec{R}_\alpha = -\Delta\vec{R}_\beta$ and these collisions do not contribute to particle transport (only to a heat transport, as a hot particle may change place with a cold one). The situation changes for electron-ion collisions, where $q_i = -q_e$ (for a purely hydrogen plasma), $\Delta\vec{p}_i = -\Delta\vec{p}_e$ and so $\Delta\vec{R}_i = \Delta\vec{R}_e$. The diffusion is *ambipolar,* because in a collision the electrons and ions make a step of equal magnitude and direction:

$$D_{e,class} = \nu_{ei} \cdot r_{L,e}^2 = \nu_{ie} \cdot r_{L,i}^2 = D_{i,class} \approx \frac{k_B T_{e,\perp} m_e}{e^2 B^2} \nu_{ei}, \tag{4.14}$$

where $k_B = 1.38 \cdot 10^{-23} m^2 kg \cdot s^{-2} K^{-1}$ is the Boltzmann constant and $T_{e,\perp}$ electron temperature perpendicular to the magnetic field.
Similar arguments can be applied for the thermal conductivities χ_α to derive a relation:

$$\chi_{i,class} = \left(m_i / m_e\right)^{1/2} \chi_e \approx 40 \chi_{e,class}. \tag{4.15}$$

However, experimentally determined diffusion coefficients are larger by a factor of approximately 10^5. Also, the electron heat conductivity is found to be comparable to that of ions. Therefore the classical diffusivity cannot be the dominant transport process in the tokamak plasma. [4][8][9][20]

4.3 Neoclassical diffusion

In a *neoclassical approach* to transport, the effects of toroidal geometry are considered. There are two main differences to classical transport theory:

- $|B|$ is not constant along a magnetic field line. Plasma particle which does not have a sufficient ratio of $v_\perp/v_\parallel$, where $v_\perp$ and $v_\parallel$ denote the particle velocity components perpendicular and parallel to the magnetic field, will be reflected back. Therefore we distinguish between two types of particles: trapped and passing. The electrical conductivity of plasma is lowered in a neoclassical theory, because the trapped particles do not contribute to the toroidal current
- ∇B and curvature drift cause that a trapped particle deviates from the magnetic surface and its orbit projected into a poloidal plane has a banana shape. These orbits are therefore called *banana orbits* (see Fig 4.1).

The fraction of the trapped particles on a flux surface is $N_t / N = \sqrt{2\varepsilon}$, where $\varepsilon = r / R$ is the inverse aspect ratio of the flux surface (r and R are the minor radius and major radius).

The width of the banana orbit is given by $r_B = \dfrac{r_L q}{\sqrt{\varepsilon}}$, where q is the safety factor. For trapped particles, an effective collision frequency is introduced $\nu_{eff} \approx \dfrac{\nu}{2\varepsilon}$, where ν is any of the collision frequencies from (4.12). An important parameter is the ratio $\nu_* = \nu_{eff} / \nu_t$, where ν_t is the inverse of time, which it takes for a particle to transit the banana. Therefore ν_* tells us whether the trapped particle is able to complete the banana orbit between two consequent collisions.

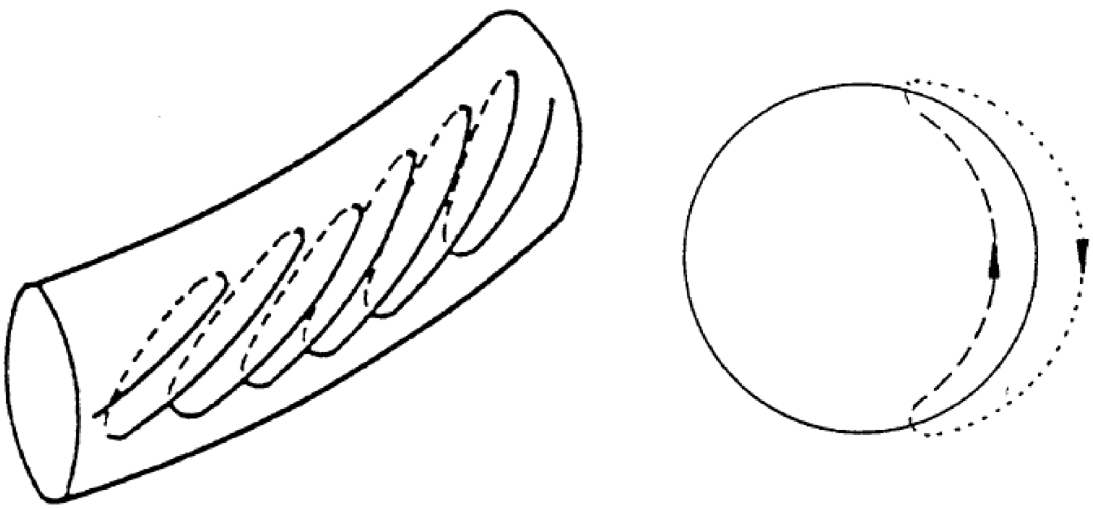

Figure 4.1: *Banana orbits in toroidal devices [9].*

According to the parameter ν_*, the neoclassical transport can be divided into three regimes:

- *Pfirsch-Schlüter regime:* $\nu_* > 1$, the trapped particles are scattered before they can complete the banana orbit. The diffusion coefficient is then determined as:

$$D_{PS} = q^2 r_L^2 \nu = q^2 D_{class} . \tag{4.16}$$

  As the safety factor *q* value ranges usually from *2* to *5*, the diffusion is increased.

- *Banana regime:* $\nu_* < \varepsilon^{3/2}$, the trapped particles are able to follow their banana orbit several times before they are scattered. Thus for a fraction $\sqrt{2\varepsilon}$ of particles, the characteristic step is r_B and collision frequency is ν_{eff} :

$$D_B \approx \sqrt{2\varepsilon} r_B^2 \nu_{eff} \approx \frac{r_L^2 q^2}{\varepsilon^{3/2}} \nu = \frac{q^2}{\varepsilon^{3/2}} D_{class} . \tag{4.17}$$

  For example for values $\varepsilon = 1/3$ and $q = 5$ this yields $D_B = 130 D_{class}$.

- Plateau regime: $\varepsilon^{3/2} < \nu_* < 1$, the diffusion coefficient in this region is independent on the collision frequency ν. The diffusion coefficient is between the two regimes above.

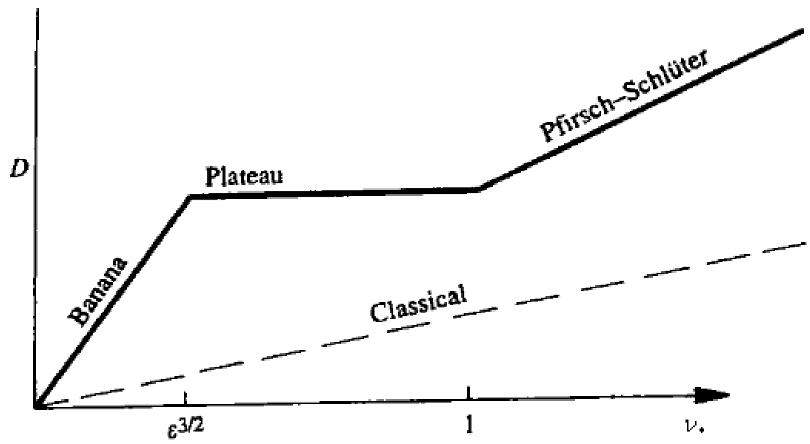

Figure 4.2: *Neoclassical diffusion coefficients [4].*

These neoclassical effects can increase the diffusion coefficient by a factor of 10^2. But it still cannot explain the experimental results. The real transport is called *anomalous* and it is the result of turbulences in plasma [4][9].

4.4 Transport coefficients

The typical diffusivities measured on tokamaks are:

- χ_i, χ_e **~ 1 m^{2}s^{-1}**

- $\boldsymbol{D \sim \frac{1}{4}\chi_e}$

where D is a diffusion coefficient (same for both species as the diffusion is ambipolar). The typical neoclassical values for diffusivities are generally much lower:

- $\boldsymbol{\chi_{i,neo} \sim 0.3\ m^2 s^{-1}}$
- $\boldsymbol{\chi_{e,neo} \sim D_{neo} \sim (m_e/m_i)^{1/2} \chi_{i,neo}}$

Therefore generally

- $\boldsymbol{\chi_i \sim 1\text{-}10\ \chi_{i,neo}}$
- $\boldsymbol{\chi_e \sim 10^2\ \chi_{e,neo}}$
- $\boldsymbol{D \sim 10\text{-}10^2\ D_{neo}}$

In experiments, the values of D, χ_i can approach the neoclassical values in the plasma core region or during a high confinement operation (H-mode, internal transport barrier...), but χ_e is almost always anomalous. [4]

4.5 Anomalous transport

The turbulence-driven anomalous transport is caused by fluctuations in the plasma. These fluctuations may be electrostatic or electromagnetic and are supposed to be an effect of one or more microinstabilities of the tokamak plasma. Macroscopic MHD instabilities like sawteeth, magnetic islands or ELMs are also an important source of the anomalous transport.

In the following text, to simplify the equations and avoid confusion, the subscripts denoting the different species are omitted if not necessary.

For a fluctuating quantity f we may write:

$$f = \langle f \rangle + \delta f\ , \tag{4.18}$$

where $\langle\ \rangle$ means averaging over a flux surface. The turbulent fluctuations result in $\vec{E} \times \vec{B}\, drift$ velocity $\delta v_\perp$ perpendicular to the flux surface:

$$\delta v_\perp = \delta E_\perp / B_T\ , \tag{4.19}$$

where $\delta E_\perp$ is the electric field fluctuation perpendicular to the flux surface and B_T is the toroidal magnetic field. This velocity combines with density fluctuations δn to produce a convective particle flux Γ:

$$\Gamma = \langle d v_\perp \delta n \rangle\ , \tag{4.20}$$

where $\langle\ \rangle$ means again averaging over a flux surface. The particle flux (4.20) must be then averaged also in time as the fluctuations are also time-dependant. The time average must be done over a time interval higher than all characteristic times in the plasma (electron and ion plasma frequency, electron and ion cyclotron frequency...). Therefore the time and space correlation between fluctuations plays an important role. For a turbulent heat flux the temperature fluctuations δT play a role:

$$q = 3/2nk_B \langle \delta v_\perp \delta T \rangle , \tag{4.21}$$

where n is the equilibrium density on the flux surface. In case of magnetic fluctuations δB associated with a change in magnetic topology, the perturbed velocity $\delta v_{//}$ parallel to the magnetic field and the perturbed radial component of the magnetic field δB_r give rise to a particle flux:

$$\Gamma = \frac{n}{B_T} \langle \delta v_{//} \delta B_r \rangle . \tag{4.22}$$

The fluctuations δn, δT_e and the electric potential fluctuation $\delta\phi$ at the edge of plasma can be measured by Langmuir probes and the magnetic fluctuation δB can be measured by the Mirnov coils. In experiments is observed that $\delta n / n$, $\delta T_e / T_e$ and $e\delta\phi / k_B T_e$ rise quickly towards the plasma edge, where they can reach values *~50%*. On the other hand, the edge plasma value of $\delta B / B$ is usually small, typically *~10^{-4}*. The internal density fluctuations can be much lower falling to *~1%*. The plasma potential fluctuations in the core follow approximately a relation $e\delta\phi / k_B T_e \approx \delta n / n$.

It is usual to perform a spatial Fourier transform of the fluctuations and observe their wave numbers $k_\perp$ and $k_{//}$ perpendicular and parallel to the magnetic field. The spectrum $S(k_\perp)$ is dominated by wavelengths ($\lambda = 2\pi / k$) greater than the ion Larmor radius $r_{L,i}$. In the azimuthal (poloidal) direction, the spectrum is peaked in the region $k_\perp \cdot \rho_s \leq 0.3$, where ρ_s is the ion Larmor radius at the electron temperature. For spectrum $S(k_{//})$ of wave numbers parallel to the magnetic field, the typical values are $k_{//} \cdot L \approx 1$, where L is the connection length around the torus ($L = qR$, where q is the safety factor and R the major radius). The characteristic frequencies of the fluctuations are ~ *100kHz*. [4]

Transport due to electrostatic fluctuations

As was mentioned in the previous paragraph, it is usual to perform a Fourier transform of the fluctuations $\delta f(t, \vec{x}) \leftrightarrow \delta f_k(\omega, \vec{k})$:

$$\delta f(t, \vec{x}) = \sum_k \delta f_k e^{i(\vec{k}\vec{x} - \omega t)} , \tag{4.23}$$

where $\vec{k}$ is the wave number (wave vector) and ω is the angular frequency. If the electrostatic potential fluctuation $\delta\phi$ is present, it causes $\vec{E} \times \vec{B}$ drift velocity δv. For a particular component $\delta\phi_k$ this velocity may be written as:

$$\delta\vec{v}_k = -i\frac{\delta\phi_k}{B}\vec{k} \tag{4.24}$$

and its component perpendicular to the magnetic field $\vec{B}$ as:

$$\delta\vec{v}_{k,\perp} = -i\frac{\vec{k}\times\vec{B}}{B^2}\delta\phi_k . \tag{4.25}$$

If this particle velocity persists for a so called *correlation time* τ_k, it leads to a radial displacement of the particle $\delta r_k \approx \delta v_{k,\perp}\tau_k$. A random walk estimate for the turbulent diffusion driven by electrostatic fluctuations is then given as:

$$D = \sum_k \frac{\left(\delta r_k^2\right)}{\tau_k} = \sum_k \left(\frac{k_\perp \delta\phi_k}{B}\right)^2 \tau_k . \tag{4.26}$$

The correlation time is determined by the process which most rapidly limits the radial drift velocity $\delta v_{k,\perp}$. The main possible processes determining τ_k are:

- The time variation of the fluctuation determined by ω_k: $\tau_k \sim 1/\omega_k$.
- The time for a particle to move along a parallel wavelength of the fluctuation: $\tau_k \sim 1/k_{//}v_{//}$.
- The time for magnetic drifts (drifts of magnetic field lines) to carry the particle along a perpendicular wavelength of the fluctuation: $\tau_k \sim 1/\omega_d$.
- The time for collisions to change the particle orbit: $\tau_k \sim 1/\nu$, where ν is the collision frequency of particles.
- The time for a turbulent velocity δv_k to carry the particle along a perpendicular wavelength: $\tau_k \sim 1/\Omega_k$, where $\Omega_k = k_{//}\delta v_k$.

Therefore for a low level fluctuations $\Omega_k << \omega_{eff,k}$, where $\omega_{eff,k} = \max(\omega_k, k_{//}v_{//}, \omega_d, \nu)$, the equation (4.26) can be rewritten as:

$$D = \sum_k \frac{1}{\omega_{eff,k}}\left(\frac{k_\perp \delta\phi_k}{B}\right)^2 \tag{4.27}$$

and $D \propto (\delta\phi)^2$. For higher level of fluctuations $\Omega_k \geq \omega_{eff,k}$ the equation (4.26) can be rewritten as:

$$D = \sum_k \frac{\delta\phi_k}{B} \tag{4.28}$$

and $D \propto \delta\phi$.[4]

Transport due to magnetic fluctuations

Magnetic fluctuations $\delta\vec{B}$ affect the structure of the magnetic surfaces and can produce ergodic magnetic fields. The motion of plasma particles along these magnetic field lines may then lead to their radial transport and losses. A radial magnetic field perturbation δB_r at a rational surface at radius r_{mn}, where the safety factor $q = m/n$ (*m*, *n* are identified as poloidal and toroidal mode), leads to a creation of a magnetic island of width:

$$w_{mn} = \sqrt{\frac{L_s r_{mn}}{m} \frac{\delta B_r}{B}}\,, \tag{4.29}$$

where $L_s = \dfrac{Rq^2}{r\dfrac{dq}{dr}}$ is called the magnetic shear length, *R* is the major radius and *r* is the minor radius. With increasing level of the magnetic fluctuations, an increasing part of the regions between resonant surfaces becomes ergodic. This behaviour is quantified by a parameter α:

$$\alpha = \frac{\sum_{m,n} w_{m,n}}{\Delta r}\,, \tag{4.30}$$

where the sum is over all modes *m, n* with rational surfaces in interval of radii Δr. When $\alpha \gg 1$, many islands overlap and the behaviour of the magnetic field lines becomes stochastic. In this case a radial diffusion of the field lines can be described by a magnetic field line diffusion coefficient D_M. If the radial field perturbation remains in the same direction over a so called *correlation length* L_c, then the field line takes a radial step:

$$\delta r \approx \frac{\delta B_r}{B} L_c\,. \tag{4.31}$$

A random walk estimate for the magnetic field line diffusion coefficient can be made:

$$D_M = \sum_k \frac{(\delta r_k)^2}{L_{ck}} = \sum_k \left(\frac{\delta B_{rk}}{B}\right)^2 L_{ck}\,. \tag{4.32}$$

For a weak turbulence the correlation length $L_{ck} \sim 1/k_{//} \sim Rq$ and $D_M \propto (\delta B_r)^2$.

Assuming collisionless plasma, where the mean free path l_{mfp} exceeds the correlation length $l_{mfp} > L_c$, a particle can move freely along the radially diffusing magnetic field line with velocity $v_{//}$ for a collision time τ_c. So it makes a radial step $\delta r = \sqrt{D_M l_{mfp}}$. The diffusion coefficient for particles can then be estimated as:

$$D = \frac{(\delta r)^2}{\tau_c} = \frac{D_M l_{mfp}}{\tau_c} = v_{//} D_M\,. \tag{4.33}$$

For a more collisional plasma, where $l_{mfp} < L_c$, the particle collisionally diffuses along the magnetic field lines with a radial step $\delta r \sim (\delta B_r / B) l_{mfp}$ in a collision time τ_c. The diffusion coefficient for particles can in this case be estimated as:

$$D = \left(\frac{\delta B_r l_{mfp}}{B} \right)^2 \frac{1}{\tau_c} = D_{//} \left(\frac{\delta B_r}{B} \right)^2, \tag{4.34}$$

where $D_{//} = \left(l_{mfp}^2 / \tau_c \right)$ is the collisional diffusion coefficient parallel to the magnetic field lines. [4]

In this chapter, information mainly from [4] and [9] were used. Especially [4] contains a very profound information about the transport in tokamaks.

5 Pellet fuelling

5.1 *Introduction*

The magnetic confinement of plasma in tokamaks is not perfect, as the particles are lost continuously and the plasma particle content would decrease on a characteristic timescale called the particle confinement time τ_p, if the fuel is not replaced. The most common and simplest method of plasma refueling is external gas puffing. It is a way of edge plasma fuelling. The neutral gas of deuterium and/or tritium is simply pumped into the vacuum vessel. This leads, however, to particle source profiles concentrated around the plasma boundary. In this region, there is a strong outward diffusion and consequently low particle confinement time and therefore fuelling efficiency attained by gas puffing is quite low. In larger devices and hotter and denser plasmas, only a small fraction of neutral gas particles will be able to penetrate across the separatrix and it will not be possible to use gas puffing as a primary fuelling method. Neutral beam injection used for heating tokamak plasmas delivers very energetic neutral particles into the plasma column. These particles are usually deuterium atoms, therefore this heating method provides also deep plasma refueling. However, attempting to refuel the plasma by NBI injection is very energy inefficient. The power required for sufficient refueling rate is enormous. Therefore for present day and future devices, so called pellet injection has become a leading technique for plasma fuelling. Pellet injection will also be crucial for ITER performance.
Solid pellets of frozen deuterium and tritium with diameters of *1-6mm* are used to refuel the plasma. Pellets are injected at high speeds (hundreds of meters per second) into the plasma column and they deposit fuel preferentially in the hotter, denser central plasma regions, where is the highest evaporation rate of the hydrogen ice. The deep deposition of particles is beneficial and brings several advantages. Generally, it takes a longer time for a deeper delivered particle to escape from the toroidal trap by a diffusive way, simply because of the longer distance it has to go, and therefore particle confinement time increases. In pellet experiments undertaken at several toroidal devices, energy and particle confinement improvement has been observed associated also with greater thermonuclear reactivity. The pellet injection also allows us to operate at higher densities, both in L and H-mode regimes, and to better control the shape of the plasma density profile. [12][13]

5.2 *Pellet shielding and ablation*

When a pellet is injected into the tokamak plasma, it is exposed to energy fluxes carried by plasma electrons and ions and it erodes or ablates. The ablation rate is defined by the balance between the energy flux available and the flux needed to remove the particles from the pellet surface, to dissociate, ionize and accelerate them. These particles create a large cloud of cold and dense neutral gas surrounding the pellet, which can be up to *100* times larger than the pellet itself. The outer edge of the cloud interacts directly with plasma, is heated and ionized. This cloud effectively protects the pellet from direct interaction with plasma particles and thus prolongs its lifetime and increases the pellet penetration depth. There are three main mechanisms of shielding provided by the neutral and ionized gas around the pellet.

1) *Magnetic shielding:* Plasma at the outer edge of the gas cloud distorts local magnetic field, causes its partial expulsion from the cloud interior and thus reduces the incident

heat flux. The rate of shielding by this phenomenon is almost negligible in present experiments.

2) *Electrostatic shielding:* Owing to the difference in the thermal velocities of electrons and ions, the pellet surface first gains a negative excess charge. Therefore it reduces the incident electron flux and increases the ion flux, until they are equalized. During the shielding period, the net energy flux may be reduced approximately by a factor of 2.
3) *Neutral gas and/or plasma dynamic shielding:* The dense neutral gas and plasma from the cloud of ablated particles shield the surface of the pellet from direct interaction with flux of energetic plasma particles via collisions with these particles. For hydrogen pellets, this process is by far the most important. On this shielding phenomenon, the most widely used neutral gas shielding (NGS) ablation model is based.

The magnitude of these shielding effects then determines what fraction of the energy flux, carried by the tokamak plasma particles reaches the surface of the pellet and consequently the pellet ablation rate, pellet penetration depth and pellet lifetime.
As the cloud of ablated particles evolves around the pellet on a timescale of the order of 1μs or less, it is elongated and expands because of its high pressure (about *10* times higher than the surrounding plasma). The ionized part of the cloud forms a cigar shaped plasmoid, which expands along the magnetic field lines by ion acoustic velocity in plasma. It also conducts a drift motion due to inhomogeneous magnetic field. The electrons and ions are separated due to combined effect of ∇B drift and magnetic field curvature drift and thus local electric field is created, which causes $\vec{E}\times\vec{B}$ drift motion in the outward direction (in the direction opposite to magnetic field gradient, towards the so called low field side, LFS, of the vessel). This drift motion lasts for approximately $20\mu s$ until the short circuiting of charge separation by electron current along the magnetic surfaces. The ionized gas is then confined to local magnetic flux surfaces. When the pellet exits from its old magnetically confined cloud, a new cloud develops around it and the process is repeated. [12][13]

5.3 Fuelling efficiency

The expected enhancement of particle fuelling efficiency was the first motivation for injecting pellets into the tokamak plasma. The fuelling efficiency is defined as the proportion of the deposited material that remains effectively in the discharge or in the case of pellet injection as the step increase of the plasma particle content due to pellet injection divided by the number of particles in the injected pellet. The injection of a solid pellet enables placement of the fuel particles deeper into the plasma, and so from this geometrical effect alone one would expect a significant improvement in fuelling efficiency. This is indeed proven in experiments, where the fuelling efficiency of the pellet injection is relatively high. It can be in a range of *50-100%,* which is much more than maximally a few percent efficiency of the gas puffing. It has been observed, that the main parameters, which influence the pellet penetration depth and consequently also the fuelling efficiency, are the pellet size, injection velocity and also the trajectory. Performed experiments confirmed, that injection of the pellets from the magnetic high field side (HFS) leads to a more efficient fuelling and lower confinement degradation with additional power, despite a limited pellet velocity. This is due to $\vec{E}\times\vec{B}$ drift of the ablated material. The cloud of ionized ablated material is displaced against the magnetic field gradient, as was described before. This leads to deeper penetration of particles for pellets injected from the HFS compared to the pellet fuelling from the LFS.[12][13][14]

Even a pellet acceleration towards the LFS was observed, in a range of $(1\text{-}5)\cdot 10^5 m\cdot s^{-2}$, which can be explained also as the effect of $\vec{E}\times\vec{B}$ drift. Due to the $\vec{E}\times\vec{B}$ drift, a part of the shielding cloud drifts towards LFS and thus causes reduced pellet shielding at HFS compared to its LFS. Increased ablation at the HFS of pellet causes pellet rocket acceleration.[15]

The experiments have revealed that, as a result of deep pellet fuelling, not only does the efficiency increase, but on timescales long compared with the pellet ablation itself also the plasma performance improves. This improvement is thought to be caused by unusually peaked electron density profiles, which imply improved particle transport properties in pellet fuelled plasmas. The improved transport has the advantage of reduced energy loss by convection and conduction and reduced particle loss. On the other hand, a problem may occur with impurity accumulation accompanied with strong radiation cooling. Improved particle transport could also potentially create a problem with removal of the helium ash in burning plasmas. However, in reactor-grade plasmas even HFS pellets will penetrate only *~15-20%* of the minor radius, due to high plasma temperatures at the plasma edge. This motivates development of superfast pellets (*10km/s*) but this is far from practical application yet.

Apart from the energy and particle confinement improvement on longer timescales, rapid transport and enhanced energy and particle losses are sometimes observed on the timescale of the pellet ablation itself. This could be possibly attributed to markedly enhanced electron pressure and density gradients and to modified post-pellet magnetohydrodynamic (MHD) activity of the plasma, especially to so called edge localized modes (ELMs). Along with pellet mass losses during the pellet acceleration and delivery, these prompt post-pellet particle losses are the most significant factor reducing the fuelling efficiency and so they influence also the design and parameters of the pellet injection system itself (namely the particle throughput which must be provided by the pellet injector to maintain the plasma density). Therefore the aim of this work was to try to quantify this increased post-pellet transport.[12][13]

5.4 Pellet production, acceleration, injection

Pellet injection concepts share common technological problems associated with the properties of solid hydrogen. The hydrogen isotopes (H_2, D_2 and T_2) freeze in the temperature range of *14-20K*, which leads to a necessity to use liquid helium cooled components for the pellet production. Also high vacuum and low heat loss techniques must be applied and suitable materials strong enough in these low temperature conditions must be used. Moreover, the physical properties of solid hydrogen play an important role with respect to its acceleration to high velocities. The densities of the solid hydrogen are low ($0.20\text{-}0.31 g/cm^3$ for D_2 and T_2) and so the necessary acceleration forces are not very high. For example, a 6mm deuterium pellet with a mass of *35mg* can be accelerated to speeds about *1.5km/s* in acceleration path less than a metre long with a light gas gun injector operating at propellant gas pressure of *60bar*. On the other hand, the yield strength of the solid hydrogen is also low (ranging from *≈2bar* for H_2 at *8K* to *≈10bar* for T_2) and places a low limit on possible acceleration forces.

Solid hydrogen pellets may be produced generally by two methods:

1) Hydrogen gas condenses and solidifies in a small part of narrow tube and then is ejected by high pressure gas (MAST)

2) Hydrogen gas is liquefied and pushed through the extruder, where it solidifies, and then is cut mechanically. (JET).

For pellet acceleration, a variety of ways have been considered. The most important ones are given below:

1) *Centrifuge accelerators:* Pellets are constrained to move in a track on a high speed rotating disc. The radius of the accelerator is varying between tens of centimeters and the order of a metre. The performance of the centrifuge is limited by the speeds achievable by the accelerator and the ability of the pellet to withstand the forces during the acceleration process. A centrifuge injector is capable of operating at high repetition rates. The pellet velocity achievable by this way is limited by the arm and pellet strength to velocities less than *5km/s*. This is for example the way of accelerating the pellets on JET.
2) *Light gas guns:* A pellet is put into a tube and subjected to an applied pressure imbalance and is therefore accelerated. In a simple single stage light gas gun, the driving force is provided by a high pressure gas (typically < *100bar*) admitted behind the pellet by fast electromagnetic valves. Single stage gas guns operate usually with hydrogen or helium propellants at a room (or little higher) temperature. These devices, show, however, saturation in velocity at about *2km/s* due to the fact that the pellet surpasses the local sound speed. To overcome this problem, a two stage guns are developed. It is also difficult for these guns to attain high repetition rates.
3) *Electromagnetic:* Electromagnetic accelerators have been proposed to accelerate a carrier holding the pellet. The pellet will then enter the plasma and the carrier will be caught.
4) *Ablation:* A laser or electron beam incident on one side of the pellet would ablate away a part of its surface and thus accelerate the pellet by a rocket effect. This acceleration must be done gradually to avoid fracturing the pellet by shock waves.

The accelerated pellet then travels through a guide tube and is injected into the plasma. In order to access the vacuum vessel from the HFS, the guide tube needs to be curved. The curvature radius then determines the maximal possible pellet velocity (because of the stress experienced by the pellet in the curved sections). This is an issue also for ITER.[12][13]

5.5 Pellet fuelling at JET

Two pellet injectors are currently available at the JET tokamak. The older JET centrifuge injector, operational from 1995 and new HFPI (High frequency pellet injector) installed in 2008.

The centrifuge injector is capable of producing $4mm^3$ cubic pellets (containing ~ $3.8 \cdot 10^{21}$ D atoms) and delivering them into plasma at speeds $150\text{-}300 m \cdot s^{-1}$. Maximal repetition rate of the system is *10Hz*. Pellet size, velocity and repetition rate are fixed within one plasma discharge. However, repetition rate can be reduced in the discharge by omitting single pellets.

The HFPI is based upon a screw extruder technology with great pellet production rate (up to $1500mm^3/s$ and light gas gun acceleration (short pulse of Helium propellant gas ~*20bar*). It is capable of producing small pellets injected at very high repetition rate for ELM pace making and mitigation and larger pellets at still high repetition rate for deep plasma fuelling. Its operational parameters are in the Tab 5.1 below:

Pellet volume – Vol.1 – Vol.2	 Adjustable *1-2mm*^{3} Adjustable *35-70mm*^{3}
Injection frequency	*10-60Hz* for Vol.1 < *15Hz* for Vol.2
Pellet material	Hydrogen, deuterium
Pellet velocity	Adjustable $50\text{-}200 m \cdot s^{-1}$ for Vol.1 Adjustable $100\text{-}500 m \cdot s^{-1}$ for Vol.2

Table 5.1: *JET HFPI parameters [23]*

There are three injection paths on JET tokamak, each injector being equipped with a fast selector allowing to select the flight tube, by which the pellet will be injected into plasma. These are the low field side (LFS), vertical high field side (HFS) and high field side (HFS) flight tubes. LFS injection is horizontal, HFS *44*° with respect to midplane and VHFS *74*° with respect to midplane (see Fig. 5.2). [23][24]

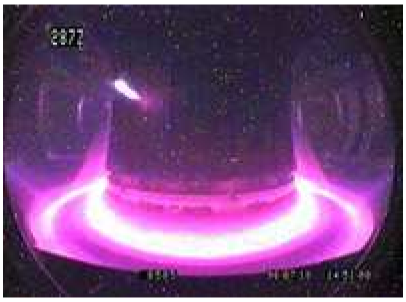

Figure 5.1: *Photograph of a pellet in flight.[10]*

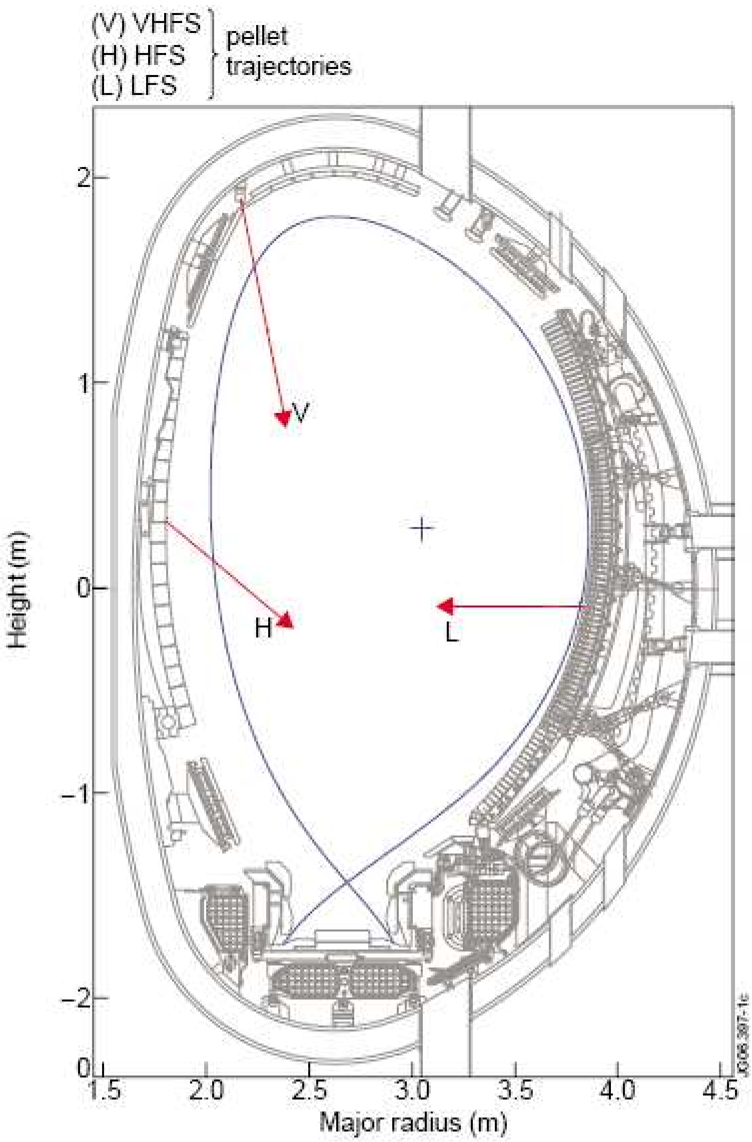

Figure 5.2: *Poloidal cross section of JET with depicted pellet injection tracks for a typical JET plasma discharge (separatrix is shown). [24]*

5.6 Pellet fuelling at ITER

Pellet fuelling from the HFS will be the primary core plasma fuelling technique on ITER. The provided core plasma fuelling is necessary for achieving high fusion gain. The proposed ITER fuelling system consists of two pellet injectors with multiple inner wall guide tubes and one guide tube for outer wall injection. The inner wall guide tubes will provide high throughput fuelling, while the outer wall guide tube is meant to trigger frequent smaller ELMs. As an edge fuelling method, set of *4* manifolds near the top of the vessel and three gas injection tubes in the area of divertor will provide gas fuelling. The gas fuelling rate will be up to $240Pa \cdot m^3 \cdot s^{-1}$, the pellet fuelling rate will be maximally $100Pa \cdot m^3 \cdot s^{-1}$ and the NBI system will provide less than $1Pa \cdot m^3 \cdot s^{-1}$. The ITER pellet injection system must be able to supply $0.23g \cdot s^{-1}$ ($\approx 1.0cm^3 \cdot s^{-1}$ solid DT) to the plasma (if the production and acceleration losses are not considered), which is significantly more than the present devices are capable to supply. In the present time, a light gas gun with continuous extruder is considered for the pellet acceleration. The technology to achieve the needed high throughput pellet fuelling is still under development, but is expected to be available within the needed ITER time scale.

The ITER pellet injection system will be limited by a guide tube curvature to a velocity of $300 m \cdot s^{-1}$ for injection from the HFS. Despite this limitation, the injection from HFS will still lead to a deeper pellet penetration due to a rapid mass drift in the major radius direction, as was discussed before. The modelling of pellet scenarios shows that injected pellets will have the capability to fuel the plasma well inside the separatrix, providing a significant level of fuelling beyond the expected ELM affected edge region. The fuelling efficiency is predicted to be nearly *100%*. It seems however, that it will not be possible to generate strongly peaked density profiles on ITER by this pellet scenario. The limited pellet velocity will lead to a pellet penetration of about *15-20%* of the minor radius. If the strong density peaking is needed, then technologies providing deeper pellet penetration will need to be developed.[16]

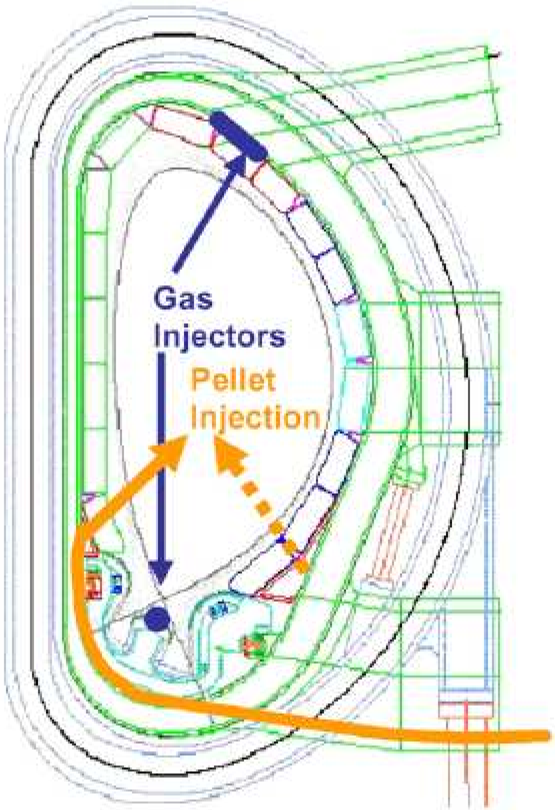

Figure 5.3: *ITER cross section showing the locations of pellet and gas injectors. The dashed pellet trajectory shows proposed LFS pellet injectors intended for ELM triggering [16].*

5.7 Other pellet functions

There are also other functions which may be performed by the injection of pellets. Recently the pellets are studied for their capability of ELM mitigation. Edge localized modes (ELMs) are MHD instabilities in the pedestal region typical for H-mode scenarios. They provide outbursts of energy and particles from the plasma in a quasi-periodic way. They are followed by a phase of pedestal pressure rebuilding. Pellets tend to trigger ELMs automatically. These

pellet induced ELMs are responsible for a significant loss of the deposited material, however, it can be used to our benefit. It has been shown, that increasing the ELM frequency by external pace making using pellet injection results in a reduced ELM energy, which is essential for the target lifetime of ITER and a future fusion reactor. For example on ITER, small pellets with a *20-40Hz* frequency injected from the LFS are supposed to be sufficient to lock the ELM frequency to pellets, thus keeping the size of ELMs much lower than they would be at a natural frequency [16][17].
Another function, which may be performed by the pellet injection system in future fusion reactors, is fast plasma termination. This function will be required in future fusion reactors, because in a case of loss of control of the plasma equilibrium at high performance, the damage caused to first wall materials could be too high. One of the possible ways for mitigation of the plasma disruption is injection of a 'killer' – pellet of medium Z impurity. The pellet radiation would then decrease the plasma thermal energy and thus limit the heat flux onto the divertor plates.

The injection of a pellet or a series of pellets is also a technique for triggering of an Internal Transport Barrier (ITB). ITB is a region of steep pressure gradient inside the plasma. Plasmas with ITB belong to so called "advanced tokamak" scenarios, which are desirable for high performance operation because they exhibit higher confinement compared to the usual H-mode [13][18].

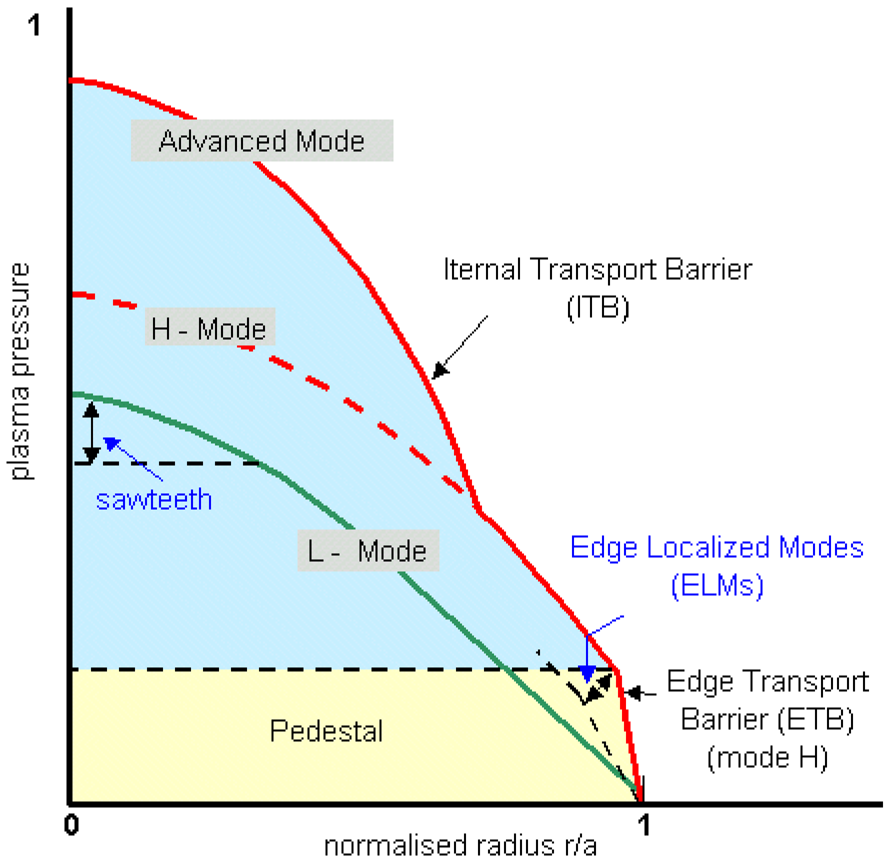

Figure 5.4: *Plasma pressure profile for L-mode, H-mode and regime with ITB [18]*

For this chapter I used information mainly from the two review papers available concerning pellets [12][13]. More information about the ITER pellet system can be found in [16].

6 Experimental settings and data

6.1 Experimental settings

In this work, data from JET pulse *#53212* have been evaluated. The basic parameters of this discharge are summarized in Tab. 6.1:

Plasma current I_p	*2.5MA*
Toroidal magnetic field B_T (on magnetic axis)	*2.4T*
Major radius R	*3m*
Minor radius a	*1m*
Elongation κ	*1.7*
Edge safety factor q_{95}	*3.2*
Plasma volume V_p	$80m^3$
Additional plasma heating P_i	*17MW NBI, 1MW ICRH*

Table 6.1: *Summary of the basic plasma parameters of JET pulse #53212*

This pulse was a part of experiments undertaken at JET aimed to develop optimized pellet refuelling scenarios (in 2001). Pellet injection sequences were optimized for long pulse fuelling to high densities, while maintaining the H-mode and good energy confinement and keeping the impurity level low. These experiments also tried to combine positive effects of deep pellet refuelling and high plasma triangularity. The pellets were injected by the JET centrifuge injector and their parameters are in the Tab. 6.2 below.

Pellet size	$4mm^3$, $3 \cdot 10^{21}$ atoms
Composition	deuterium
Repetition rate	*3Hz, 6Hz*
Injection speed	$160 m \cdot s^{-1}$
Injection path	from HFS along a trajectory tilted by *44°* to the horizontal plane. (see Fig. 4.2)

Table 6.2: *Summary of the basic pellet parameters for JET pulse #53212.*

For this pulse, there were three sequences of pellets injected into the plasma column: sequence of five, six and seven pellets. The first sequence starts at time $t = 57.87s$, pellets injected at a preset repetition rate of approximately *6Hz*. Then two single pellets are omitted and the next sequence of six pellets is injected at time $t = 58.98s$ at halved repetition rate of approximately *3Hz*. Then three single pellets are omitted before the last pellet injection sequence starts at $t = 61.22s$ also with reduced repetition rate of approximately *3Hz*.

6.2 Plasma diagnostics

The following data for JET shot *#53212* were downloaded from the JET database and considered in this work:

- Temporal evolution of line averaged electron density measured by interferometers along *8* different lines (see figure 6.1).
- Temporal evolution of electron density profile measured by LIDAR (see Fig. 6.1).
- Temporal evolution of electron temperature profile measured by LIDAR.
- Temporal evolution of D_α emission measured by visible spectroscopy.
- Temporal evolution of total plasma energy content W_{tot} measured by two diamagnetic coils.

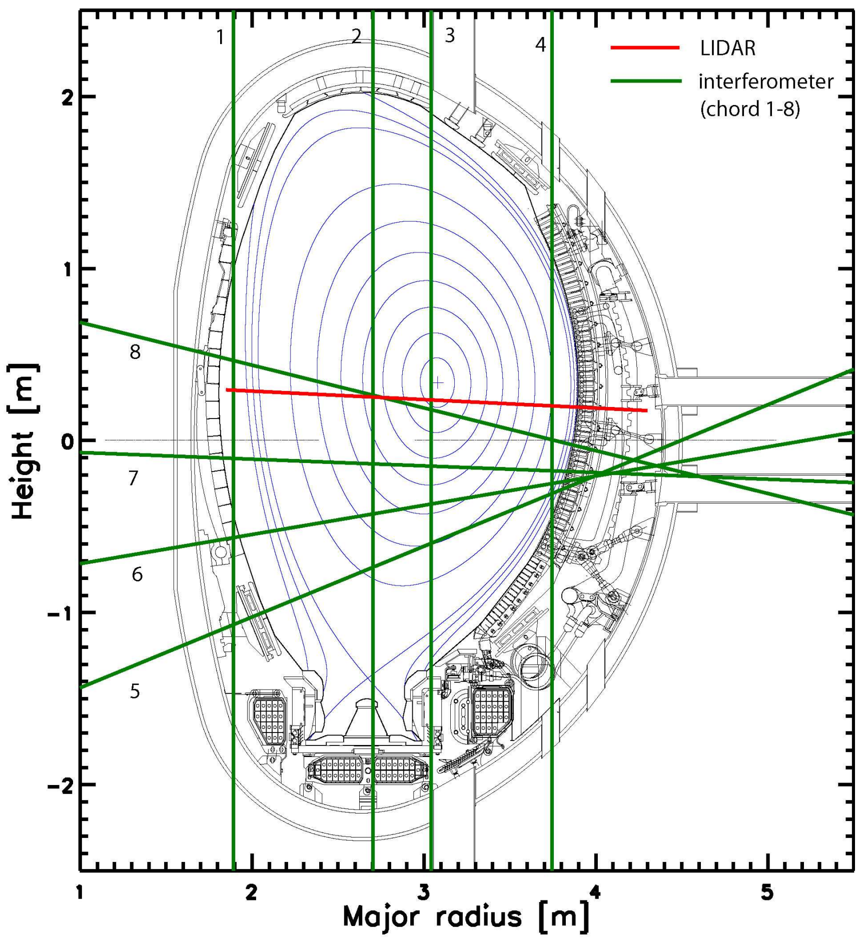

Figure 6.1: *JET tokamak poloidal cross section with shown trajectories of LIDAR (red) and 8 chords of interferometer (green). Blue lines show the magnetic surfaces for the considered shot #53212.*

LIDAR (LIght Detection And Ranging)

LIDAR diagnostics measures plasma electron temperature and density. It uses a laser pulse projected into the plasma. The laser light is scattered via Thomson scattering process, which is an elastic scattering of electromagnetic radiation by a charged particle. The incident wave accelerates the charged particle due to its electric field component. The particle moves in the direction of the oscillating electric field of the wave and emits electromagnetic dipole radiation. The monochromatic laser light is scattered and Doppler shifted by the fast moving plasma electrons (for ions, the scattering is usually neglected due to large ion mass), producing a broad spectrum of scattered light. By measuring the width of this scattered spectrum the velocity distribution and hence the electron temperature T_e can be determined and by measuring the total intensity of the scattered light the density of the electrons n_e can be deduced. In order to get the spatial resolution of these quantities, a very short laser pulse is sent into plasma (*0.3ns* which is *~10cm* long) and a fast detection and recording system is used to observe the time evolution of the back-scattered spectrum. From this time dependence and the LIDAR principle the local values of electron temperature and density can be deduced. A *1J* ruby laser (wavelength *694nm*) is used at JET as the light source, with a frequency of *4Hz*. The trajectory of the pulse can be seen at Fig. 6.1.[10][29]

Interferometry

The idea of this diagnostics is to superpose two or more waves travelling along a different path and observe their phase shift. Typically a single incoming beam of laser light is split into two identical beams by a partial mirror. One of the beams passes through the plasma. These two beams are then made to interfere. The path difference and the change of refractive index in the path of the beam crossing the plasma create a phase difference between them and an integrated electron density along the path of the beam can be deduced. *8* different paths are used at JET (see Fig. 6.1).

The D_α emission measured is the light of a wavelength *656nm* emitted by a deuterium atom during an electron transition from the third to the second energy level. When the plasma gets in contact with the walls, neutral hydrogen particles (previously deposited on the wall) are knocked out. They interact with the edge plasma, are excited and emit line radiation. One of the lines is D_α.

6.3 Plasma response to the pellet

The main intention of the series of pellet experiments at JET including pulse *#53212* was to access densities in the vicinity of *Greenwald density* n_e^{Gw} (Greenwald density is an experimentally determined limit of plasma density), while keeping the confined energy high. During these experiments several critical issues appeared:

- Excessive increase of the plasma edge density
- Trigger of central MHD activity
- ELM bursts following pellet injection

Each of these effects connected with pellet injection can cause severe energy losses and therefore attempts were made to minimize them.

The excessive increase of the edge density could be limited by lowering the maximum pellet injection rate to *6Hz*. The pellet induced increase of neutral gas pressure then did not reach such high values to be able to deteriorate the confinement. The MHD activity, namely so-called neoclassical tearing mode (NTM), triggered by temperature reduction due to pellet, could be avoided by increasing the external plasma heating. Confinement losses caused by enhanced ELM activity were reduced by adapting the pellet injection cycle. Omitting single pellets leads to reduction of ELM activity and consequently to recovery of the plasma energy content.

As you can see on Fig. 6.2, the averaged electron density strongly increases for a short time after each pellet injection, reaches its maximum and then drops down again, until the next pellet is injected. The first short phase of strong density increase describes the pellet evaporation. The outer atoms of the pellet ablate in the hot plasma and are ionized. The moment of total pellet evaporation can be seen on Fig. 6.2 as the time of local maximum of electron density. The prompt post pellet particle losses can be explained by transiently increased plasma radial diffusivity because of increased density gradient. Also pellet induced ELMs may carry out immediately a very large fraction of the pellet delivered particles.

The frozen pellets injected into the plasma column accordingly decrease the plasma temperature. This decrease is proportional to density increase and product of plasma density and temperature (plasma pressure) remains approximately the same during the pellet injection. Injection of each pellet also results in quick energy loss, mainly due to a triggered ELM. However, in phases between the injected pellets and especially in longer periods between two pellet sequences, the energy manages to recover.

Evolutions of essential plasma parameters for the described JET pulse are shown on Fig. 6.2. We can clearly observe that initial quick *6Hz* pellet sequence caused significant energy drop due to enhanced ELM activity (which can be identified from increased intensity of D_α emission). To allow the energy to recover, two pellets were omitted before the onset of second pellet injection. The first pellet sequence including the following pause transformed plasma to a higher density state and was able to maintain the energy content still high. The second pellet sequence at halved repetition rate of *3Hz* was able to achieve even better refuelling performance. This could be caused by the fact, that colder and denser plasmas are more suitable for deep particle deposition. The low injection rate also enabled the energy, which transiently dropped after each injected pellet, to be almost fully recovered before injection of the next pellet. Therefore the plasma density was able to surpass the Greenwald level with about *6.1MJ* energy content. Finally, this high performance phase was terminated by a growing NTM. The next pellet sequence then starts from a low density level with low confined energy and is not able to achieve the previous high confinement level. [25]

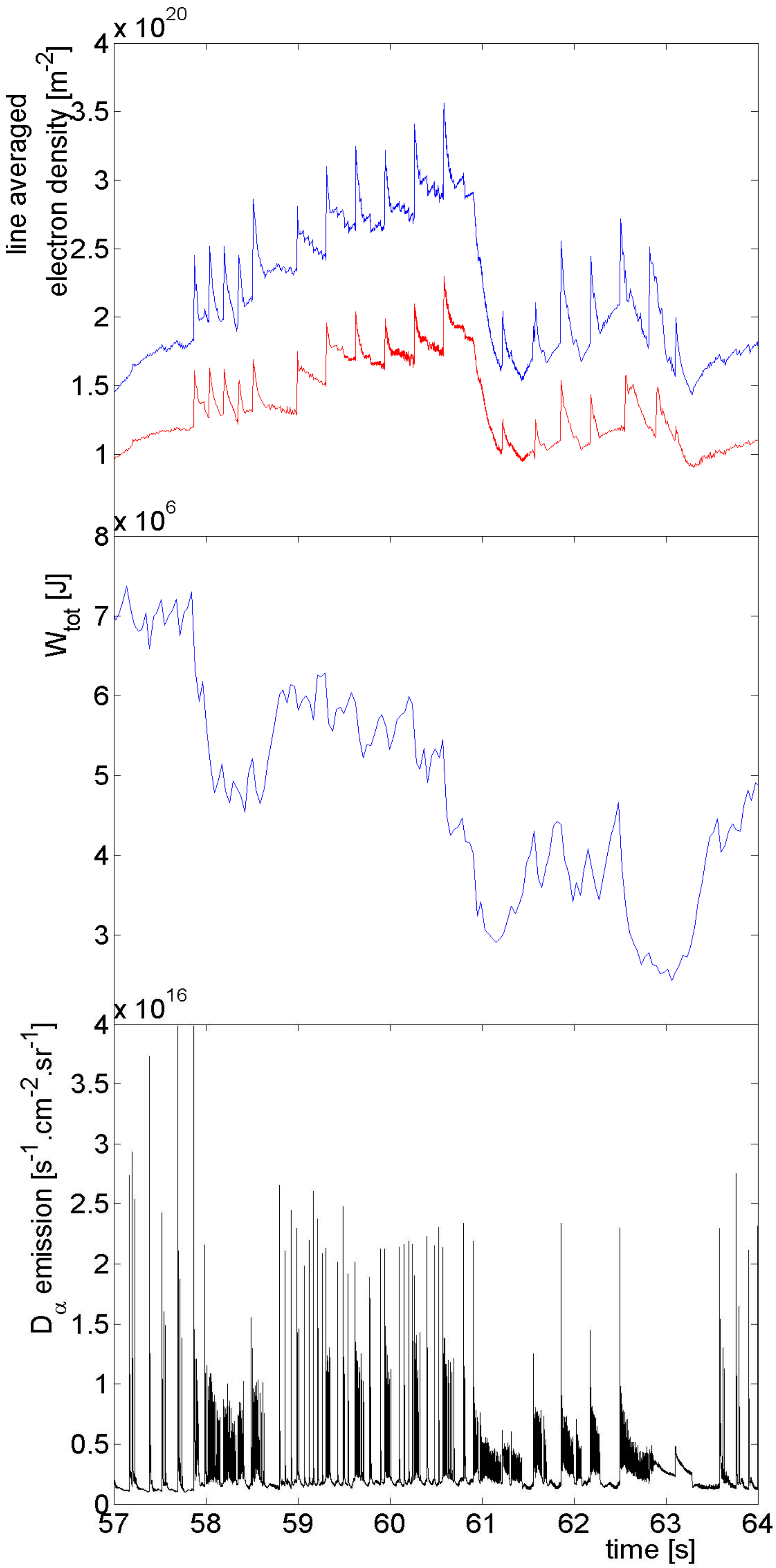

Figure 6.2: *Time evolution of line averaged electron density (chord 3 (blue) and chord 8(red)), total plasma energy and D_α emission intensity during the pellet injection.*

7 Data processing

7.1 Boxcar method

The plasma diffusivity can be estimated from the evolution of the density profile after the pellet injection. For this purpose, the downloaded data from LIDAR (electron density profiles) were used. The aim of this work was to try to quantify the transiently increased outward diffusion at the edge of plasma after the injection of a pellet. As can be seen from Fig. 6.2, the length of the pellet evaporation process is about *10ms* and the consequent phase of increased particle losses is also of the order of tens of milliseconds. Unfortunately, LIDAR diagnostics measures the density profiles with a frequency of *4Hz*, which means it is not capable to record fast changes in the electron density profile due to pellet injection. There are one or maximally two LIDAR measurements during the evaporation of the pellet and the consequent fast particle losses, which is not sufficient for calculations of the diffusion coefficient. Interferometers, on the other hand, measure electron density with a relatively high repetition rate of approximately *133Hz*. However, these densities are line averaged and thus does not provide the needed information about the density profile. One way how to get a more detailed picture of the time evolution of electron density profile after injection of a pellet is to make a *boxcar analysis* of the LIDAR data. The idea of the boxcar analysis is following:

- In this method, every injected pellet is assumed to be the same and its injection is assumed to have always the same impact on electron density profile evolution.
- The LIDAR measurement comes for every post-pellet density evolution in a different time. For each LIDAR measurement, its relative time to the moment of injection of the last pellet is calculated.
- These measurements with assigned relative times are then put together and an “average post-pellet electron density profile evolution” is gained.

For the calculations performed in this thesis, the boxcar analysis of the first and third pellet sequence from the JET pulse *#53212* (starting at times $t = 57.87s$ and $t = 61.22s$) was done. The post-pellet line averaged electron density evolution is approximately equally shaped for these sequences and the pellets are injected in approximately equally dense plasma (see Fig. 6.2). The procedure of assigning the relative times to the LIDAR measurements can be seen on the following Fig. 7.1 and 7.2. On these figures the top red graph shows the density evolution measured by LIDAR for $R = 3.6m$ (major radius), the bottom graphs show line averaged electron density measured by *8* chords of interferometer. The point of intersection of the black vertical lines (in the times of LIDAR measurement) with the interferometer data shows us, in which part of the pellet-induced density evolution the LIDAR measurement is located. From the downloaded interferometer data it is possible to determine the pellet injection times (which correspond to the places with sudden strong increase of density) and with the aid of Fig. 7.1 and 7.2 it is then possible to assign relative times to each LIDAR density profile measurement. Therefore the “average” post-pellet temporal evolution of electron density profile is gained.

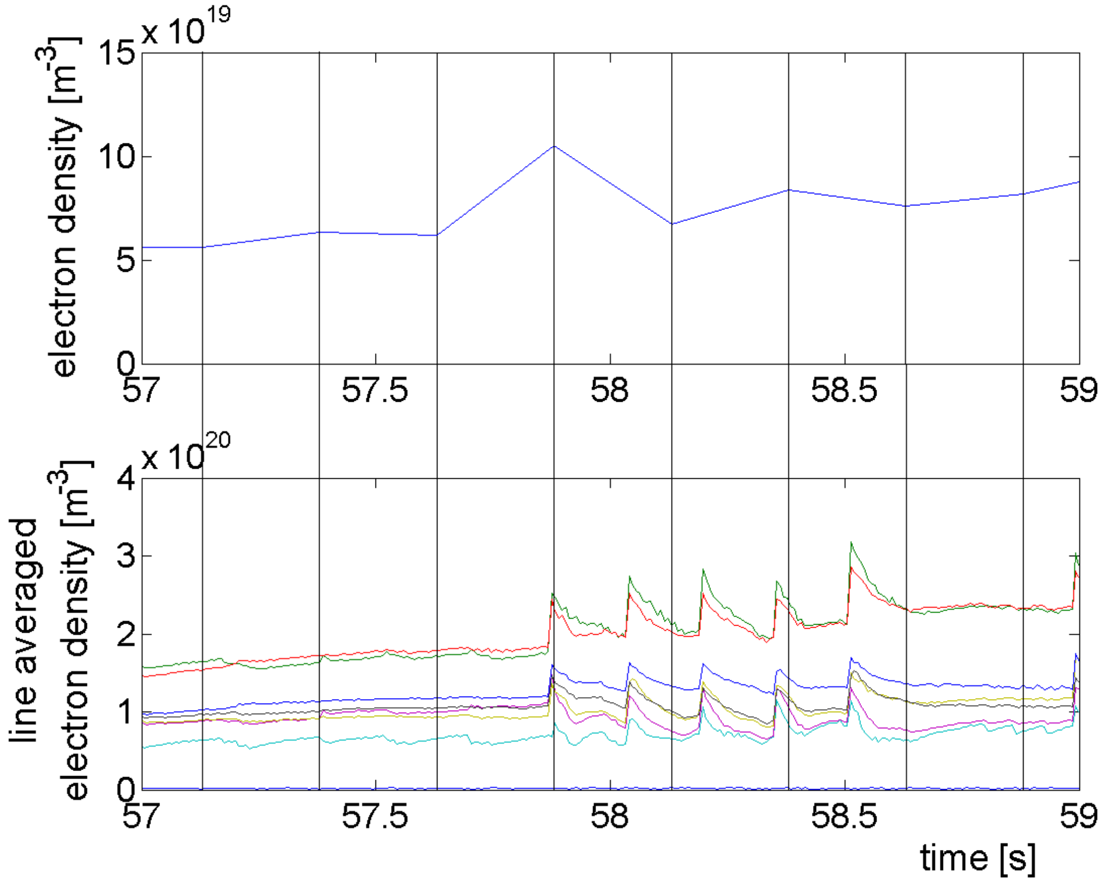

Figure 7.1: *The boxcar analysis of the first sequence of pellets starting at t = 57.87s*

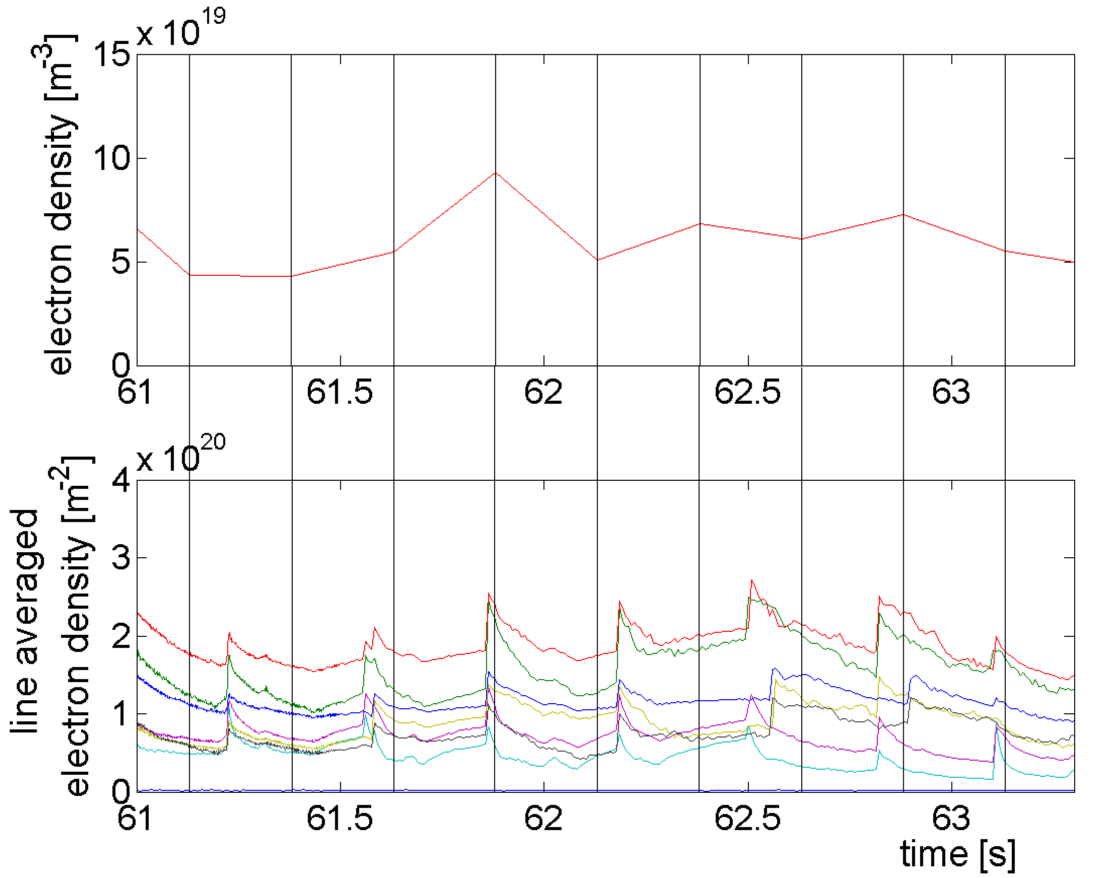

Figure 7.2: *The boxcar analysis of the third sequence of pellets starting at t = 61.22s*

From the analysis, only *4* most reliable post-pellet electron density profiles were chosen (profiles after pellets *1*, *2* and *4* from the first sequence and one profile after pellet *3* from the third sequence) along with three pre-pellet profiles before the first sequence of pellets. Graph containing these profiles and a graph of the gained average post-pellet density evolution at two different outer edge plasma radii are shown below for illustration (Fig. 7.3 and 7.4).

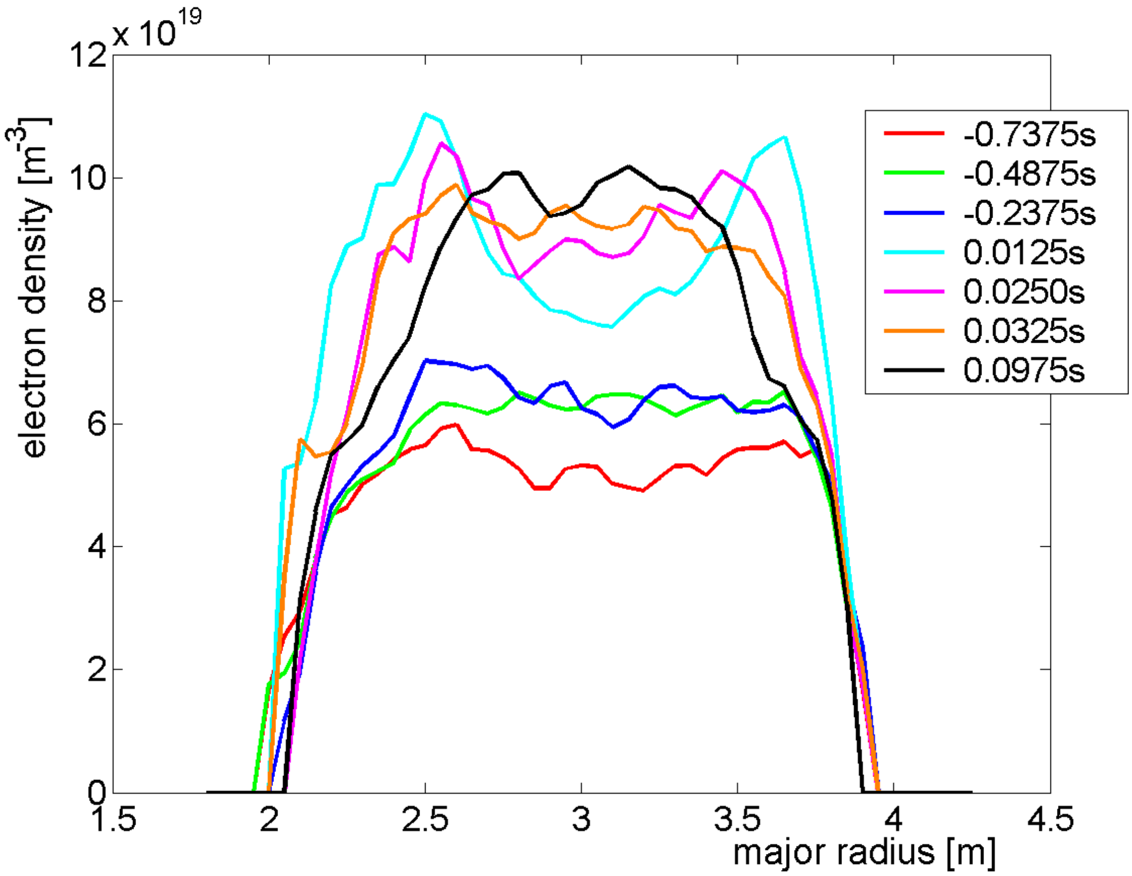

Figure 7.3: *Electron density profiles from the boxcar analysis with a legend of their relative times.*

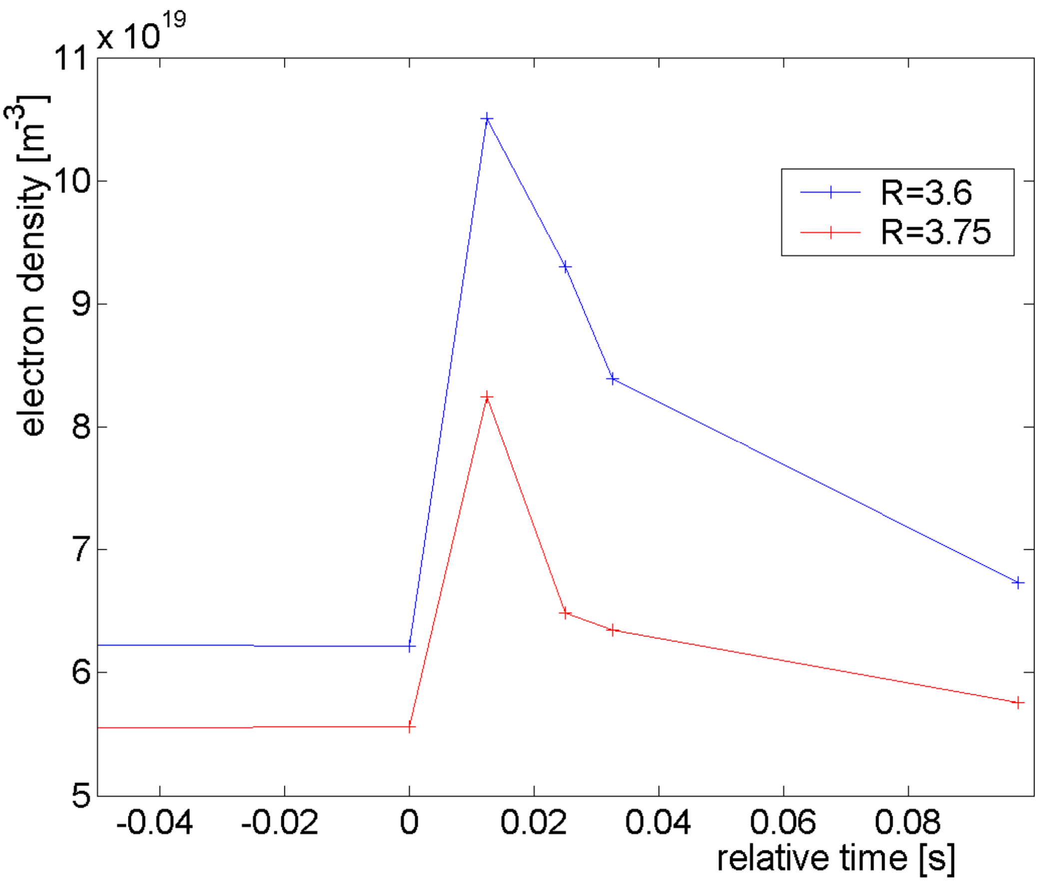

Figure 7.4: *Dependence of the post-pellet electron density on relative time to the injection of pellet (gained from the boxcar analysis) for two values of major radius 3.6m and 3.7m.*

However, the boxcar method is an approximate method facing many problems and there are more possible error sources. The pellets' mass and shape can slightly differ after the production. Also during the injection and pellet flight through the guide tube, the pellet mass losses occur, which are different for each pellet. These losses may be up to about *10%* of the total pellet mass. The major error may arise from the fact that electron density profiles in different injection times differ. For the boxcar analysis performed in this thesis, the error in electron density caused by this effect may be roughly estimated from the interferometer data as *~10%*. The computations based on the data processed by the boxcar analysis thus provide rather qualitative than exact quantitative estimates of plasma parameters. Nonetheless, with respect to the mentioned error estimates, these computations can still be meaningful and provide useful information.

The problem with insufficiently time-resolved information about the electron density profile can be solved also by inverse integral transform of the interferometry data. The problem of deducing spatial resolution of some function, when data about its integrated values along different trajectories are given, is in fact an issue of tomography. At the JET tokamak, these methods are applied to combine the LIDAR spatial and interferometer temporal information about the plasma electron density [30]. This is, however, beyond the scope of this work.

8 Calculations

8.1 Bessel functions analysis

In the following text, the subscript denoting the particle species is omitted because all the computations are performed for plasma electrons. The computed edge plasma diffusion coefficient is, however, valid both for electrons and ions as the diffusion is expected ambipolar.

For the calculation of the diffusion coefficient itself, a simplified version of diffusion equation (4.7) can be used. In real experiments, it is very difficult to distinguish between particle diffusion and convection. Therefore so-called effective diffusion coefficient, which describes both these phenomena, can be introduced and it is defined as:

$$\vec{\Gamma} = -D_{eff} \cdot \vec{\nabla} n\,, \tag{8.1}$$

and the equation (4.7) can be written as:

$$\frac{\partial n}{\partial t} = div\left(D_{eff}\vec{\nabla} n\right) + S \tag{8.2}$$

In the following text, D will always denote the effective diffusion coefficient D_{eff}. Calculation of S is also very difficult. It can be expressed as:

$$S = div\vec{\Gamma}_{ionisation}\,, \tag{8.3}$$

where $\vec{\Gamma}_{ionisation}$ is the particle flux caused by the source S of particles due to ionisation or recombination. The equation (8.2) can then be written as:

$$\frac{\partial n}{\partial t} = div\left(D\vec{\nabla} n + \vec{\Gamma}_{ionisation}\right) \tag{8.4}$$

According to [28], $\frac{\Gamma_{ionisation}}{n} \approx 0.5 m \cdot s^{-1}$ for *r/a = 0.8*. This value is approximately ten times lower than $D \cdot \frac{\nabla n}{n}$ and as a result we can neglect the contribution of S compared to the diffusion and convection terms. The resulting simplified equation can be written as:

$$\frac{\partial n}{\partial t} - D\Delta n = 0\,. \tag{8.5}$$

The simplified diffusion equation (8.5) is a parabolic partial differential equation, which is very important in the mathematical physics. Generally, an equation of this particular shape is called the heat equation, as the same equation is used to describe a distribution of heat in a given region over time. The general form of the heat equation in n-dimensional Euclidean space E^{n+1} is following:

$$\frac{\partial n}{\partial t} - a\sum_{k=1}^{n}\frac{\partial^2 n}{\partial x_k^2} = f(\vec{x},t), \tag{8.6}$$

where *a* is a constant, $f(\vec{x},t)$ is the source term and $n(\vec{x},t)$ is the mass density. This equation (8.6) together with an initial condition:

$$n(\vec{x},0) = \alpha(\vec{x}) \tag{8.7}$$

is called *the classical Cauchy problem for the heat equation*. It can be generally solved by transforming it to a *generalized Cauchy problem for the heat equation:*

$$\frac{\partial n}{\partial t} - a\sum_{k=1}^{n}\frac{\partial^2 n}{\partial x_k^2} = \theta(t)f(\vec{x},t) + \delta(t)\alpha(\vec{x}), \tag{8.8}$$

where $\Theta(t)$ is the Heaviside step function of time and $\delta(t)$ is the Dirac delta function of time. Another step is finding the fundamental solution $\varepsilon(\vec{x},t)$ for the heat conduction operator *L*:

$$L = \frac{\partial}{\partial t} - a\cdot\Delta \tag{8.9}$$

in a space E^{n+1}. The general solution of the classical Cauchy problem for the heat equation is then determined by a convolution of the fundamental solution $\varepsilon(\vec{x},t)$ and the right side of the generalized equation (8.8):

$$n(\vec{x},t) = \int_0^t \int_{R^n} \frac{f(\vec{\xi},t)}{\left(2\sqrt{\pi a(t-\tau)}\right)^n} e^{-\frac{\|\vec{x}-\vec{\xi}\|^2}{4a(t-\tau)}} d\vec{\xi}\, d\tau + \int_{R^n} \frac{\alpha(\vec{\xi})}{\left(2\sqrt{\pi a t}\right)^n} e^{-\frac{\|\vec{x}-\vec{\xi}\|^2}{4at}} d\vec{\xi}\,. \tag{8.10}$$

This equality (8.10) is sometimes called *the Poisson formula*.[31][32]

In our particular case, the diffusion equation is homogenous, without the source term $f(\vec{x},t)$, and the constant *a* is equal to the diffusion coefficient *D*. The initial condition (8.7) is the density profile just after the pellet injection into the plasma, at the beginning of the decay process of pellet induced perturbation. The form of the general solution (8.10) is then reduced to the second term only (the first integral being zero because of the lack of the source term *f*). This form of the solution of our diffusion equation is however still rather difficult. For the further described analysis, solution of the simplified form of the diffusion equation in axial symmetry was used.

According to [33], a Bessel functions analysis was used in this work to estimate the post pellet diffusion coefficient. If we assume only a radial dependence of plasma electron density $n = n(r,t)$, the simplified diffusion equation (8.5) in cylindrical geometry can be written as:

$$\frac{\partial n}{\partial t} = D\left(\frac{\partial^2 n}{\partial r^2} + \frac{1}{r}\frac{\partial n}{\partial r}\right). \tag{8.11}$$

This equation, along with a general initial condition (8.7) and with boundaries $0 \le r \le L$ has a general solution of a form [34]:

$$n(r,t) = \int_0^L \alpha(\xi) G(r,\xi,t) d\xi , \tag{8.12}$$

where $G(r,\xi,t)$ is the Green's function. If a boundary condition $n = 0$ for $r = L$ is prescribed, then the Green's function G can be written with use of Bessel functions as:

$$G(r,\xi,t) = \sum_{n=1}^{\infty} \frac{2\xi}{L^2 J_1^2(\mu_n)} J_0\left(\mu_n \frac{r}{L}\right) J_0\left(\mu_n \frac{\xi}{L}\right) \exp\left(-\frac{D\mu_n^2 t}{L^2}\right), \tag{8.13}$$

where J_0 and J_1 are the first order Bessel functions, defined as [8]:

$$J_m(x) = \sum_{k=0}^{\infty} \frac{(-1)^k}{k!(k+m)!} \left(\frac{x}{2}\right)^{2k+m} , \tag{8.14}$$

and μ_n is the n-th positive zero of the Bessel function J_0 (which means $J_0(\mu_n) = 0$).

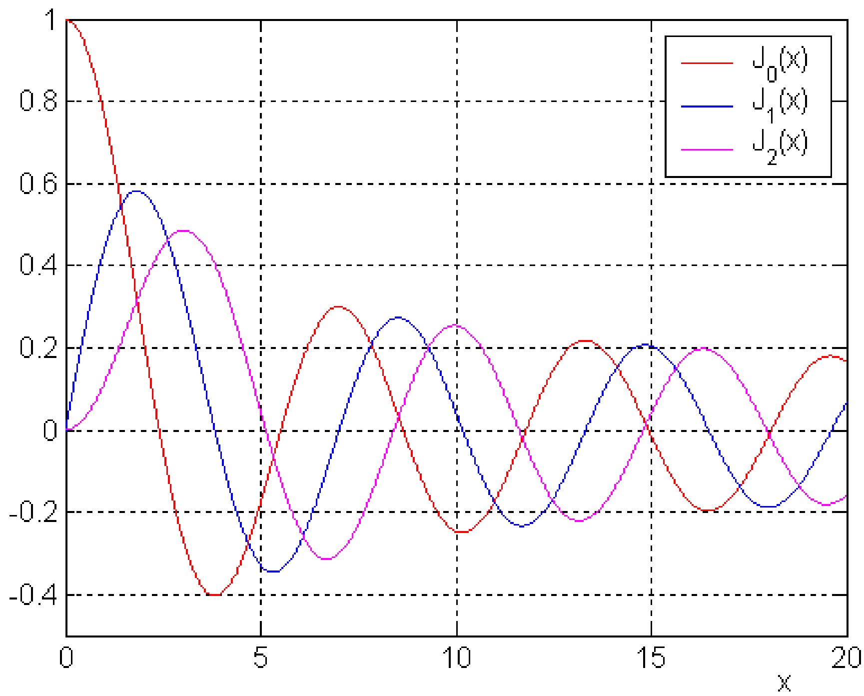

Figure 8.1: *The first three first order Bessel functions J_m.*

The data used for calculation were the three post pellet density profiles in relative times (to the time of pellet injection), which come out from the boxcar analysis in previous chapter (see Fig. 7.3). It is possible to estimate the diffusion coefficient D from the evolution of post pellet density perturbation $\delta n(R,t)$:

$$\delta n(R,t) = n(R,t) - n(R,0), \tag{8.15}$$

where R is the major radius and $n(R,0)$ is the density profile before the pellet injection. For $n(R,0)$, the electron density profile at relative time *-0.2375s* from the boxcar analysis is used (see Fig. 7.3).

To justify the use of axial symmetric diffusion equation, the three post pellet density perturbation profiles were averaged with respect to the tokamak minor (plasma) axis at $R \approx 3m$. Then these averaged profiles $\delta n(r,t)$ (for $0 \le r \le a$) were mapped on a 1-dimensional x grid varying between *0* and *1*. $\delta n(x,t)$ in a new variable x was then fitted for each time t with a fourth degree polynomial $\delta\hat{n}(x,t)$ to regularize the profile [33]. Then if $\delta\hat{n}(x,t)$ is the initial condition at time t, with use of equations (8.12), (8.13) a solution at time $t+\delta t$ may be written as:

$$\delta\tilde{n}(x,t+\delta t) = 2\sum_{n=1}^{\infty}\frac{J_0(\mu_n x)}{J_1^2(\mu_n)}\exp\left(-D\mu_n^2\delta t\right)\int_0^1 J_0(\mu_n x)\delta\hat{n}(x,t)xdx\,. \qquad (8.16)$$

The terms of the series on the right side of equation (8.16) fall down to smaller and smaller values with increasing n, therefore it is possible to cut off the series. A minimization is then applied with respect to D of the term:

$$\sum_{i=1}^{N}\left(\delta\tilde{n}(x_i,t+\delta t)-\delta\hat{n}(x_i,t+\delta t)\right)^2 = \left\|\delta\tilde{n}(x,t+\delta t)-\delta\hat{n}(x,t+\delta t)\right\|^2, \qquad (8.17)$$

where $\delta\tilde{n}(x,t+\delta t)$ is a function of D and is calculated from (8.16) and $\delta\hat{n}(x,t+\delta t)$ is the fourth degree polynomial fit of the density perturbation in time $t+\delta t$. The fitting was done by using MATLAB 6.5 curve fitting tool.

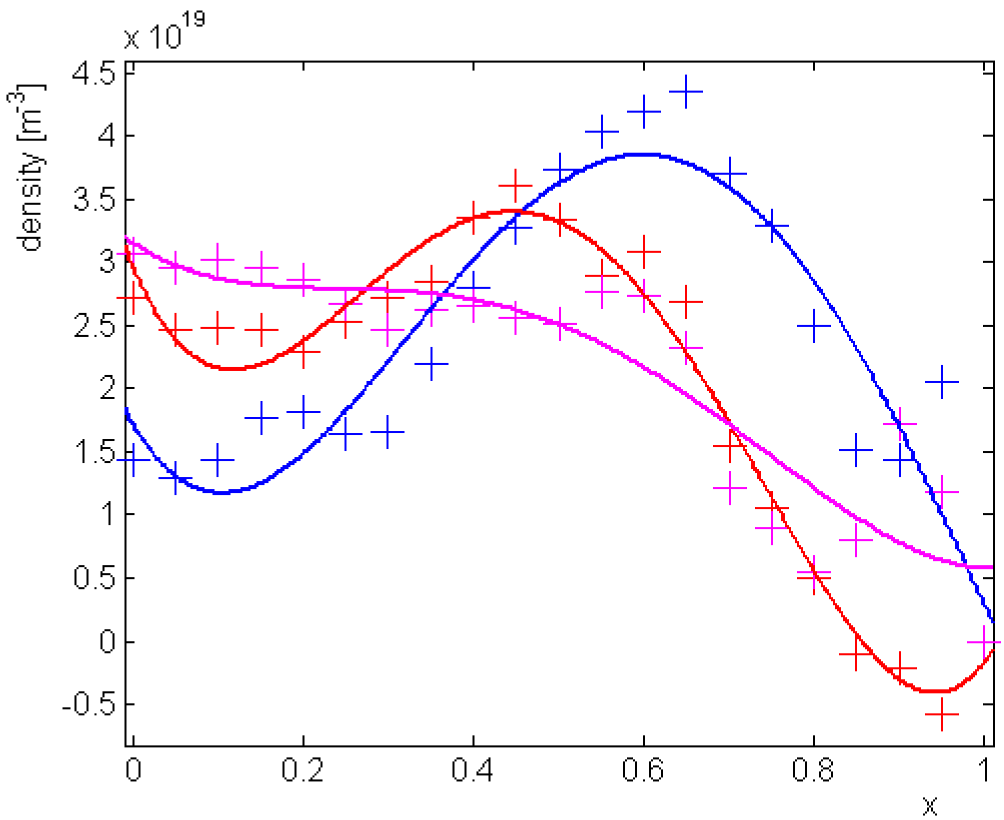

Figure 8.2: *The density perturbations* $\delta n(x,t)$ *plotted in times t=12.5ms (blue), t=25ms (red) and t=32.5ms (magenta) in the new x coordinate (+ points) and their appropriate fourth degree polynomial fits in the same times (solid lines).*

The fitted fourth degree polynomial $\delta\hat{n}(x,t)$ can be written in the following form:

$$\delta\hat{n}(x,t) = p_1 x^4 + p_2 x^3 + p_3 x^2 + p_4 x + p_5, \tag{8.18}$$

with constant coefficients $p_1 - p_5$. The results of the fitting are given in the Tab. 8.1 below (fitted values are given with 95% confidence bounds):

Time [ms]	p_1 $[10^{20}]$	p_2 $[10^{20}]$	p_3 $[10^{20}]$	p_4 $[10^{20}]$	p_5 $[10^{20}]$
12.5	3.57 ± 3.96	-9.47 ± 7.99	6.90 ± 5.26	-1.15 ± 1.25	0.17 ± 0.09
25	8.07 ± 1.99	-16.19 ± 4.02	9.40 ± 2.64	-1.59 ± 0.63	0.30 ± 0.04
32.5	1.89 ± 3.80	-3.74 ± 7.66	2.05 ± 5.04	-0.46 ± 1.19	0.32 ± 0.08

Table 8.1: *Results of the fourth degree polynomial fit of the density perturbation* $\delta n(x,t)$ *in times t=12.5ms, t=25ms and t=32.5ms.*

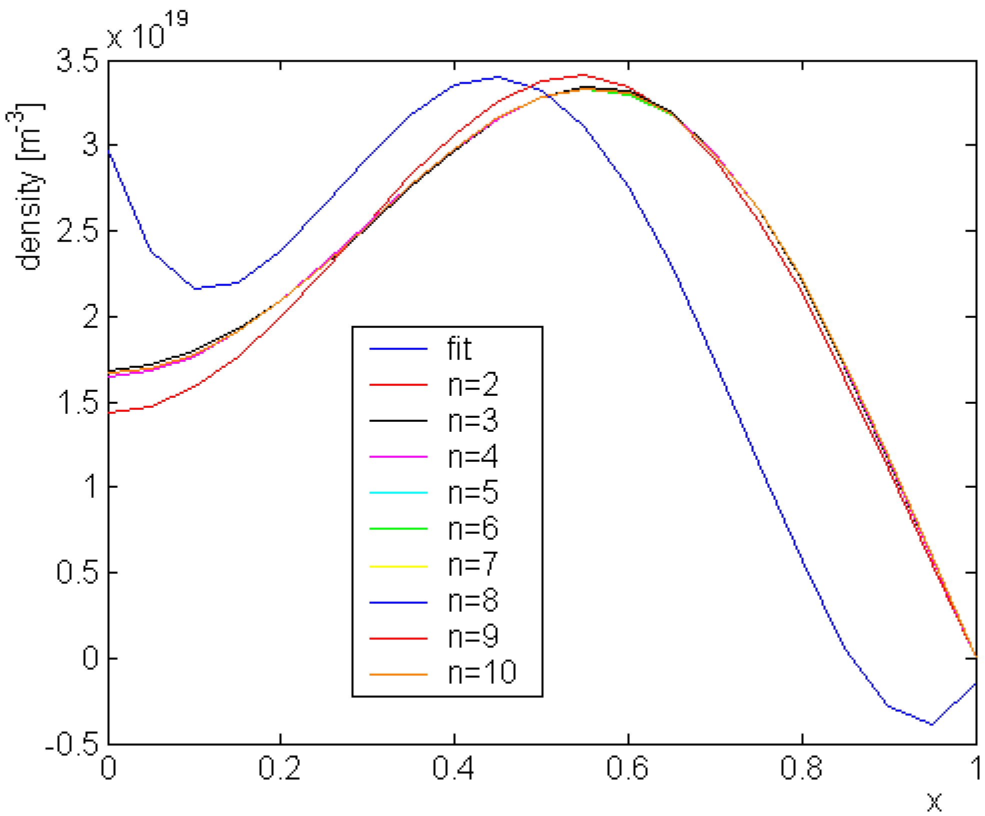

Figure 8.3: *The results* $\delta\tilde{n}(x,t+\delta t)$ *of summation (7.16) for different considered number n of the series for times t=12.5ms and t+*δt*=25ms and with use of an expected value of D=1m*^{2}*s*$^{-1}$*. The fourth degree fit of the density perturbation* $\delta\hat{n}(x,t+\delta t)$ *in time t+*δt*=25ms is given to compare (blue).*

On Fig. 8.3 are given the results $\delta\tilde{n}(x,t+\delta t)$ of summation (8.16) for different considered number *n* of the summed terms for times *t=12.5ms* and *t+δt=25ms* and with use of an expected value of $D=1m^2s^{-1}$. It can be seen, that there is not an observable difference between functions, which come up from the series in (8.16) cut off at $n \geq 3$. For this particular calculation, the series was cut off for n > *10*. This can be defended by the fact that for values of *D* not too near to zero the contribution of the last term in the sum was reduced to less than *1%* (more precisely the value of maximum difference between the functions, which come up from the series cut off at *n=11* and *n=10*, was reduced to less than *1%* of the average value of the function for *n=10*). The minimization process was then performed, for $0 < D \leq 10\ m^2s^{-1}$. The results of the Bessel functions analysis are given in Tab. 8.2 below:

Time window	$D\ [m^2s^{-1}]$
12.5 ms - 25 ms	3.295
25 ms – 32.5 ms	2.872

Table 8.2: *Diffusion coefficients calculated by the Bessel functions analysis*

The computed post-pellet diffusion coefficients in Tab. 8.2 seem rather big compared to calculations in the previous bachelor thesis [1] and similar studies on the MAST tokamak [27][33]. This may be caused by several reasons. The major problem of the analysis is the use of cylindrical coordinates and therefore the assumption of circular plasma shape. This is not true, as can be seen from Fig. 6.1 with depicted magnetic surfaces. The plasma centre is shifted in the major radius direction and the plasma has an elongated triangular D shape.

8.2 Mapping of LIDAR data to magnetic surfaces

The total plasma pressure including the energy of plasma rotation is constant on magnetic surfaces. It can be deduced from the Grad-Shafranov equation (3.21) valid in MHD equilibrium. Due to the large parallel thermal conductivities along the magnetic field lines, the electron and ion temperatures are also constant along the magnetic surfaces. The plasma pressure can be calculated as:

$$p = n_e k_B T_e + n_i k_B T_i \approx n_e k_B (T_e + T_i), \tag{8.19}$$

where T_e and T_i is the electron and ion temperature and k_B the Boltzmann constant. This means that also the electron density is approximately constant on magnetic surfaces $n = n(\psi)$. Therefore it is convenient to introduce the flux coordinates (ρ, θ, ϕ), where ρ is the square root of the normalized poloidal flux, defined by (4.23). θ and ϕ coordinates are the poloidal and toroidal angles. Their closer definition is not necessary, as the plasma density $n = n(\rho)$ is assumed to be the function of the magnetic flux coordinate only.

With use of the EFIT code mentioned in chapter 3, the matrix of $\psi(R,z,t)$ values for a grid *65x65* in spatial (R,z) coordinates (*R* is major radius, *z* height over the midplane, see Fig. 3.1) and for *130* time slices for the JET shot *#53212* was downloaded. The LIDAR electron density was then mapped on the magnetic surfaces $\rho = \sqrt{\psi}$. This was done via 2D spatial spline interpolation of $\rho(R,z,t)$ in the points of LIDAR measurement $\rho(R_{LIDAR}, z_{LIDAR}, t)$; interpolation in the times of LIDAR measurement was performed consequently. Thus values $n(\rho,t)$ of the electron density on magnetic surfaces ρ were obtained. With use of the boxcar analysis, post-pellet electron density profile evolution $n(\rho,t_{rel})$ was obtained. The smoothing spline function was then used to smooth the $n(\rho,t_{rel})$ function in ρ. Two $n(\rho)$ profiles (with relative times *-0.2375s* and *0.0125s*) before and after spline smoothing are shown on Fig. 8.4.

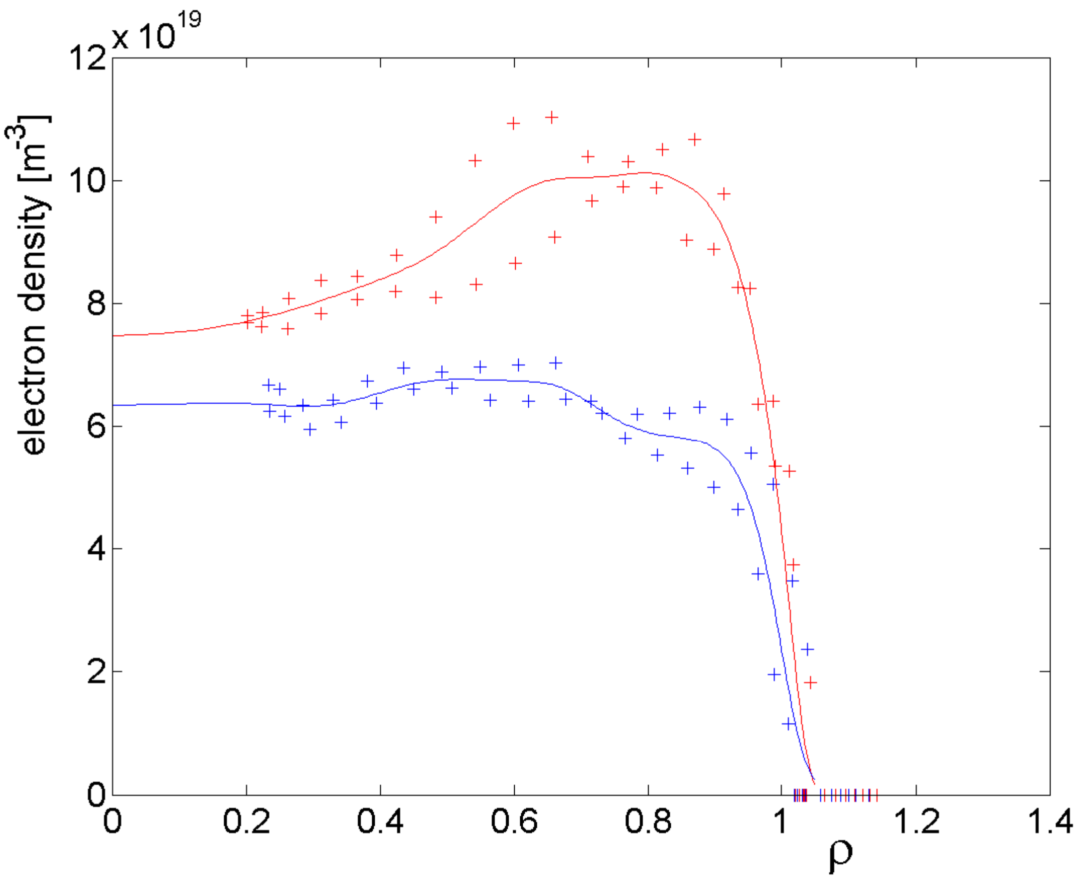

Figure 8.4: *Electron density profiles at relative times* $t_{rel} = -0.2375s$ *(blue) and* $t_{rel} = 0.0125s$ *(red) (before and after the first pellet injection at time t=57.87s). The '+' points denote the profiles before smoothing and solid lines show the smoothed dependence.*

In order to be able to calculate the temporal derivative of $n(\rho,t_{rel})$, its spline interpolation in time was conducted. All of the interpolation and smoothing techniques were conducted with use of MATLAB 6.5 spline toolbox 3.1.1. More about these techniques is provided in Appendix A.

The resulting $n(\rho,t_{rel})$ function is shown on Fig. 8.5.

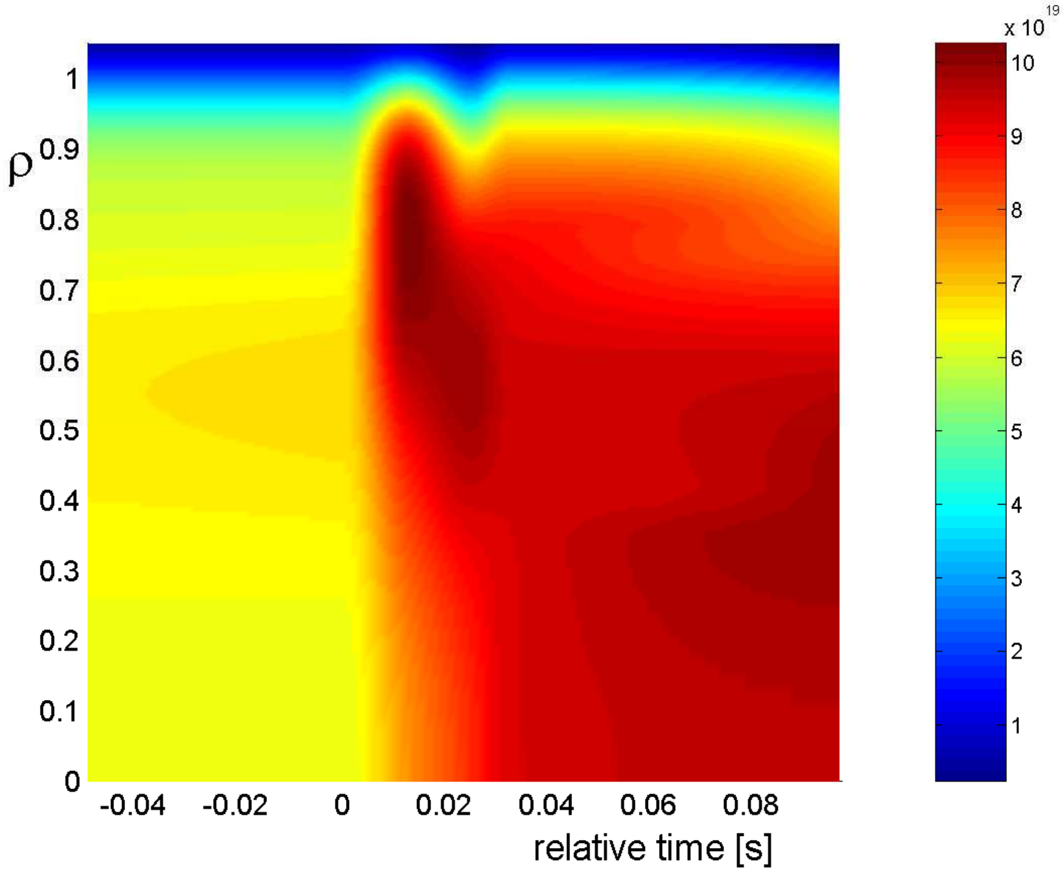

Figure 8.5: *2D contour plot showing the electron density evolution* $n(\rho,t_{rel})$ *due to pellet. The colorbar on the right side shows the relation between colour and density (in* m^{-3}*).*

On Fig. 8.5, it is possible to clearly observe the sudden increase of plasma electron density after the relative time $t=0s$ indicating the pellet injection and also a great density peak at the pellet penetration radius around $\rho = 0.8$.

This smoothed and interpolated function $n(\rho,t_{rel})$ is computed in *200* magnetic surfaces ρ and *150* relative times. Using numerical techniques, for each relative time t_{rel} and magnetic surface ρ the number of electrons contained inside the surface $N(\rho,t_{rel})$, the surface volume $V(\rho,t_{rel})$ and the surface area $S(\rho,t_{rel})$ was computed. On the following Fig. 8.6, the time evolution of the number of electron particles contained in plasma ($N(\rho,t_{rel})$ for separatrix $\rho = 1$) can be seen.

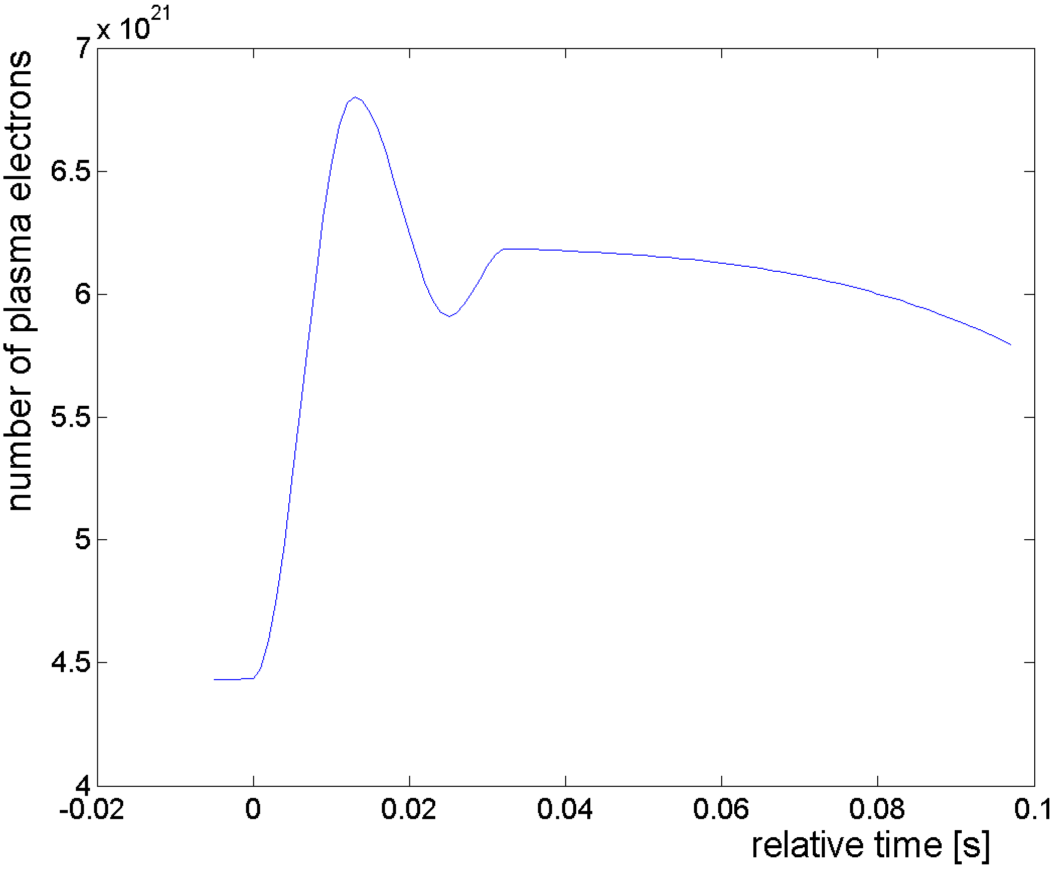

Figure 8.6: *Time evolution of the total electron particle content in plasma during the average post-pellet electron density evolution.*

From the increase of the number of particles after the pellet injection at $t_{rel} = 0ms$ till its peak at about $t_{rel} = 13ms$ (denoting the total pellet evaporation) shown on Fig. 8.6 it can be clearly deduced that the number of deuterium atoms contained in the pellet is $N \approx 2.4 \cdot 10^{21}$. This numbered roughly corresponds to the expected value of $3 \cdot 10^{21}$ deuterium atoms quoted in the paper [25]. The difference between this calculated pellet size and the expected value is quite good. The difference can be easily attributed to:

1. the imperfection of measurement of the pellet size
2. losses in guide tube between the measurement point and the plasma

From the equation (4.2) it can be deduced, that the temporal derivative of the number of plasma electrons contained inside a magnetic surface ρ is proportional to the electron particle flux flowing inside through the area of the magnetic surface ρ:

$$\frac{\partial N(\rho, t_{rel})}{\partial t} = -\Gamma(\rho, t_{rel}) \cdot S(\rho, t_{rel}) \,. \tag{8.20}$$

The time derivative in (8.20) can be replaced by a forward difference:

$$\frac{\partial N(\rho,t_{rel})}{\partial t} \approx \frac{N(\rho,t_{rel}+\Delta t_{rel}) - N(\rho,t_{rel})}{\Delta t_{rel}}, \qquad (8.21)$$

where Δt_{rel} is the difference between two times of the discrete $N(\rho,t_{rel})$ data. The particle flux $\Gamma(\rho,t_{rel})$ is then computed as:

$$\Gamma(\rho,t_{rel}) = -\frac{N(\rho,t_{rel}+\Delta t_{rel}) - N(\rho,t_{rel})}{\Delta t_{rel}} \cdot \frac{1}{S(\rho,t_{rel})} \qquad (8.22)$$

and it is shown on Fig. 8.7 for $\rho = 0.8;\ 0.9$ and 1.0 (for the region impacted by the pellet ablation and evaporation at the edge of plasma).

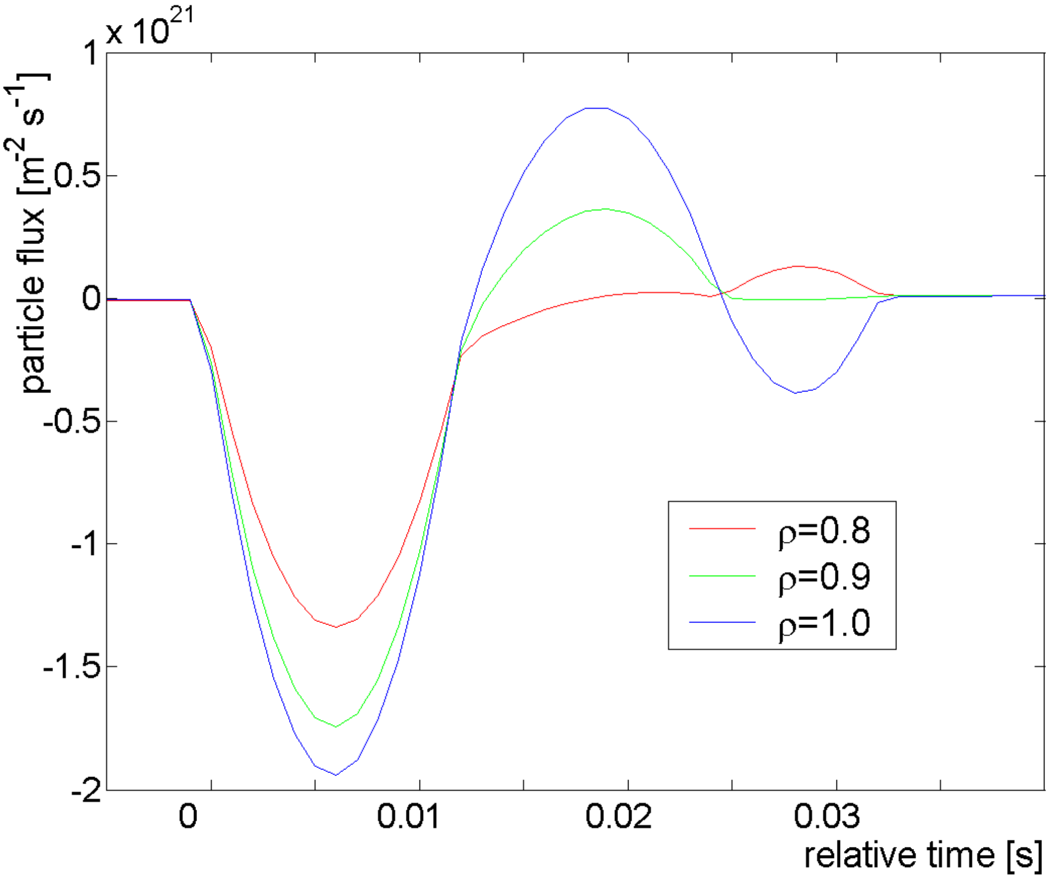

Figure 8.7: *The temporal evolution of electron particle flux through magnetic surfaces* $\rho = 0.8$*, 0.9 and 1.0. The negative value means inward direction of the flux.*

Fig. 8.7 allows us to clearly observe negative electron particle flux during the pellet evaporation. This is attributed to the particle source omitted in the equation (8.20). Focus of our study is however the time interval after pellet is evaporated, when the particle source can be neglected. This part corresponds to the interval $t_{rel} > 13ms$. In this time interval the direction of the flux is positive due to particle losses.

Using equation (8.1) along with the knowledge of $\Gamma(\rho,t_{rel})$ it is possible to compute the effective diffusion coefficient. It is however necessary to evaluate the density gradient $\vec{\nabla} n$.

As was mentioned in chapter 3.4, the ρ coordinate for large aspect ratio tokamaks satisfies approximately the relation $\rho \approx r/a$ (where *a* is the tokamak minor radius). The linear relation between minor radius and ρ can be clearly observed on Fig. 8.8 (left plot) for *z=0*. For every relative time t_{rel} the minor radius $r = r(\rho)$ for *z=0* is computed as $r(\rho) = |R(\rho) - R_0|$, where *R* is the major radius and R_0 is the major radius of the plasma centre (which can be deduced from the minimum of $\rho(R, z=0)$). The dependence $r(\rho)$ is then fitted by a line $r = k \cdot \rho + q$ (Fig. 8.8, right plot).

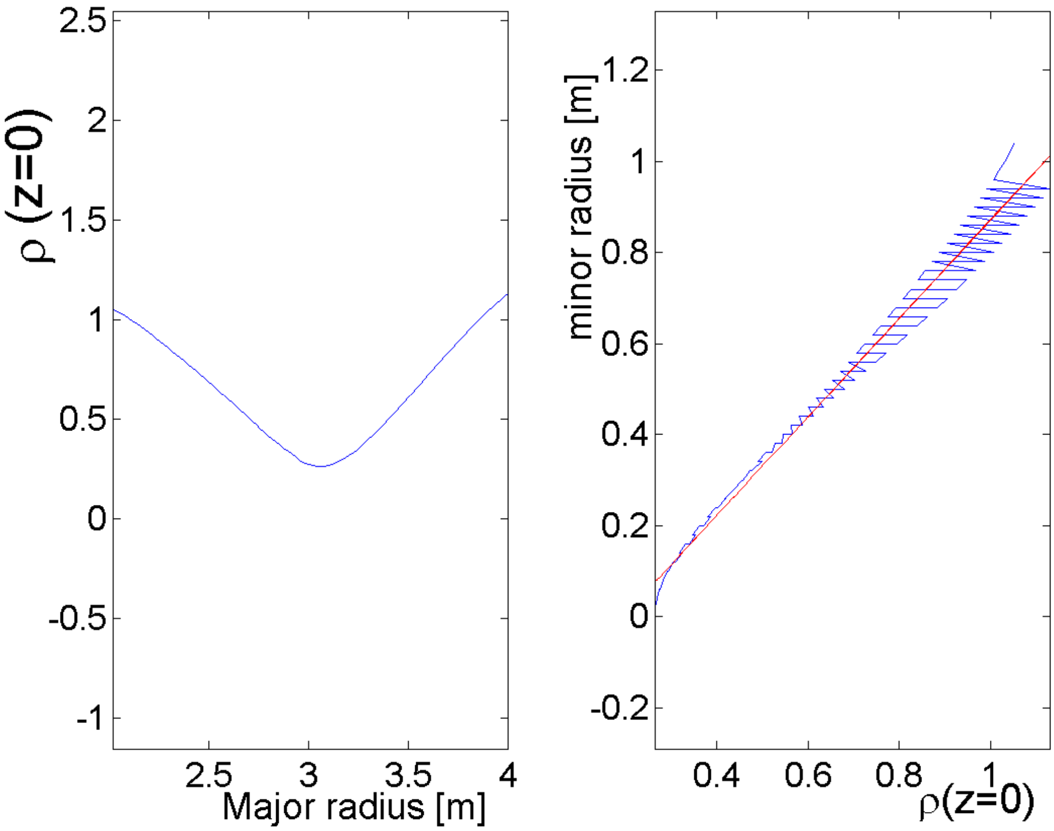

Figure 8.8: *Dependence* $\rho = \rho(R)$ *for midplane* $z = 0$ *(left); fitted dependence* $r = k \cdot \rho + q$ *for midplane* $z = 0$ *(right). The fitting was done by using MATLAB 6.5 curve fitting tool.*

For all relative times, *k* was in a range *1.05-1.16*, which well corresponds to the plasma minor radius $a \approx 1m$. The value of *q* ranged from *-0.28* to *-0.18*.

The gradient in general orthogonal coordinates (q_1, q_2, q_3) can be computed as:

$$\vec{\nabla} = \frac{1}{h_1}\frac{\partial}{\partial q_1}\hat{q}_1 + \frac{1}{h_2}\frac{\partial}{\partial q_2}\hat{q}_2 + \frac{1}{h_3}\frac{\partial}{\partial q_3}\hat{q}_3, \tag{8.23}$$

where $\hat{q}_i$, *i=1,2,3* are unit vectors of the base of these coordinates and coefficients h_i, *i=1,2,3* are the so called *scale factors* [36]:

$$h_i = \sqrt{g_{ii}} = \sqrt{\sum_{k=1}^{3}\left(\frac{\partial x_k}{\partial q_i}\right)^2}\ , \tag{8.24}$$

where g_{ij} is the metric tensor and x_i, $i=1,2,3$ are the Cartesian coordinates. In our case, the coordinates are modified cylindrical coordinates (ρ,φ,z), where φ is the poloidal angle and z measures the distance in toroidal direction:

$$\begin{aligned} x &= r\cos\varphi = (k\cdot\rho+q)\cdot\cos\varphi \\ y &= r\sin\varphi = (k\cdot\rho+q)\cdot\sin\varphi\ . \\ z &= z \end{aligned} \tag{8.25}$$

The scale factors can therefore be calculated (with use of (8.24, 8.25)) as:

$$\begin{aligned} h_\rho &= k \\ h_\varphi &= k\cdot\rho+q \\ h_z &= 1 \end{aligned} \tag{8.26}$$

And the gradient in (ρ,φ,z) is:

$$\vec{\nabla} = \frac{1}{h_\rho}\frac{\partial}{\partial\rho}\hat{\rho} + \frac{1}{h_\varphi}\frac{\partial}{\partial\varphi}\hat{\varphi} + \frac{1}{h_z}\frac{\partial}{\partial z}\hat{z} = \frac{1}{k}\frac{\partial}{\partial\rho}\hat{\rho} + \frac{1}{k\cdot\rho+q}\frac{\partial}{\partial\varphi}\hat{\varphi} + \frac{\partial}{\partial z}\hat{z}\ . \tag{8.27}$$

If we assume that the electron density is a function of magnetic surfaces (and time) only, $n = n(\rho,t_{rel})$, the size of its gradient in new coordinates using ρ has a very simple form of:

$$\nabla n = \frac{1}{k}\frac{\partial n}{\partial\rho} \tag{8.28}$$

and using the forward difference to replace the partial derivative again:

$$\nabla n(\rho,t_{rel}) \approx \frac{1}{k(t_{rel})}\frac{n(\rho+\Delta\rho)-n(\rho)}{\Delta\rho} \tag{8.29}$$

The diffusion coefficient can thus be calculated us:

$$D(\rho,t_{rel}) = -k(t_{rel})\cdot\Gamma(\rho,t_{rel})\cdot\frac{\Delta\rho}{n(\rho+\Delta\rho)-n(\rho)}\ . \tag{8.30}$$

The temporal evolution of the computed diffusion coefficient $D(\rho,t_{rel})$ for ρ *=0.8, 0.85, 0.9, 0.95* and *1.0* is shown on Fig. 8.9 below.

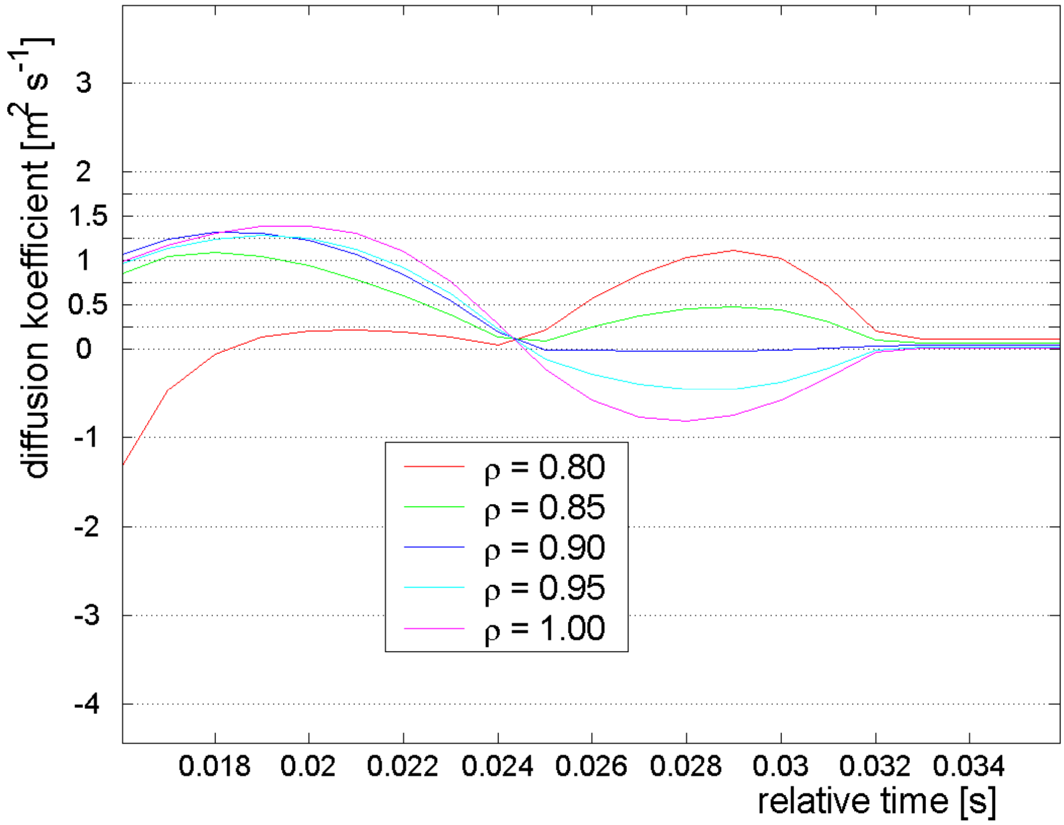

Figure 8.9: *Temporal evolution of the computed diffusion coefficient* $D(\rho, t_{rel})$ *for* ρ *=0.8, 0.85, 0.9, 0.95 and 1.0.*

Interpretation

The diffusion can be derived from the Fig. 8.9. The relevant part of the plasma is $r/a = 0.8 - 1.0$, i.e. the region between the maximum of pellet deposition and plasma edge (see Fig. 8.4). It is the particle diffusion in this region which determines the post-pellet losses and then consequently the requirements on pellet fuelling system.
The relevant time interval is t_{rel} = *0.016 - 0.022s*. This selection of time interval is dictated by two considerations:

(1) It is well after the initial rise of the plasma density during t_{rel} = *0.-0.15s* due to the pellet injection (the particle source is large, see Fig. 8.6)

(2) It is before the time t_{rel} ~ *0.03s*, when the total particle content temporarily increases, which gives negative flux (Fig. 8.7). The likely reason for this increase is that it is the artifact of boxcar analysis, as we assumed that all pellets and their post-pellet transport are identical, which is clearly not the case.

In conclusion, from the Fig. 8.9 the effective diffusion coefficient is:

– ***D_{eff} ~ 0.25-1.35 m^2/s.*** *(r/a~0.8-1)*

This value is consistent with the previous analysis in [1], where a value ~ $0.8 m^2 s^{-1}$ was found.

8.3 Pellet particle confinement

In parallel with the local transport analysis presented we can perform global particle confinement analysis.

As the pellets are injected into the plasma and reach deeper regions of the plasma column before total evaporation, they greatly affect the plasma confinement and transport, especially at the edge. The local density increase can be in order of tens of percent (for ITER it can be up to *50%*, depending on the penetration) and the plasma is non-stationary, responding to these perturbations. The main parameters of the pellet, which affect the post pellet transport, are the *pellet deposition radius* r_{pel} (or its value normalized to the minor radius $\rho_{pel} = r_{pel} / a$) and the *post pellet particle confinement time* (pellet retention time) τ_{pel}. These two parameters are very important, because they determine the particle throughput provided by the pellet injection system, which is necessary to maintain the plasma density [35]:

$$\Phi_{pel} \approx n_e \cdot S \cdot a \cdot (1 - \rho_{pel}) / \tau_{pel}, \tag{8.31}$$

where n_e is the electron density averaged in time (over pellets) and in normalized radius $\rho_{pel} \le \rho \le 1$, S is the plasma surface.

The *pellet deposition radius* is a radius, where the major part of the pellet is deposited. It depends on the injection speed, pellet size, pellet injection path and additional effects like pellet ∇B drifting and plasma turbulence. The pellet evaporation for JET shot *#53212* lasts usually about *10ms*. For our case, the normalized pellet deposition radius can be determined from the post pellet electron density profile at Fig. 8.4, as it was assumed that the magnetic surface coordinate $\sqrt{\psi} = \rho \approx r / a$. Therefore:

- $\boldsymbol{\rho_{pel} \approx 0.80}$.

The pellet injection induces a strong perturbation of the plasma and affects the confinement significantly. The development of the edge plasma transport after the pellet is described by the *post pellet particle confinement time* τ_{pel}. It can be determined from the post pellet evolution of plasma density at a fixed radius (the pellet deposition radius was chosen in our case):

$$n_e(t,\rho_{pel}) \propto exp[-(t-t_{pel})/\tau_{pel}], \tag{8.32}$$

where t_{pel} is the time of total pellet evaporation (deposition). From the equation (8.32) it can be seen, that τ_{pel} represents a characteristic time of the perturbed density evolution. The calculation can be made by taking a logarithm of the equation (8.32) and doing a linear least square fit of the data.

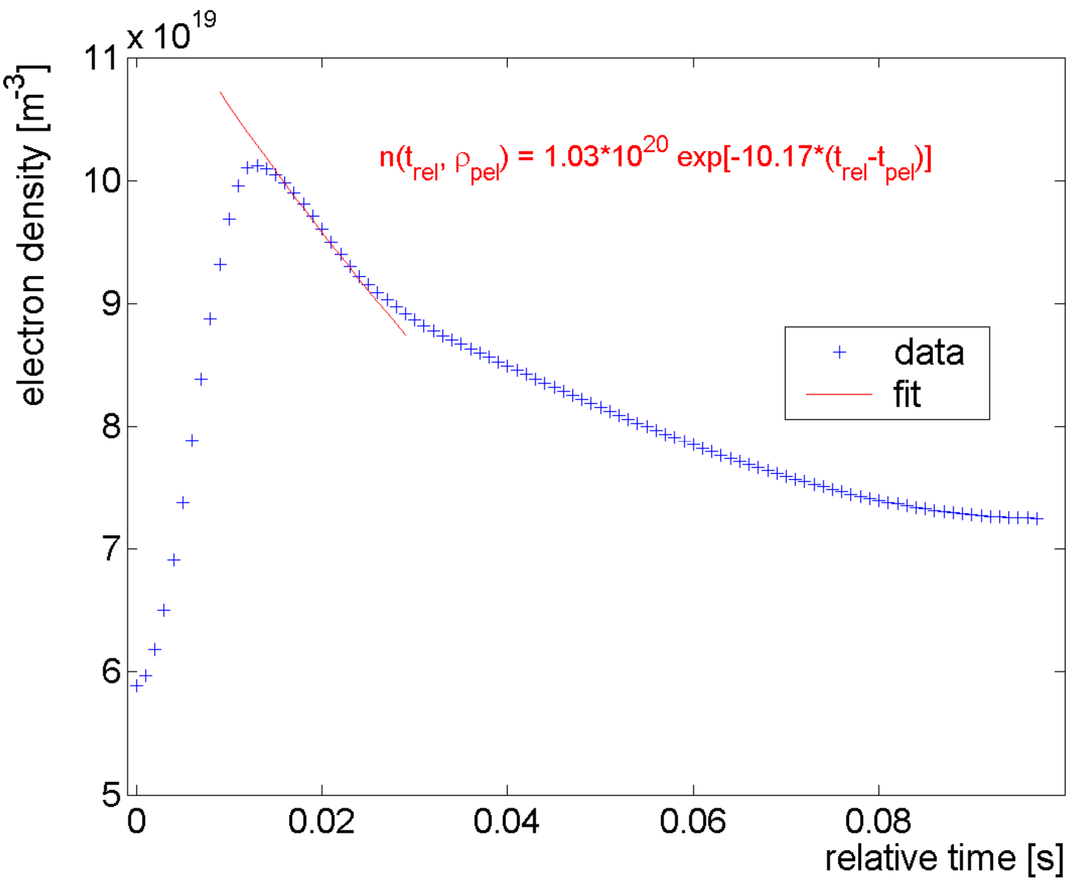

Figure 8.10: *Exponential fit of the post-pellet density evolution at the normalized pellet deposition radius ρ_{pel}=0.80. The data used are $n(\rho, t_{rel})$ from the numerical analysis in chapter 7.2. The fitting was done by using MATLAB 6.5 curve fitting tool.*

With use of the pre-processed data $n(\rho, t_{rel})$ from the previous chapter 8.2, the exponential fit was done for the relative time interval *16ms-22ms*, which was considered most relevant in order to compute the immediate quick losses of the plasma particles and with $t_{pel} = 13ms$ as the time of the pellet total evaporation (estimated as the time of maximal plasma particle content on Fig. 8.6). The fitted density-time dependence is:

$$n(t_{rel},\rho_{pel}) = 1.03 \cdot 10^{20} \exp[-10.17 \cdot (t_{rel}-t_{pel})], \qquad (8.33)$$

Therefore the value of τ_{pel}, along with its error (95% confidence bound) from the log-linear fit is:

- $\boldsymbol{\tau_{pel} = 98.3 \pm 5.3ms}$

This value corresponds with the typical values of pellet retention time during the JET discharges, which is about *50–100ms*.

A possible error of this calculation arises from the fact, that the density evolution need not have an exponential shape and that the τ_{pel} is not a constant, but changes in time and is usually shorter immediately after the pellet than later on. To minimize this, only a short time interval of fast particle losses was chosen for the calculation. The error may be also enhanced by the error of the boxcar method itself.

If we carry out a dimensional analysis of the simplified diffusion equation (8.5), where D is the particle diffusion coefficient, and we assume a characteristic time of the density evolution to be τ_{pel} and a characteristic length to be pellet penetration depth, which is $\Delta_r = a - r_{pel}$, we get:

$$\frac{n}{\tau_{pel}} \propto \frac{n}{\Delta_r^2} \tag{8.34}$$

and we can express τ_{pel} in the following form:

$$\tau_{pel} = const.\cdot(\Delta_r^2 / D), \tag{8.35}$$

or in a form more suitable for scaling purposes:

$$\tau_{pel} = const.\cdot a^2\cdot(\,(1-\rho_{pel})^2 / D), \tag{8.36}$$

where $\rho_{pel} = r_{pel}/a$ is the pellet deposition radius normalized to the minor radius. The constant in (8.35), (8.36) depends on the exact shape of the density profile. From the knowledge of D and τ_{pel} it is possible to approximately determine the constant for our experiment and gain a useful and simple formula:

– $\boldsymbol{\tau_{pel} \approx (0.61\text{-}3.07)\cdot(\Delta_r^2 / D)}$

(the computed value $D=0.25 - 1.35 m^2 s^{-1}$ found in the previous chapter 8.2 was used).

To be able to predict the pellet retention time τ_{pel} to next step devices such as ITER, the experimental values are usually normalized to the total energy confinement time τ_E, for which there exists an energy confinement scaling. The energy confinement time is defined as the total energy content of the plasma divided by the total power input. For JET shot *#53212* during the pellet operation $E \approx 5\text{-}6 MJ$, $P \approx 18 MW$ and so $\tau_E \approx 0.28\text{-}0.33 s$. Therefore

– $\boldsymbol{\tau_{pel} / \tau_E \approx 0.30\text{ -}0.35}$.

The pellet retention time is normalized to the energy confinement time because of an assumption, that the two processes of particle and energy transport are bounded and both heat and particle transport after the pellet is driven by the same turbulence. Moreover, the diffusion coefficient D and the thermal diffusion coefficient χ usually follow a relation $D \approx (0.2\text{-}0.6)\,\chi$.

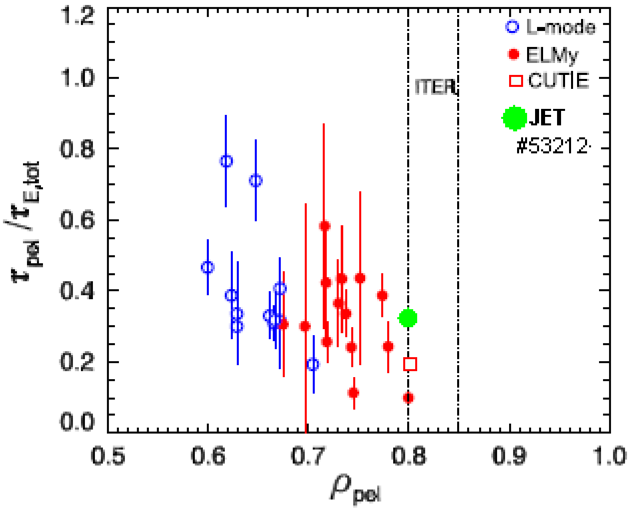

Figure 8.11*: Comparison of the ratio τ_{pel}/τ_E for JET shot #53212 (green) and for pellet experiments on MAST tokamak [35]*

On Fig. 8.11 can be seen, that the estimated ratio τ_{pel}/τ_E for the JET shot *#53212* corresponds well to similar measurements made for the MAST tokamak.

In this chapter 8.3 information from [35] were used to perform a similar analysis as on MAST tokamak.

8.4 Fuelling requirements for ITER

The expected parameters of a nominal ITER discharge are following: minor radius $a = 2.0m$, electron density is $n_e = 10^{20} m^{-3}$, plasma surface $S = 683m^2$ and the energy confinement time $\tau_E = 3.7s$. The pellet deposition radius expected on ITER is $r_{pel} / a \approx 0.8 - 0.85$. With use of the previously found relation of pellet retention time and energy confinement time $\tau_{pel} / \tau_E = 0.30 - 0.35$ it is possible to estimate τ_{pel} for ITER as $\tau_{pel} \approx 1.11 - 1.30s$. The particle throughput provided by the ITER pellet injection system, which is necessary to maintain the plasma density can then be computed from (8.31) as approximately:

– $\Phi_{pel} \approx (160\text{-}250) \cdot 10^{20} s^{-1}$ or in more usual units $\boldsymbol{\Phi_{pel} \approx 30 - 50 Pa \cdot m^3 s^{-1}}$.

The value $50Pa \cdot m^3 s^{-1}$ is about *50%* of the present ITER design value for steady-state operation. To supply particles at this rate using the largest fuelling pellets ($d_{pel} = 5mm$, $6.2 \cdot 10^{21}$ atoms) implies the pellet frequency of $f_{pel} = 4Hz$. This would mean that the time interval between pellets, $1/f_{pel} = 0.25s$ would be *4-5* times shorter than the pellet retention time τ_{pel}. Such situations are rare in present pellet-fuelled plasmas and the values of τ_{pel} in such conditions are not known. Another uncertainty arises from the fact that the proposed ELM mitigation techniques enhance the edge particle transport and could result in shorter pellet retention time, which would in turn increase the needed pellet throughput (8.31). The assumed pellet penetration depth in ITER, $r_{pel} / a \approx 0.8 - 0.85$, is also uncertain as it relies fully on the existence of drift of the ablated pellet particles. Without the drift, the ablation models predict the penetration just up to the pedestal and thus the pellet retention time would be negligible due to the ELMs. Therefore to be able to predict the plasma density on ITER and the needed throughput (8.31), a better scaling for both fuelling parameters: pellet deposition radius and pellet retention time is needed. [35]

8.5 Post pellet plasma fluctuations estimate

The post pellet diffusion coefficient is anomalous, as it reaches values $\sim 1 m^2 s^{-1}$. A simple estimate was therefore made to roughly determine the size of the plasma turbulent fluctuations, which would cause this enhanced anomalous transport after the pellet injection.

The effective diffusion coefficient D_{eff} from the equation (8.1) was determined as ~ 0.25-$1.35 m^2 s^{-1}$ in Chapter 8.2 for the edge of plasma and describing the fast post pellet losses. From Fig. 8.7, the edge plasma particle flux during the fast post-pellet losses reaches values

- $\boldsymbol{\Gamma \approx 0.3\text{–}7.8 \cdot 10^{20} m^{-2} s^{-1}}$

Electrostatic fluctuations

At first let us assume this flux to be caused by electric field fluctuation (perpendicular to the magnetic field) (4.19),(4.20). The typical density fluctuations at the edge plasma are $\delta n/n \sim 0.1$. For the fluctuation of the electric field we may write:

$$\delta E = grad\ \delta\phi , \tag{8.37}$$

where $\delta\phi$ is a fluctuation of the plasma electric potential. In the equation (8.37) the gradient operation can be approximated by multiplying by the typical wave number of the fluctuations, perpendicular to the magnetic field $k_\perp$. This wave number is related to the ion Larmor radius $r_{L,i}$, as it is usually $k_\perp \cdot r_{L,i} \sim 0.4$. The equation (8.20) may be rewritten in the following form:

$$\Gamma = \langle \delta v_\perp \delta n \rangle = \delta v_\perp \delta n \cdot \cos\theta , \tag{8.38}$$

where the right side shows the sizes of the fluctuations and θ is the phase shift between those two fluctuations. Assuming $\cos\theta \approx 0.5$ we may write with use of (8.37), (8.38), (4.19):

$$\delta\phi = 5 \cdot \frac{r_{L,i} B_T}{n\left(\frac{\delta n}{n}\right)} \Gamma . \tag{8.39}$$

The ion Larmor radius $r_{L,i}$ is determined by a formula:

$$r_{L,i} = \frac{m_i v_{\perp,i}}{e B_T} , \tag{8.40}$$

where $v_{\perp,i}$ is the ion velocity perpendicular to the magnetic field, e is the ion electric charge and m_i is the ion mass. By assuming the velocity to be thermal and the ion temperature to be approximately equal to the electron one $T_i \approx T_e$ we may write:

$$v_i \approx \sqrt{\frac{k_B T_e}{m_i}} \text{ and } \delta\phi = 5\frac{\sqrt{m_i k_B T_e}}{en\left(\frac{\delta n}{n}\right)}\Gamma, \qquad (8.41)\ (8.42)$$

where T_e is the electron temperature and k_B is the Boltzmann constant. For a numerical calculation, following values were used: $m_i=3.33\cdot10^{-27}kg$ is the mass of deuteron (assuming deuterium plasma), $k_BT_e \approx 1.3keV$ is the plasma electron temperature for time $t = 57.88s$ just after the first pellet and for radius ρ_{pel}, $e=1.6\cdot10^{-19}C$ is the elementary charge, $n \approx 10^{20}m^{-3}$ is the plasma electron density for the same time and radius as the temperature, $\delta n/n\sim0.1$. The resultant potential fluctuation $\delta\phi$ causing the maximum flux $\Gamma \approx 7.8\cdot10^{20}\, m^2 s^{-1}$ therefore is:

- $\boldsymbol{\delta\phi \approx 2.0\ V}$

It is usual to relate $e\delta\phi$ to k_BT_e, as $e\delta\phi$ is usually a small part of the electron temperature k_BT_e,. For our case:

- $\boldsymbol{e\delta\phi \approx 1.5\cdot10^{-3}\, k_BT_e}$

Magnetic fluctuations

From Fig. 6.2 which shows the interferometer line averaged plasma density and the D_α emission during the pellet operation it is obvious, that ELMs play crucial role and are the major reason for post pellet fast particle losses. ELM's are magnetohydrodynamic (MHD) instabilities, which affect the magnetic field. From this it is possible to deduce that the anomalous transport due to magnetic fluctuations and disturbance of the magnetic field may be more relevant than the anomalous transport driven by electrostatic fluctuations.

The value of radial magnetic field fluctuation δB_r, which would cause the post pellet transport of particles may be roughly estimated using equations (4.32), (4.33) (note that it can be used only when assuming collisionless plasma, where $l_{mfp} > L_C$). We assume $v_{//} = c_s$, where c_s is the speed of sound for ions in plasma [8]:

$$c_s = \sqrt{\frac{\gamma_i k_B T_i}{m_i}}, \qquad (8.43)$$

where γ_i is the polytrophic index for ions. Equation (4.33) can be then written in the following form:

$$D = c_s\left(\frac{\delta B_r}{B}\right)^2 L_c \Rightarrow \delta B_r = B\sqrt{\frac{D}{L_c c_s}}. \qquad (8.44)$$

With use of estimates $L_c \sim qR \sim 10m$, $T_i \approx T_e$ and using following values: $m_i=3.33 \cdot 10^{-27}kg$, $B=2.4T$, $\gamma_i \approx 5/3$, $k_B T_e \approx 1.3keV$, $D \approx 0.25\text{-}1.35m^2s^{-1}$, the radial magnetic field fluctuation δB_r, which would cause the post pellet particle transport, was roughly determined as:

- $\boldsymbol{\delta B_r \approx 0.7\text{-}1.3mT}$

Relatively small values of fluctuating electrostatic potential and fluctuating magnetic field required to explain the post pellet particle losses indicate, that both processes can be at work.

9 Summary and conclusions

Plasma refuelling is one of the most important parts of the tokamak research. The most important technology of tokamak plasma fuelling for future devices like ITER would be the pellet injection. High speed injection of frozen fuel pellets provides efficient refuelling by deeper particle deposition. The efficiency of pellet fuelling determines how much of fuel has to be injected into the plasma in order to keep the plasma density at the level necessary for given fusion power. The question of refuelling is closely connected with the particle confinement and transport in plasma, which is the subject of this thesis.

The results of this work can be summarised as follows:

1) The post-pellet effective diffusion coefficient at the edge plasma was calculated using simplified solution of the diffusion equation in axial symmetry. The diffusion coefficient was estimated as $D = 3.295 m^2 s^{-1}$ for a time interval *12.5-25ms* after the pellet injection and $D = 2.872 m^2 s^{-1}$ for a time interval *25-32.525ms* after the pellet injection. This value is rather large compared to similar studies on the MAST tokamak [27],[33] and in the bachelor thesis [1]. The error is supposed to be caused by the wrong assumption of circular-shaped plasma. In the next part of the chapter 7 a more profound analysis was made using the magnetic surface coordinates. The LIDAR data were mapped on the magnetic surfaces, where the density is assumed constant. Spatially and time resolved effective diffusion coefficient was then computed. For the edge plasma $\rho \in (0.8, 1.0)$ and the post-pellet time interval *16-22ms* it was $D \approx 0.25 - 1.35 m^2 \cdot s^{-1}$. This range of values is consistent with previous calculations in [1], where the diffusion coefficient was estimated as $D = 0.8 \pm 0.4 m^2 s^{-1}$ and also with pellet experiments on the MAST tokamak, where typically $D = 0.7 - 1.8 m^2 s^{-1}$.

2) The pellet size was estimated from the growth of plasma particle content due to the pellet as $N_D \approx 2.4 \cdot 10^{21}$ deuterium atoms. This is consistent with pellet size measured at pellet injector.

3) The pellet retention time and the pellet deposition radius were estimated. The pellet retention time is a characteristic time of the post pellet density evolution, the pellet deposition radius is a radius, where the major part of the pellet evaporates and is deposited. These two parameters are very important, as they determine the particle throughput provided by the pellet injection system, which is necessary to maintain the plasma density. They were determined as $\tau_{pel} = 98.3 \pm 5.3 ms$ and $\rho_{pel} = 0.8$. The pellet retention time was then normalized to the energy confinement time and found to be in good agreement with similar results from the MAST tokamak.

4) The particle throughput provided by the ITER pellet injection system necessary to maintain the plasma density was estimated to be $\Phi_{pel} \leq 50 Pa \cdot m^3 s^{-1}$. This value is about *50%* of the present ITER design value for steady-state operation, however, the estimate is far from reliable and better scaling for pellet deposition radius and pellet retention time is needed.

5) The last task was to estimate the post pellet plasma fluctuations which drive the anomalous transport. Assuming the post pellet transport to be caused by electrostatic

fluctuations it was possible to roughly determine the plasma potential fluctuations as $e\delta\phi \approx 1.5 \cdot 10^{-3} k_B T_e$. Assuming that the particle transport is topology driven by the perturbation of the magnetic field topology (due to ELMs), radial magnetic field fluctuation δB_r was roughly determined as $\delta B_r \approx 0.7 - 1.3 mT$.

Measurements and understanding of post pellet particle confinement in present tokamaks is far from complete. Further improvements are clearly necessary in order to design the fuelling systems for future fusion reactors.

A Appendix

A.1 Cubic spline interpolation

In the numerical analysis, interpolation is a method of constructing new data points within the range of a discrete set of known data points. The spline function interpolation uses piecewise polynomial function of a degree *m* called *spline* as interpolant. This function is generally continuous on its domain along with its derivatives to the order *m-1* and its *m-th* order derivative is square integrable. In technical applications, the most useful spline functions are piecewise third degree (cubic) polynomials.

In the following text, the explanation of the method will be constrained to real functions of one variable only for simplification and better understanding of the sense of the method.

On interval $\langle a,b \rangle$ of a real axis x is given a grid $a = x_0 < x_1 < ... < x_n = b$ and in its knots are given values $\{f_k\}_{k=0}^{n}$ of a function $f(x)$ defined on $\langle a,b \rangle$. Let us formulate the problem of piecewise cubic interpolation. On interval $\langle a,b \rangle$ we are looking for a function $g(x)$, which is in agreement with the following requirements:

(1) $g(x)$ belongs to the group of functions $C^2(a,b)$ continuous with derivatives to the second order.

(2) On every interval $\langle x_{k-1}, x_k \rangle$, $g(x)$ is a cubic polynomial of a shape:

$$g(x) \equiv g_k(x) = \sum_{l=0}^{3} a_l^{(k)} (x_k - x)^l \ , \ k = 1,...,n \ . \tag{A.1}$$

(3) In the knots of the grid $\{x_k\}_{k=0}^{n}$ the following equalities are accomplished:

$$g(x_k) = f_k \ , \ k = 0,1,...,n \ . \tag{A.2}$$

(4) $g''(x)$ fulfils the boundary conditions:

$$g''(a) = g''(b) = 0 \ . \tag{A.3}$$

It can be shown that the outlined problem of finding the interpolation piecewise cubic function $g(x)$ has only one solution. Let us outline its calculation.

Because the second order derivative $g''(x)$ is continuous (1) and linear (2) on every interval $\langle x_{i-1}, x_i \rangle$, $i = 1,...,n$ of the grid, we can write for $x_{i-1} \le x \le x_i$:

$$g''(x) = m_{i-1} \frac{x_i - x}{h_i} + m_i \frac{x - x_{i-1}}{h_i} \ , \tag{A.4}$$

where $h_i = x_i - x_{i-1}$, $m_k = g''(x_k)$. After double integration of (A.4) over *x*:

$$g(x) = m_{i-1}\frac{(x_i - x)^3}{6h_i} + m_i\frac{(x - x_{i-1})^3}{6h_i} + A_i\frac{x_i - x}{h_i} + B_i\frac{x - x_{i-1}}{h_i}, \tag{A.5}$$

where A_i and B_i are integration constants. They can be calculated from conditions $g(x_{i-1}) = f_{i-1}$, $g(x_i) = f_i$ (3). By applying $x = x_i$ and $x = x_{i-1}$ on (A.5) we get:

$$m_i\frac{h_i^2}{6} + B_i = f_i$$

$$m_{i-1}\frac{h_i^2}{6} + A_i = f_{i-1}$$

Therefore (A.5) can be rewritten as:

$$g(x) = m_{i-1}\frac{(x_i - x)^3}{6h_i} + m_i\frac{(x - x_{i-1})^3}{6h_i} + \left(f_{i-1} - \frac{m_{i-1}h_i^2}{6}\right)\frac{x_i - x}{h_i} + \left(f_i - \frac{m_i h_i^2}{6}\right)\frac{x - x_{i-1}}{h_i}, \tag{A.6}$$

$$g'(x) = -m_{i-1}\frac{(x_i - x)^2}{2h_i} + m_i\frac{(x - x_{i-1})^2}{2h_i} + \frac{f_i - f_{i-1}}{h_i} - \frac{m_i - m_{i-1}}{6}h_i. \tag{A.7}$$

With use of the presumption (1) about the continuity of functions $g'(x)$ and $g''(x)$ on $\langle a,b\rangle$ and with use of (A.3) it is possible to gain a set of linear algebraic equations for the unknowns $m_1, m_2, ..., m_n$. The matrix of this set of equations is regular and therefore there is only one solution of $g(x)$ given by (A.6).

The high effectiveness of the cubic spline function interpolation is caused by its following characteristics: Let us assume a group of functions $W_2^2(a,b)$ on the interval $\langle a,b\rangle$, which have square integrable second order derivative. Let us search an interpolation function:

$$u \in W_2^2(a,b),\ u(x_k) = f_k,\ k = 0,1,...,n, \tag{A.8}$$

which minimizes a functional

$$\Phi(u) = \int_a^b (u''(x))^2\,dx \tag{A.9}$$

It can be shown that it is exactly the cubic spline function $g(x)$. Therefore an alternative definition of the piecewise cubic spline function is that it is such function from $W_2^2(a,b)$, which has the prescribed values in the knots of the grid and it minimizes the functional (A.9). This characteristic can be physically interpreted: Since the total energy of an elastic strip is proportional to its curvature, the spline is the configuration of minimal energy of an elastic strip constrained to *n* points.

A.2 Piecewise cubic smoothing spline function

Let us solve the same problem of searching a smooth approximation of a function defined by values on a grid $a = x_0 < x_1 < ... < x_n = b$ as before. This time the functional values f_k are not accurate and contain an error. In this case it is pointless to construct an interpolation function, which has the same values as f_k in the knots of the grid. It is necessary to construct a function, which will be near these values, but smoother than the interpolant. These functions are not called interpolation functions, but smoothing. Let us demand, that the smoothing function g_x is from $W_2^2(a,b)$ and minimizes the following functional:

$$\Phi_1(u) = \int_a^b (u'')^2\, dx + \sum_{k=0}^{n} p_k \left(u(x_k) - f_k\right)^2 , \qquad \text{(A.10)}$$

where p_k are certain positive numbers. In this functional (A.10), the interpolation conditions that the function passes near the knot values and the condition of minimal "undulation" of the function are connected. The greater are the weight coefficients p_k, the stronger are the interpolation conditions and the nearer would the smoothing function be to the knot values. It can be shown that the solution of (A.10) is a cubic spline function, i.e. function which agrees to the conditions (1), (2) and (4) in the previous chapter A.1. The solution of this problem can be found for example in [37], along with other numerical problems concerning the spline functions. The text in this chapter was written with use of [37] and [38].

Acknowledgements

At the first place I would like to thank to my supervisor Ing. Martin Valovič, Ph.D. for his support and help with my work and also for his great patience. I would also like to express my gratitude to the following persons from the COMPASS tokamak: To my consultant Ing. Ivan Ďuran, Ph.D for his willingness to help me with my work, whenever I was in need, to RNDr. Jan Mlynář, Ph.D. and Mgr. Pavel Cahyna for their useful suggestions and aid with particular problems in my work.

References

[1] P. Háček. *Fuelling efficiency and its impact on plasma parameters in tokamaks,* Bachelor thesis. FJFI ČVUT v Praze, 2007

[2] P. Háček. *Particle confinement of pellet fuelled plasmas in tokamaks*, Research project. FJFI ČVUT v Praze, 2008

[3] G. McCracken, P. Stott. *Fúze, Energie vesmíru.* Mladá fronta, Praha, 2006

[4] J. Wesson. *Tokamaks, third edition.* Oxford University Press, Oxford, 2004

[5] *Iter.org* [online]. [cit. 2009-05-07] <http://www.iter.org>

[6] F. F. Chen. *Úvod do fyziky plazmatu*. Academia, 1984

[7] V. Weinzettl. *Termonukleární fúze v tokamacích* [online] [cit. 2009-05-07] <http://vega.fjfi.cvut.cz/docs/sfbe/tokamak/index.html>

[8] P. Kulhánek. *Teorie plazmatu*, studijní text pro FJFI ČVUT, [online]. [cit. 2009-05-07] <http://www.aldebaran.cz/studium/fpla.pdf>

[9] H. W. Barthels, H.S. Bosch, R. Brakel, H.J. Hartfuss, D. Hartmann, R. Hippler, D.H.H. Hoffmann, R. Kleiber, A. Könies, K. Krieger, A. Melzer, A.G.Peeters, R. Schneider, B.D. Scott, W. Suttrop, H. Zohm. *IPP Summer University for Plasma Physics*, Greifswald, 2005

[10] *EFDA-JET, the world's largest nuclear fusion research experiment* [online]. [cit. 2009-05-07] <http://www.jet.efda.org>

[11] *Glossary of Fusion Terms* [online] [cit. 2009-05-07] <http://www.fusion.org.uk/info/glossary.htm>

[12] S.L. Milora et al. *Pellet fuelling – review paper*. Nucl. Fusion 35 (1995) 657

[13] B. Pégourié. *Pellet injection experiments and modelling*. Plasma Phys. Control. Fusion 49 (2007) R87-R160

[14] F. Köchl. *Pellet drift effect studies at JET*. EPS Conference, Warsaw, 2007, Paper O1.143

[15] I. Senichenkov. *The pellet rocket acceleration caused by* ∇B*-induced drift*. EPS Conference, Warsaw, 2007, Poster O4.094

[16] L.R. Baylor et al. *Pellet fuelling and control of burning plasmas in ITER*. Nucl. Fusion 47 (2007) 443

[17] K. Gal. *Pellet induced perturbations in the plasma edge*. EPS Conference, Warsaw, 2007, Paper O4.080

[18] M. Kubič. *The database for comparison of plasma parameters of the JET tokamak in various regimes of its operation.* Research project. FJFI ČVUT v Praze, 2008

[19] S. Atzeni. *The physics of inertial fusion.* Oxford University Press, Oxford, 2004

[20] P. M. Bellan. *Fundamentals of Plasma Physics.* Cambridge University Press, Cambridge, 2006

[21] H. J. de Blank. *Plasma Equilibrium in Tokamaks*. Carolus Magnus Summer School on Plasma and Fusion Energy Physics, 2005

[22] E. J. Doyle et al. *Chapter 2: Plasma confinement and transport*. Nucl. Fusion 47 (2007) S18 – S127

[23] A. Géraud. *The JET high frequency pellet injector project*. 24th SOFT Conference, Warsaw, 2006, pages P4–H–201

[24] P. T. Lang et al. *ELM Triggering by Local Pellet Perturbations in Type-I ELMy H-mode Plasma at JET*. Nucl. Fusion 47 (2007) 754

[25] P. Lang et al. *High density operation at JET by pellet refuelling*. Plasma Phys. Contr. Fusion 44 (2002) 1919

[26] T.J. Dolan. *Fusion research: Principles, experiments and technology.* Pergamon Press, 2000

[27] M. Valovic. *Confinement characteristics of pellet-fuelled plasmas in MAST*. EPS Conference, Warsaw, 2007, Paper O4.026

[28] M. Valovic at al. *Density peaking in low collisionality ELM-y H-mode in JET*. Plasma Phys. Contr. Fusion, 46 (2004) 1877

[29] *Thomson scattering – Wikipedia, the free encyclopedia*. [online]. [cit. 2009-05-07] <http://en.wikipedia.org/wiki/Thomson_scattering>

[30] I. Furno et al. *A new method for the inversion of interferometry data using basis functions derived from singular value decomposition of local measurements in tokamak plasmas,* Plasma Phys. Control. Fusion 47 (2005) 49-69

[31] M. Krbálek. *Úlohy matematické fyziky, cvičení*. FJFI ČVUT v Praze, 2008

[32] *Heat equation – Wikipedia, the free encyclopedia* [online]. [cit. 2009-05-07] <http://en.wikipedia.org/wiki/Heat_equation>

[33] L. Garzotti. *Post pellet injection transport analysis on MAST.* April 25, 2007

[34] A. D. Polyanin, A. V. Manzhirov. *Handbook of mathematics for engineers and scientists.* CRC Press, 2007

[35] M. Valovič et al. *Particle confinement of pellet-fuelled tokamak plasma*. Nucl. Fusion 48 (2008) 075006 (8pp)

[36] *Scale factor – from Wolfram MathWorld*. [online]. [cit. 2009-05-07] <http://mathworld.wolfram.com/ScaleFactor.html>

[37] G. I. Marčuk. *Metody numerické matematiky*. Academia, Praha, 1987

[38] *Spline interpolation – Wikipedia, the free encyclopedia* [online]. [cit. 2009-05-07] <http://en.wikipedia.org/wiki/Spline_interpolation>

[39] J. Mlynář. *Úvod do termojaderné fúze – lecture*. KF FJFI ČVUT v Praze